IMPROVED PREDICTION OF ADSORPTION-BASED LIFE SUPPORT FOR DEEP SPACE EXPLORATION

by

Karen N. Son

A Dissertation

Submitted to the Faculty of Purdue University

In Partial Fulfillment of the Requirements for the degree of

Doctor of Philosophy

School of Mechanical Engineering

West Lafayette, Indiana

December 2018

THE PURDUE UNIVERSITY GRADUATE SCHOOL
STATEMENT OF COMMITTEE APPROVAL

Dr. Suresh V. Garimella, Chair
School of Mechanical Engineering

Dr. Justin A. Weibel
School of Mechanical Engineering

Dr. Amy M. Marconnet
School of Mechanical Engineering

Dr. Sangtae Kim
School of Chemical Engineering

Dr. James C. Knox
George C. Marshall Space Flight Center, NASA

Approved by:

Dr. Jay P. Gore
Head of the Graduate Program

To Dr. Heng Ban:

Thank you for introducing me to research.

ACKNOWLEDGMENTS

This work was made possible by the financial support of the National Aeronautics and Space Administration (NASA) through the Space Technology Research Fellowship (NSTRF grant #NNX13AL55H). I am especially indebted to Mr. John Sharp and Mr. Greg Schunk for mentoring and supporting my research, and to Dr. James Knox at Marshall Space Flight Center for his invaluable input on my research.

I would like to thank Dr. Suresh Garimella for his continual encouragement and mentorship throughout the past five years of my graduate studies. His guidance has been invaluable to me both personally and professionally. I would also like to thank Dr. Justin Weibel for being a phenomenal mentor, advisor, and friend.

I am forever grateful for many teachers spanning my time in elementary school through my graduate studies who fostered my desire to learn. Special thanks to Dr. Heng Ban, Dr. Ning Fang, Dr. Joyce Kinkead, and Dr. Christie Fox for giving me the opportunity to explore my interests and discover my love for research.

Finally, thank you to my wonderful husband, Forrest. You made weekends in the lab, late nights proofing papers, and every other moment in the past five years immensely enjoyable. Of all the blessings I've received while pursuing my education, I am most grateful for the occasion it afforded me to meet you. Thanks for inspiring me to take giant leaps.

TABLE OF CONTENTS

LIST OF TABLES

LIST OF FIGURES

NOMENCLATURE

A	area, m^2
A_{fr}	free-flow area ($\pi d_{can,in}{}^2/4$), m^2
c	molar concentration, mol/m^3
c_p	specific heat capacity, J/(kg K)
d	diameter, m
$\mathbf{D}$	dispersion coefficient tensor, m^2/s
$D_{eff,j}$	effective diffusivity of species j in the gas-phase mixture, $\left(1/D_{M,j}+1/D_{K,j}\right)^{-1}$, m^2/sec
D_{jk}	binary diffusion coefficient of species j in species k, m^2/sec
$D_{K,j}$	Knudsen diffusivity of species j in the gas-phase mixture, m^2/sec
$D_{M,j}$	molecular diffusivity of species j in the gas-phase mixture, m^2/sec
D_{ax}	axial dispersion coefficient, m^2/s
D_r	axial dispersion coefficient, m^2/s
h	heat transfer coefficient, $W/(m^2\ K)$
k	thermal conductivity, W/(m K)
k_0	mass transfer coefficient, 1/s
k_l	linear-driving-force (LDF) mass transfer coefficient, $m^3/(mol\ s)$
k_{eff}^0	effective axial thermal conductivity of a quiescent bed, W/(m K)
$k_{eff,ax}$	effective axial thermal conductivity of bed with flow, W/(m K)
L	sorbent bed length, m
M	molar mass, g/mol
n	adsorbate concentration in the adsorbed phase, mol/m^3
n^*	equilibrium adsorbed-phase concentration, mol/m^3
p	pressure, kPa
R	universal gas constant, 8.314 J/(mol K)
t	time, s

t_b breakthrough time, s

t_{stoich} stoichiometric breakthrough time, s

T temperature, K

ΔT_g temperature change of gas across the bed, K

$\mathbf{u}$ local superficial velocity tensor (*i.e.*, the Darcy velocity), m/s

u_s superficial fluid velocity, m/s

u_∞ mean inlet superficial fluid velocity, m/s

u_i interstitial fluid velocity (u_s/ε), m/s

V volume, m^3

V_{bed} total bed volume ($\pi d_{can,in}{}^2 L/4$), m^3

$\dot{V}$ volumetric flow rate, SLPM (at 1 atm and 273.15 K)

z axial position, m

y_j mole fraction of species *j*, [mol/mol]

Greek symbols

β radial dispersion factor

ε void fraction (of the sorbent bed)

ε_{CL} , ε_∞ void fraction at bed centerline (*i.e.*, far from the wall)

$\bar{\varepsilon}$, ε_{bulk} average bed porosity (*i.e.*, bulk porosity of the sorbent bed)

ε_r local void fraction of the sorbent bed as a function of radial distance from centerline

λ isosteric heat of adsorption, J/mol

μ dynamic viscosity, kg/(m s)

ρ density, kg/m^3

ρ_{env} pellet envelope density, kg/m^3

τ tortuosity

χ total capacity measured as mass of CO_2 adsorbed, g

Subscripts

0	inlet condition
amb	ambient
ax	axial
bed	sorbent bed
can	canister containing sorbent
CO_2	carbon dioxide
eff	effective
H_2O	water
g	gas-phase
init	initial
in	inner, inside
ins	insulation
max	maximum
mean	mean
out	outer, outside
p	pellet
r	radial
s	sorbent

Dimensionless groups

Nu	Nusselt number
Pe	Peclet number ($Re \times Pr$)
Pe_∞	Peclet number at infinite velocity
Pr	Prandlt number ($\mu c_p / k$)
Re_p	pellet Reynolds number ($u_\infty d_\mathrm{p} \rho_\mathrm{g} / \mu_\mathrm{g}$)
Sc_j	Schmidt number of species j ($\mu_\mathrm{g} / \rho_\mathrm{g} D_j$)

Abbreviations

CDRA	carbon-dioxide removal assembly
DSC	differential scanning calorimetry
LSS	life-support systems
NASA	National Aeronautics and Space Administration
PSA	pressure-swing adsorption
SSE	sum of squares error
TSA	temperature-swing adsorption
TGA	thermogravimetric analysis

ABSTRACT

Author: Son, Karen, N. PhD
Institution: Purdue University
Degree Received: December 2018
Title: Improved Prediction of Adsorption-Based Life Support for Deep Space Exploration
Committee Chair: Suresh V. Garimella

Adsorbent technology is widely used in many industrial applications including waste heat recovery, water purification, and atmospheric revitalization in confined habitations. Astronauts depend on adsorbent-based systems to remove metabolic carbon dioxide (CO_2) from the cabin atmosphere; as NASA prepares for the journey to Mars, engineers are redesigning the adsorbent-based system for reduced weight and optimal efficiency. These efforts hinge upon the development of accurate, predictive models, as simulations are increasingly relied upon to save cost and time over the traditional design-build-test approach. Engineers rely on simplified models to reduce computational cost and enable parametric optimizations. Amongst these simplified models is the axially dispersed plug-flow model for predicting the adsorbate concentration during flow through an adsorbent bed. This model is ubiquitously used in designing fixed-bed adsorption systems. The current work aims to improve the accuracy of the axially dispersed plug-flow model because of its wide-spread use. This dissertation identifies the critical model inputs that drive the overall uncertainty in important output quantities then systematically improves the measurement and prediction of these input parameters. Limitations of the axially dispersed plug-flow model are also discussed, and recommendations made for identifying failure of the plug-flow assumption.

An uncertainty and sensitivity analysis of an axially disperse plug-flow model is first presented. Upper and lower uncertainty bounds for each of the model inputs are found by comparing empirical correlations against experimental data from the literature. Model uncertainty is then investigated by independently varying each model input between its individual upper and lower uncertainty bounds then observing the relative change in predicted effluent concentration and temperature (*e.g.*, breakthrough time, bed capacity, and effluent temperature). This analysis showed that the LDF mass transfer coefficient is the largest source of uncertainty. Furthermore,

the uncertainty analysis reveals that ignoring the effect of wall-channeling on apparent axial dispersion can cause significant error in the predicted breakthrough times of small-diameter beds.

In addition to LDF mass transfer coefficient and axial-dispersion, equilibrium isotherms are known to be strong lever arms and a potentially dominant source of model error. As such, detailed analysis of the equilibrium adsorption isotherms for zeolite 13X was conducted to improve the fidelity of CO_2 and H_2O on equilibrium isotherms compared to extant data. These two adsorbent/adsorbate pairs are of great interest as NASA plans to use zeolite 13X in the next generation atmospheric revitalization system. Equilibrium isotherms describe a sorbent's maximum capacity at a given temperature and adsorbate (*e.g.*, CO_2 or H_2O) partial pressure. New isotherm data from NASA Ames Research Center and NASA Marshall Space Flight Center for CO_2 and H_2O adsorption on zeolite 13X are presented. These measurements were carefully collected to eliminate sources of bias in previous data from the literature, where incomplete activation resulted in a reduced capacity. Several models are fit to the new equilibrium isotherm data and recommendations of the best model fit are made. The best-fit isotherm models from this analysis are used in all subsequent modeling efforts discussed in this dissertation.

The last two chapters examine the limitations of the axially disperse plug-flow model for predicting breakthrough in confined geometries. When a bed of pellets is confined in a rigid container, packing heterogeneities near the wall lead to faster flow around the periphery of the bed (*i.e.*, wall channeling). Wall-channeling effects have long been considered negligible for beds which hold more than 20 pellets across; however, the present work shows that neglecting wall-channeling effects on dispersion can yield significant errors in model predictions. There is a fundamental gap in understanding the mechanisms which control wall-channeling driven dispersion. Furthermore, there is currently no way to predict wall channeling effects *a priori* or even to identify what systems will be impacted by it. This dissertation aims to fill this gap using both experimental measurements and simulations to identify mechanisms which cause the plug-flow assumption to fail.

First, experimental evidence of wall-channeling in beds, even at large bed-to-pellet diameter ratios (d_{bed}/d_p=48) is presented. These experiments are then used to validate a method for accurately

extracting mass transfer coefficients from data affected by significant wall channeling. The relative magnitudes of wall-channeling effects are shown to be a function of the adsorption/adsorbate pair and geometric confinement (*i.e.*, bed size). Ultimately, the axially disperse plug-flow model fails to capture the physics of breakthrough when nonplug-flow conditions prevail in the bed.

The final chapter of this dissertation develops a two-dimensional (2-D) adsorption model to examine the interplay of wall-channeling and adsorption kinetics and the adsorbent equilibrium capacity on breakthrough in confined geometries. The 2-D model incorporates the effect of radial variations in porosity on the velocity profile and is shown to accurately capture the effect of wall-channeling on adsorption behavior. The 2-D model is validated against experimental data, and then used to investigate whether capacity or adsorption kinetics cause certain adsorbates to exhibit more significant radial variations in concentration compared than others. This work explains channeling effects can vary for different adsorbate and/or adsorbent pairs—even under otherwise identical conditions—and highlights the importance of considering adsorption kinetics in addition to the traditional d_{bed}/d_p criteria.

This dissertation investigates key gaps in our understanding of fixed-bed adsorption. It will deliver insight into how these missing pieces impact the accuracy of predictive models and provide a means for reconciling these errors. The culmination of this work will be an accurate, predictive model that assists in the simulation-based design of the next-generation atmospheric revitalization system for humans' journey to Mars.

1. INTRODUCTION

1.1 Background

Fixed-adsorbent beds are used for gas separations across a wide range of applications from industrial chemical processing and thermochemical energy storage to atmospheric revitalization in confined habitations.

1.1.1 Adsorption-based, gas separation

Separation processes transform a mixture of substances into two or more products that differ from each other in composition. The energy required to separate out constituents of a gas-mixture often accounts for the majority of the production costs in chemical and petrochemical industries [1]; thus, considerable effort is devoted to improving the efficiencies of separation processes. Adsorption-based technologies represented 11.2% of the approximately 75-billion-dollar global industrial gas separations and purification market in 2018 [2]. Adsorption is the adhesion of molecules to the surface of a solid. The solid is referred to as the adsorbent or simply the sorbent, and the constituent that adheres to the solid (*e.g.*, CO_2 or H_2O) is referred to as the adsorbate. Figure 1.1 shows several commercial sorbents produced by Honeywell UOP; these sorbents are made by mixing pure zeolite crystals (on the order of 10 μm in size) of with ~20% clay binder to form pellets (~2 mm in diameter).

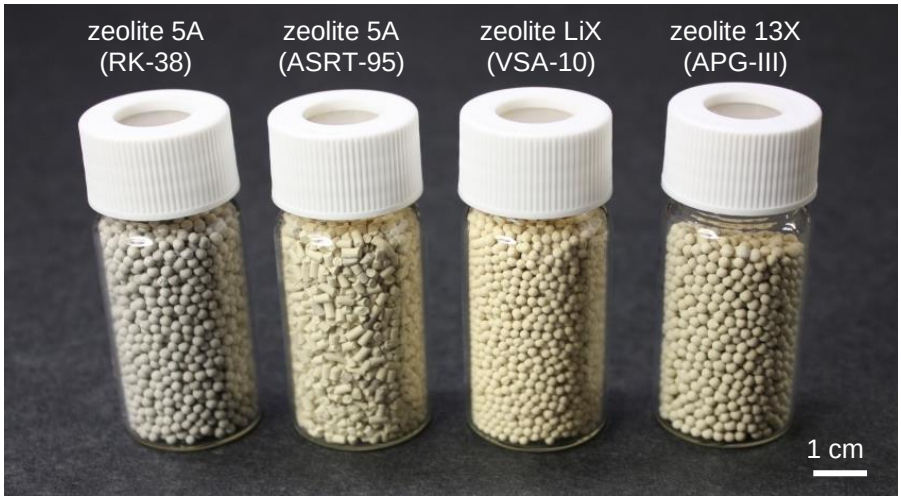

Figure 1.1. Photograph of several zeolite sorbents produced by Honeywell UOP.

Adsorption is reversible; meaning that the adsorbent can be regenerated and reused, and the adsorbed gas can be recovered. Adsorption-separation systems generally operate on multiple-bed, cyclic processes which allow for continuous flow of feed and product. In this structure, one bed will actively capture the adsorbate from the multicomponent feed, while another bed (previously saturated with adsorbate) is regenerated by heating and/or lowering the pressure. This system yields two products: the effluent of the first bed (*e.g.*, air without adsorbate) and the adsorbate coming off the second bed during regeneration. These systems are commonly categorized by the regeneration method, *e.g.*,

- temperature-swing adsorption (TSA),
- pressure-swing adsorption (PSA), and
- vacuum-swing adsorption (VSA).

VSA differs from PSA based on the range of pressures used in the cyclic regeneration. VSA processes adsorb at near-ambient (total) pressure and regenerate at sub-ambient pressures, while PSA processes typically operate at much higher range (*e.g.*, 0.1 to 10 MPa).

Adsorbents are increasingly used as a low-energy alternative to the traditional, cryogenic processes for separating the constituents of air. Air separation accounts for the second largest application of adsorbents at a projected 1.1 billion dollars in 2019 [3]. The market for adsorbents used in separating gaseous chemicals (including petrochemicals) is projected at an additional $250–$500 million in 2019 [4]. Different purification levels are required for different adsorption processes depending on the end use of the product gas; these processes are typically divided into bulk-separation and purification processes based on the influent concentration of adsorbate. While there is not a clear demarcation between these two categories, purification processes are generally defined as having an inlet adsorbate mass-fraction of 0.1 or less [5]. Purification processes are predominantly carried out in fixed-bed, temperature-swing adsorbers [5]. Traditionally, adsorbents were more commonly used for purification than bulk-separation. While this has changed with recent advances in pressure-swing adsorption that have enabled adsorbents to capture a large portion of the air-separation field, adsorbent-based gas-purification systems represent a significant market with growing applications [4]. Gas-purification processes include dehumidification, CO_2 removal, natural-gas purification, NO_x and SO_2 abatement, and remediation of nuclear effluent [1].

1.1.2 Atmospheric control in habitable volumes

Humans produce approximately one-kilogram of CO_2 per day. Plants metabolize CO_2 on-earth to maintain an atmospheric concentration of 40.9 kPa (403.3 ppm in 2016, as measured by the World Meteorological Organization [6]). In confined habitations, such as space vehicles, humans depend on Air-Revitalization-Systems (ARS) to remove this biotoxin. During the Apollo-era, astronauts used disposable lithium hydroxide (LiOH) canisters which react with CO_2, separating it from the O_2 and N_2 atmosphere. Unfortunately, each mission requires ~1.5 kg of LiOH per person-day; this large stowage requirement of LiOH (both in terms of mass and volume) precluded its use in long-duration missions. Thus, NASA switched to adsorbent-based CO_2 separation with the development of the first space station, Skylab, in the 1970's. Skylab marked the first use of a regenerable ARS in space. Skylab's multi-bed, PSA system formed the basis for the current ARS system aboard the International Space Station (ISS), the Carbon Dioxide Removal Assembly (CDRA).

The CDRA utilizes a fully regenerative vacuum/temperature-swing adsorption process (VTSA) to remove CO_2 from the ISS cabin air. The CDRA can remove 100% of the metabolic CO_2 generated by six crew members. It operates cyclically, employing two desiccant beds and two adsorbent beds. As one desiccant bed and one adsorbent bed operate in adsorption mode, the other two beds are desorbing (regenerating). Halfway through a cycle, the beds switch modes, providing continuous CO_2 removal capability. The CDRA uses 5A zeolite in the CO_2 sorbent bed and silica gel in the desiccant bed.

NASA's Life Support Systems (LSS) project, a part of the Advanced Exploration Systems program, aims to improve LSS "using the ISS's state-of-the-art hardware as a point of departure"[7]. Deep-space exploration places unprecedented demands on space-launch systems; vehicles will not only venture farther than any previous crewed mission, but they also must carry the supplies needed to sustain a crew for years without resupply. This new challenge places added importance on minimizing mass, volume and power loads for all spacecraft systems, including the LSS responsible for the removal of metabolic carbon dioxide (CO_2) from a crewed vehicle.

Two types of zeolite were used for the work in this dissertation, zeolite 5A and zeolite 13X. 5A and 13X are generic commercial names for zeolites with A- and X-type frameworks, respectively,

both with Na^+ as the major cation. Zeolite 13X has a higher capacity for CO_2 and water compared with zeolite 5A. Zeolite 13X is also commonly referred to as zeolite NaX, molecular sieve 13X, or simply 13X. Note that zeolite 13X and 5A are extensively used in current NASA systems for life support and will also be used in the next-generation adsorbent-based, life-support systems [8].

1.1.3 Simulation-based design of fixed-bed absorbers

Engineers increasingly rely upon simulations in designing adsorption systems to save cost and time over the traditional design-build-test approach. The LSS project also hinges upon the development of predictive simulation tools to reduce the hardware testing requirements in the design of the next generation of atmospheric-revitalization technology [9], [10]. Researchers at NASA's Marshall Space Flight Center have developed predictive models of the CDRA in efforts to create a virtual laboratory to optimize the design of the next-generation, air-revitalization system [10]. The model used in this dissertation follows the same physical assumptions used in the full CDRA, four-bed molecular sieve (4BMS) model [10], including the consideration of a nonconstant isosteric heat of adsorption which was a recently added improvement to the 4BMS model. This similarity allows for extrapolation of the results of this work to the full 4BMS model.

As direct numerical simulation of such multi-scale systems is computationally intractable, simplified models (*e.g.*, one-dimensional flow) are often employed to predict system performance. Furthermore, predictive models rely on accurate knowledge-based estimation of several model inputs (*i.e.*, free parameters). Models frequently depend on verified correlations to determine the mass and heat transfer coefficients *a priori*. Where accurate correlations of these free parameters are unavailable, multiple heat or mass transfer mechanisms are combined together into lumped-free parameters. One such reduction ubiquitously used in designing fixed-bed absorbers is the axially dispersed plug-flow model. This simplified model neglects radial variations (*e.g.*, in velocity, temperature, concentration) and lumps all the mechanisms which contribute to axial mixing (*e.g.*, turbulence, Taylor dispersion, and wall effects) into a single term called the axial-dispersion coefficient, D_{ax}.

1.1.4 Adsorption equilibrium and kinetics

There are three distinct mechanisms for adsorption separation: steric, kinetic, and equilibrium mechanisms. In steric separation, constituents of a mixture are separated by sorbent with uniform

aperture size in the crystalline microstructure. This microstructure permits small molecules to diffuse into the adsorbent while excluding larger molecules which pass through the bed without effect. Steric separation occurs in sorbents of precisely controlled microstructure, such as zeolites molecular sieves. Conversely, kinetic separation occurs in absorbents with a distribution of pore sizes which leads to differences in diffusion rates of different molecules. The equilibrium mechanism depends on the differing ability of adsorbates to accommodate each component of the mixture; the vast majority of adsorption separation processes use this mechanism [1].

Adsorption equilibria describe a sorbent's capacity to hold onto a specific species. For a given adsorbent/adsorbate pair, this equilibrium depends on the sorbent temperature and the gas-phase concentration of adsorbate (*i.e.*, the partial pressure of the adsorbate). The equilibrium adsorbed-phase concentration of adsorbate, n^*, is routinely approximated by an empirical fit to measured adsorption isotherms. Obtaining accurate isotherm measurements and fits is key to developing predictive simulations.

The kinetics of adsorption must also be accurately captured to develop truly predictive models. The linear-driving force (LDF) is commonly used to represent the kinetics of adsorption. The LDF approximation ignores the concentration gradient within a pellet and lumps all mass transfer resistances into a single term. It assumes that the adsorption rate ($\partial n/\partial t$) is linearly proportional to the difference between the adsorbate concentration in the gas phase, n, and the equilibrium adsorbed-phase concentration, n^*,

$$\frac{\partial n}{\partial t} = k_l \left(n^* - n \right) , \qquad 2.1$$

where the constant of proportionality, k_l, is termed the LDF mass transfer coefficient. While most model inputs can be accurately predicted with empirical correlations for the literature, k_l is very difficult to predict *a priori*; as such, k_l, is commonly found by fitting to bench-scale breakthrough tests and assumed to remain constant for scaled-up processes.

1.1.5 Breakthrough curves

Breakthrough tests are often performed on bench-scale adsorbent beds to extract mass-transfer information. Breakthrough experiments are commonly run in small-scale test beds to extract mass

transfer coefficients for subsequent use in models. In a recent survey of the literature on fixed-bed adsorption Knox [11] found that 11 of the 19 papers surveyed used breakthrough curve analysis to extract mass transfer rates. Furthermore, of the 19 papers only one considered a bed larger than 20 pellets in diameter. To perform a breakthrough test, the bed, which is initially devoid of adsorbate ($n = n^* = 0$ mol/kg), is exposed to an inlet flow of adsorbate in an inert carrier gas at $t = 0$. The inlet flow is maintained at a constant superficial velocity, temperature, and adsorbate partial pressure, while the outlet is maintained at a constant total pressure. The adsorbate is adsorbed by the sorbent as the gas mixture passes through the bed. Eventually, there is a small, but measurable quantity of adsorbate detected in the bed effluent. The time at which this occurs is termed the initial breakthrough time, t_b. For this dissertation, the breakthrough time is defined as the time at which the effluent concentration first reaches 1% of the influent concentration. The test continues until the bed is completely saturated, meaning that the effluent concentration matches the influent concentration to within 1%. Figure 1.2 illustrates the concentration of adsorbate (CO_2) in a sorbent bed at several important steps of a breakthrough test and indicates where these points occur on a breakthrough curve.

The breakthrough curve can be characterized by a few important times namely the initial breakthrough time (t_b), the 50% breakthrough time ($t_{0.5}$), the stoichiometric time (t_{stoich}), and the saturation time (t_{sat}). As stated above, the initial breakthrough time indicates when adsorbate is first detected in the effluent. Similarly, the $t_{0.5}$ indicates when the adsorbate concentration in the effluent reaches 50% of the inlet concentration (x/x_0=0.5). The stoichiometric breakthrough time represents the geometric mean of the integrated breakthrough curve as shown in Figure 1.2; note that the stoichiometric breakthrough time roughly coincides with $t_{0.5}$.

The relative importance of these characteristic times changes based on the end goal of the adsorption process. For example, the initial breakthrough time is of paramount importance when designing a purification process due to strict requirements on low adsorbate effluent concentrations. In contrast, a bulk separation process can continue until the bed is completely saturated. Therefore, the stoichiometric breakthrough time is more important than the initial breakthrough when designing for bulk separations.

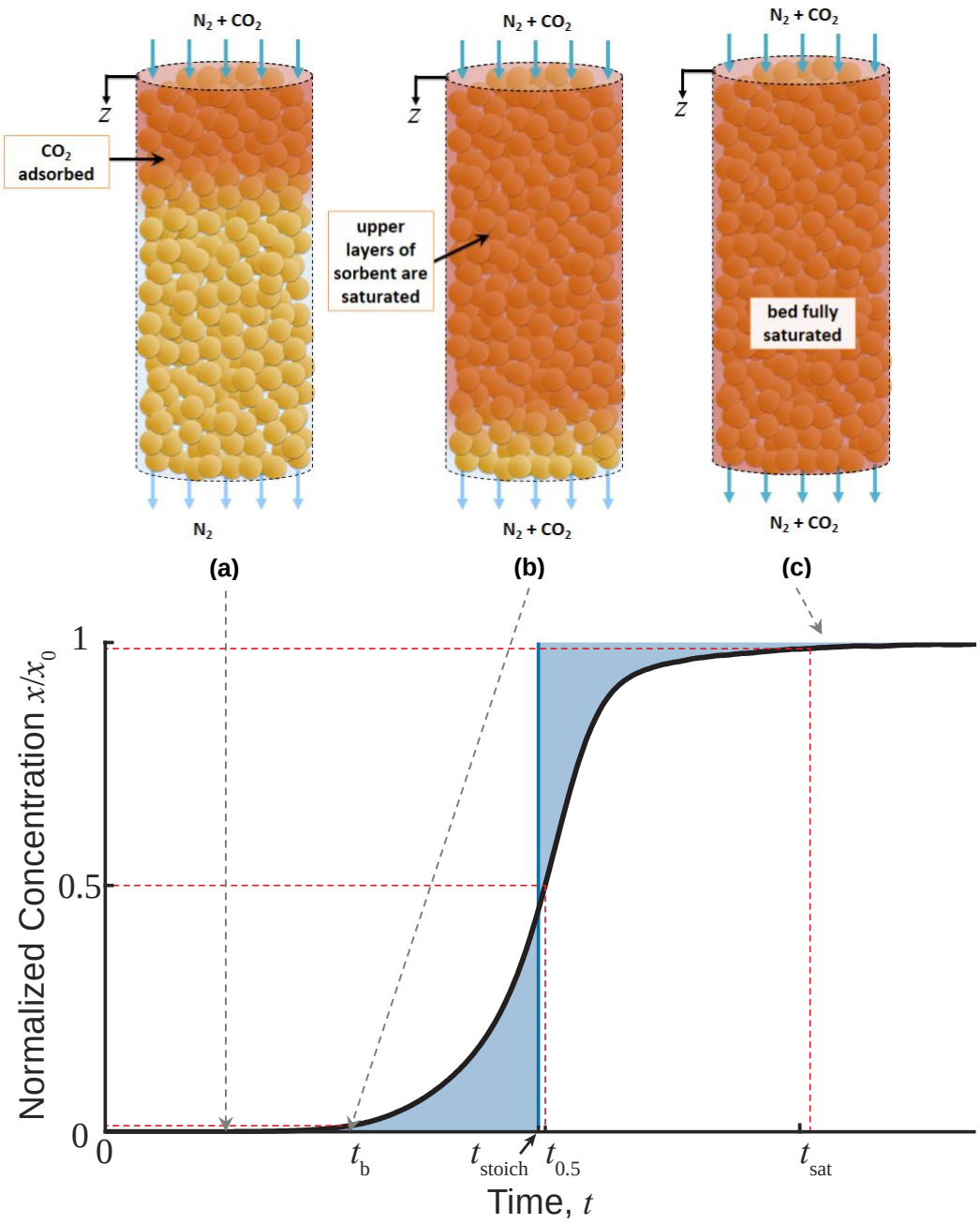

Figure 1.2. CO_2 breakthrough process in a sorbent bed. Illustrations of bed (top) show: (a) the CO_2 front progressing down the bed as the top of the sorbent bed becomes saturated, (b) breakthrough as the bed nears saturation, and (c) the fully saturated bed at the end of the test.

1.2 Literature review

Simulations are increasingly relied upon in designing adsorption systems to save cost and time over the traditional design-build-test approach. As direct numerical simulation of such multi-scale systems is computationally intractable, simplified models (*e.g.*, one-dimensional flow) are often employed to predict system performance. As such, many simplified models of the fixed-bed adsorption of have developed over the past several decades; improving the efficiency and accuracy of these predictive models is of great interest as we transition to a simulation-based design and optimization approach.

In a recent review of mathematical models for CO_2 adsorption in fixed-bed columns, Shafeeyan *et al.* [12] found that all most all works rely on two simplifying assumptions to decrease computational time:

1. the linear driving force (LDF) approximation and
2. negligible radial gradients with either plug flow or axially dispersed plug flow.

The LDF model (as originally proposed by Gleuckauf and Coates in 1947 [13]) is frequently used because it is analytical and simple yet still yields remarkably accurate results [14]. The assumption that the radial gradient in temperature, concentration, and velocity are negligible is also ubiquitously used. Approximately half of all studies Shafeeyan *et al.* [12] reviewed neglected axial dispersion entirely; the rest used empirical correlations to predict axial dispersion *a priori*. It was widely accepted that axial dispersion has minimal effect on adsorption models until Knox *et al.* (2016) published an experimental work investigating the effects of wall-channeling on apparent axial dispersion. Their work showed that correlations from the literature grossly underpredicted axial dispersion in small-diameter channels, leading to errors in fitted LDF coefficients of ~15% for CO_2 on zeolite 5A [15].

The remainder of this chapter reviews relevant literature related to the study of understanding and enhancing the accuracy of one-dimensional, fixed-bed adsorption models; specifically emphasizing CO_2 and H_2O adsorption on zeolite sorbents. The review is subdivided into sections which discuss:

1. sensitivity and uncertainty analyses of such models,
2. equilibrium adsorption isotherms

3. heat of adsorption
4. models for axial dispersion in adsorption systems, and
5. accounting for wall-channeling effects confined geometries.

This body of literature is key to the understanding of fixed-bed adsorption and vital background for developing a predictive adsorption model.

1.2.1 Sensitivity and uncertainty analysis of fixed-bed absorbers

In general, the sensitivity of one-dimensional, fixed-bed adsorption models is well understood. Adsorption equilibria, mass-transfer rates, and process parameters (*e.g.*, flow rate, inlet concentration, bed length) are known to be strong lever arms [16]. There are comparatively fewer studies which analyze the uncertainty of adsorption models due to errors in empirically predicted inputs such as heat and mass transfer parameters. Most such studies focus on the effect of uncertainties in mass transfer parameters on the breakthrough curve. Refs. [17]–[31] used models which account for both interparticle and intraparticle transport, and compared the relative sensitivities of multiple mass transfer parameters to determine the dominant mass-transfer mode(s). These studies found that model results are sensitive to mass transfer coefficients and generally, there is a single, dominant mass-transfer mode to which the model is most sensitive. It is well known that intraparticle diffusion can be ignored and the mass-transfer resistance can be approximated by a single parameter termed the linear-driving-force (LDF) coefficient when one mass-transfer mode dominates [32]. Refs. [33]–[39] evaluated the sensitivity of the breakthrough curve to this LDF coefficient. The LDF approximation is widely used both in the literature and in industry as a simplified representation of the mass transfer process in fixed-bed adsorption with good results as there is generally one dominant mass-transfer resistance [40],[12]. Regardless of the mass-transfer model, it is generally accepted that one-dimensional, fixed-bed adsorption models are sensitive to the mass transfer coefficients if the process is far enough away from the extreme limit of local gas-sorbent concentration equilibrium.

Other studies focus on the sensitivity of adsorption models to equilibrium isotherm parameters. This includes investigations on the effect of different isotherm types (*e.g.*, linear versus Langmuir, multi-component versus single-component) [16]. It has generally been concluded that nonlinear isotherms are required to model adsorption with a reasonable degree of fidelity [34],[36], and that

adsorption is highly sensitive to isotherm parameters while desorption is insensitive [36]. A large number of studies investigated only the effect of varying the isotherm parameters for a single isotherm model; Refs. [17], [18], [20], [33], [36], [39], [41] studied the effect on quantitative metrics such as breakthrough time, while Refs. [19], [27], [33]–[35], [42]–[44] evaluated model sensitivity by observation of changes in the slope or position of breakthrough curves. Most of these studies ([17]–[19], [34], [35], [39]) evaluated model sensitivities to the Freundlich isotherm parameters. Others investigated sensitivity to the Langmuir isotherm parameters [43], the Langmuir-Freundlich (*i.e.*, Sips) isotherm parameters [20], [27], or the Toth isotherm parameters [33], [44]. Despite the wide variety of systems and isotherm types considered in these studies, there is a consensus in the literature that one-dimensional, fixed-bed adsorption models are sensitive to both the type of isotherm used (*e.g.*, Freundlich, Langmuir, Toth) and to uncertainties in the empirically determined isotherm parameters[1].

Conclusions in the literature regarding sensitivity to axial dispersion are less consistent; while many researchers concluded that adsorption models are insensitive to axial dispersion ([18], [19], [24], [26], [28], [34], [39], [42]), others found the opposite to be true ([15], [30], [37], [38]). Yet others are equivocal in their conclusions. For example, Borina and Pavko [45] note that sensitivity to axial dispersion is a complex function of process parameters such as bed length and flow rate. They found that breakthrough time was insensitive to axial dispersion for a short bed at low velocity (L = 180 cm, $u_\infty = 4.1\times10^{-5}$ m/s) but highly sensitive to axial dispersion for a longer bed at high velocity (L = 1000 cm, $u_\infty = 4.1\times10^{-2}$ m/s). Lu *et al.* [37] found that sensitivity to axial dispersion also depends on the criteria used to define breakthrough time (x/x_0 = 2%, 50%, or 98%), with lower breakthrough concentration criteria (*i.e.*, x/x_0 = 2%) causing the model to be most sensitive to axial dispersion. They concluded that sensitivity to axial dispersion becomes important relative to other parameters as the requirements on effluent concentration become more stringent.

Most of these studies used empirical correlations to predict the axial dispersion coefficient. There are many such correlations (both empirical and semi-empirical) which allow researchers to directly predict the axial dispersion of their system without comparing their model directly to experimental data or higher-fidelity simulations. However, none of these correlations account for every possible mechanism of axial dispersion. Therefore, some researchers have focused on the effect of using

such predictions of axial dispersion on subsequently fit model parameters (*e.g.*, LDF mass transfer coefficient). Axial dispersion is a complex function of flow conditions and bed geometry, with available correlations spanning several orders of magnitude in their predictions [46], [47]. Furthermore, the available empirical correlations do not account for wall channeling, causing them to drastically underpredict the apparent axial dispersion in small-diameter beds, such as those used in laboratory experiments to obtain fitted parameters [15], [38]. Knox *et al.* [15] investigated the effect of using such empirical correlations to predict axial dispersion when fitting a one-dimensional, fixed-bed adsorption model to typical lab-scale, experimental-breakthrough data. They found that using empirical prediction of axial dispersion fitted to the effluent caused an error in LDF coefficient, and proposed an experimental method for reducing this error using in-bed centerline concentration measurements where the near-wall apparent dispersion effects are minimized.

Compared to the wealth of literature on equilibrium and kinetic parameters for mass transfer, relatively few papers have considered sensitivity to heat transfer parameters ([34], [36], [43], [48]–[51]). This is partially due to the simplifying assumption made in many studies ([17]–[31], [37]–[39], [42], [44], [45]) to neglect heat transfer and treat the entire bed as isothermal. This assumption is made even though system-level models of cyclic pressure and temperature-swing-adsorption processes are known to be highly sensitive to temperature [33]. Even studies that account for heat transfer rely on assumptions such as adiabatic walls ([34], [43], [49], [51]), constant isosteric heat of adsorption ([48], [50]), or local thermal equilibrium (LTE) ([34], [41], [48], [49], [51]). Sircar [48] evaluated the adiabatic wall assumption and concluded that while the breakthrough time is insensitive to the ambient heat loss, the profile of concentration in the bed depends strongly on this quantity. Furthermore, using an adiabatic boundary condition induced considerable error when fitting equilibrium capacity and the kinetic parameters, even when the temperature change in the column is small. In another study, Sircar [50] studied the effect of the fluid-solid heat transfer coefficient on the performance of a pressure swing adsorption system by modeling a single particle and concluded that the LTE assumption is appropriate at high Nusselt numbers ($Nu > 6$). Walton and LeVan [51] showed that assuming a constant isosteric heat of adsorption had minimal impact on plateau temperature, partial pressure, and loading, but a significant impact on breakthrough time compared with temperature-dependent models. The most dramatic difference was observed

at the highest adsorbed-phase heat capacity where approximating the isosteric heat as constant led to a severely overestimated breakthrough time.

1.2.2 Equilibrium adsorption isotherms

Knowledge of single-component, equilibrium adsorption isotherms is critical to the design of pressure-swing adsorption (PSA) and temperature-swing adsorption (TSA) systems. Accurate measurements of CO_2 isotherms are required for a broad range of applications, from greenhouse gas remediation to atmosphere revitalization. Another adsorbate/adsorbent pair that is of great interest is H_2O on zeolite 13X. Many industrial processes (*e.g.*, natural gas purification process [52]) use zeolite 13X to remove water vapor from gas streams. Removing water from gas streams reduces the potential for several undesirable effects, such as hydrate formation, corrosion, and condensation or freezing of moisture [53]. Moisture removal is also an important precursor to adsorption of other constituents; of particular concern to the present work is the use of adsorbent beds to dehumidify the cabin air of spacecraft prior to carbon CO_2 removal [54], [55].

Accurate adsorption equilibrium data of CO_2 and H_2O on zeolite 13X are needed across a wide range of temperatures and pressures to enable these predictive simulations. Though many studies have published data for CO_2 and H_2O adsorption, discrepancies in reported isotherms are common in the literature due to variability in the adsorbents tested and differences in measurement procedures [56]. While in principle the measurement is straightforward and can be accomplished using a variety of commercially available or custom-built instruments, in practice, it is challenging to obtain repeatable and accurate measurements. Correct measurements are especially challenging to obtain at low vapor pressures and loadings, due to finite instrument sensitivities and the difficulty of verifying complete activation of the adsorbent. It is also difficult to determine when equilibrium has been reached in many measurement instruments.

In 2009, Wang and LeVan [57] published several isotherms for CO_2 and H_2O adsorption on Grace Davidson zeolite 5A and 13X. While these data spanned a wide range of temperatures (−50 °C to 175 °C) and pressures (0.07 kPa to 85 kPa) useful for many PSA and TSA applications, their activation temperature (175 °C) was too low to completely remove residual water loading [58]. As a result, their isotherms measured an erroneously reduced capacity. Brandani and Ruthven [59]

documented the effect of small quantities of water on the CO_2 capacity in several different forms of zeolite X. They found residual water loading on NaLSX sorbent at temperatures as high as 220 °C; increasing the temperature to 350 °C resulted in complete H_2O removal. This agrees with later work performed at NASA [58] which showed that an activation temperature greater than 300 °C was required to completely remove residual water loading. NASA has depended on published isotherms, such as those of Wang and LeVan [57], to model adsorbent-based life support systems which operate on PSA and TSA cycles to revitalize the cabin atmosphere of space vehicles. However, unresolved discrepancies between model predictions and experiments necessitated the development of new equilibrium adsorption isotherms for CO_2 and H_2O adsorption on zeolite 13X.

1.2.3 Heat of adsorption

The heat of adsorption is another important parameter for modeling PSA and TSA processes [60] and is often used as an essential screening metric for assessing different sorbent materials for a specific application [60]–[63]. Despite its importance, the heat of adsorption is rarely measured directly [64] but is rather predicted from equilibrium isotherms using the Clausius–Clapeyron equation [16], [65]. While a handful of studies have used microcalorimetry to measure the heat of adsorption of CO_2 on 13X at a single temperature ([66]–[73]), none have measured the heat of adsorption of CO_2 on 13X as a function of temperature. Llewellyn *et al.* [74] investigated the effect of temperature on the heat of adsorption of N_2 and Ar on NaX and DAY and found that the polar interactions of the N_2/NaX system caused significant variations in the heat of adsorption with temperature. Given that the electric quadrupole moment in the CO_2 molecule interacts very strongly with the cations present in the zeolite 13X crystals, there is reason to believe that temperature may affect the heat of adsorption of CO_2 on 13X.

1.2.4 Models for axial dispersion in adsorption systems

Actual fixed-beds of adsorbents consist of a random packing of polydisperse sorbent particles. This stochastic structure naturally results in a flow field with dispersive attributes. Dispersion in the bed can include turbulence, flow splitting and rejoining around particles, Taylor dispersion, channeling (due to radial variations in bed void fraction), and wall effects. Numerous correlations are available in the literature which predict axial (D_{ax}) and radial (D_r) dispersion *a priori* from particle Peclet number, velocity, and pellet diameter (see the reviews of Delgado [46], [47]).

Unfortunately, none of these correlations account for all dispersive mechanisms, and there is significant variation between their predictions.

Generally, the dispersion is considered a secondary effect and is commonly neglected from adsorption models [12]. Recent work by Knox *et al.*[11], [15] compared the *a priori* prediction of the axial dispersion coefficient, D_{ax}, from available correlations to measured dispersion from experimental breakthrough data and the examined in detail the potential consequences of using *a priori* prediction of D_{ax}. They found that measured axial dispersion was an order of magnitude higher than correlations would predict. This finding was attributed to channeling effects which inflate axial-dispersion in a one-dimensional model. Furthermore, Knox *et al.* [11], [15] examined the effect of the large measured D_{ax} on fitting an axially dispersed plug-flow model with the Danckwerts outlet boundary to breakthrough data to extract LDF coefficient. They found that using empirical correlations to predict D_{ax} can result in erroneous extraction of the LDF mass transfer coefficient from experimental breakthrough data. Knox *et al.* [11], [15] concluded that, contrary to prior works, axial dispersion should be considered in systems when extracting LDF from laboratory-scale experiments.

1.2.5 Wall-channeling in confined geometries

When a bed of pellets is confined in a rigid container, packing heterogeneities near the wall lead to faster flow around the periphery of the bed (*i.e.*, wall channeling). As the bed-to-pellet diameter ratio increases, the fraction of the flow affected by wall channeling decreases. Thus, while radial flow variations are known to exist in fixed-beds [75], it is generally accepted that their effects can be safely neglected for sufficiently large beds. “Sufficiently large” is generally defined as beds with a diameter at least twenty times greater than the adsorbent pellet diameter [76] ($d_{bed}/d_p \geq 20$).

While a bed-to-pellet diameter ratio of 20 is generally considered to be large enough to ignore the effects of near-wall channeling [76], recent studies by Knox and coworkers ([11], [15], [77], [78]) have indicated that wall channeling can affect apparent axial dispersion at values of d_{bed}/d_p even as large as 48. Researchers routinely use bench-scale adsorption beds to measure breakthrough curves for calibrating mass transfer coefficients with highly confined beds ($d_{bed}/d_p < 20$)[79]. This approach relies on correlations to predict the axial-dispersion coefficient *a priori*; while several

such correlations exist [46], none of these pellet-driven dispersion correlations account for the effects of nonplug flow. Inaccurate prediction of D_{ax}—due to the prevalence of nonplug-flow conditions—can lead to significant errors in the mass transfer coefficients fitted to breakthrough curves from such highly confined experiments [15], [78].

To circumvent the lack of available correlations for nonplug flow, Knox *et al.*[15] proposed a new experimental method that allows for independent extraction of the LDF mass transfer coefficient and the apparent axial-dispersion coefficient using two sampling locations: (1) a centerline sampling location embedded close to the end of the bed and (2) a downstream sampling location which measures the mixed-exit concentration. The intrabed, centerline location is assumed to be sufficiently far from the walls that it is not influenced by the nonplug-flow effects on axial dispersion. Thus, extant correlations for pellet-driven dispersion can be used to extract the mass transfer coefficient. Once the mass transfer coefficient is extracted from the centerline data, the mixed-exit data can be used to find the apparent axial dispersion, a term which incorporates the effects of nonplug-flow conditions that are prevalent in highly confined beds.

Two approaches have been used when near-wall-channeling effects play a significant role in the hydrodynamics. The first approach maintains the plug-flow assumption and uses a larger, apparent axial dispersion to account for the wall-channeling effects (*e.g.*, Knox *et al.*[15]). The second approach uses two-dimensional simulations to account for the radial distribution of velocity (*e.g.*, Augier *et al.*[79]). Despite the increased accuracy of 2-D simulations, 1-D simulations are still widely used to reduce computational expense. This dissertation uses both approaches to examine what mechanisms cause the plug-flow assumption to fail and under what circumstances modelers need to consider higher-order effects.

1.3 Objectives

The primary objective of this dissertation is to improve the accuracy of axially dispersed plug flow adsorption model. This simplified model is the cornerstone of NASA's simulations which will be used to design the next-generation LSS for deep-space exploration. This dissertation aims to identify the critical model inputs that drive the overall model uncertainty then systematically improve the measurement and prediction of these key input parameters.

The first objective is to identify critical model inputs. Axially dispersed plug flow adsorption models have been shown to be highly sensitive adsorption isotherms, mass transfer coefficients, and several operating parameters (*e.g.,* flow rate); however, the effects of uncertainty in model inputs on overall model uncertainty is not well understood. This dissertation includes a detailed comparison of empirically predicted input parameters to experimental measurements from the literature to determine the uncertainty in each predicted parameter. Such an analysis of these parameters (*e.g.*, effective axial thermal conductivity) is unavailable elsewhere in the literature. Prior work in the literature also fails to investigate the effect of wall channeling on breakthrough curve uncertainty. In particular, the influence of wall channeling on the apparent axial dispersion is not considered. The present work accounts for axial dispersion, including the effects of wall channeling on axial dispersion. This is accomplished by calibrating the model against experimental data from intra-bed centerline concentration measurements to find the LDF coefficient. This LDF coefficient is then used to extract axial dispersion coefficients from mixed, downstream concentration measurements for both a small-diameter bed (dominated by wall-channeling) and a large-diameter bed (dominated by pellet-driven dispersion). The subsequent sensitivity and uncertainty analysis which model inputs most strongly impact the predicted effluent concentration and temperature profiles.

Before investigating other model inputs, it is necessary to determine an accurate model of the equilibrium adsorption isotherms for CO_2 and H_2O on zeolite 13X. Equilibrium isotherms are known to be strong lever arms and a potentially dominant source of model error. The capacity of this sorbent/adsorbent pair is of great importance to NASA as the next generation atmospheric revitalization system will most likely use zeolite 13X. As such, this dissertation seeks to improve the fidelity of equilibrium isotherms for CO_2 and H_2O on zeolite 13X compared to extant data. New adsorption isotherms are reported for pure CO_2 on zeolite 13X over a temperature range of 0 °C to 200 °C and pressure range of 0.001 kPa to 100 kPa. Similarly, isotherms for water adsorption on zeolite 13X are measured at 25 °C, 35 °C, 50 °C, 70 °C, and 100 °C and at equilibrium pressures ranging from 0.006 kPa to 25 kPa. These pure component equilibria are fit with several models to determine the best expression for modeling the capacity as a function of temperature and pressure. This best-fit isotherm model from this analysis is now used NASA's adsorption simulations and in all subsequent modeling efforts discussed in this dissertation.

Both LDF mass transfer coefficient and axial dispersion were shown to be important model inputs based on the uncertainty analysis in this dissertation. Thus, a primary objective of this dissertation is improving the measurement and prediction of LDF and axial dispersion coefficients to reduce overall model uncertainty. Previously, the effect of axial dispersion on breakthrough curves was thought to be minimal; axial dispersion is commonly neglected by modelers and those who do consider it use empirical predictions to predict it *a priori*. Recent work by Knox *et al.* [15], showed that the effects of wall-channeling on apparent axial dispersion could not be neglected even when the bed-to-pellet diameter ratio exceeded 20. This result contradicts the consensus in the literature for when wall-effects can be neglected. Furthermore, there is considerable variance not only in the values obtained from *a priori* predictions but also in the physical dispersion mechanisms each correlation considers. There is a gap in basic understanding of what mechanisms dominate axial dispersion, and this dissertation aims to close this gap.

A dual experimental/numerical study is conducted to narrow this gap by evaluating the ability of the axially disperse plug-flow model to accurately predict breakthrough in confined geometries. The axially disperse plug-flow model is used to independently extract mass transfer and axial-dispersion coefficients from breakthrough experiments via centerline and mixed-exit concentration measurements, respectively. Four experimental cases are considered: breakthrough of carbon dioxide (CO_2) and water (H_2O), in two cylindrical beds of zeolite 13X (NaX) each. The adsorbate concentration is monitored both within the bed (centerline) and after the bed (mixed exit) throughout each experiment. Mass transfer and axial-dispersion coefficients are then independently extracted by fitting to the intrabed centerline and mixed-exit breakthrough curves respectively. The mass transfer coefficient extracted by fitting to the intrabed, centerline breakthrough curve is shown to be independent of bed size, even when $d_{bed}/d_p=17$. The extracted axial-dispersion coefficients are compared to the predictions of existing correlations for mechanical dispersion that do not account for the effects of wall channeling, and thereby grossly underpredict the apparent axial dispersion observed in the bed. The relative magnitudes of wall-channeling effects are shown to be a function of the adsorption/adsorbate pair and geometric confinement (*i.e.*, bed size). Ultimately, the axially disperse plug-flow model fails to capture the physics of breakthrough when nonplug-flow conditions prevail in the bed.

Lastly, a two-dimensional adsorption model is used to examine the interplay of wall-channeling and adsorption kinetics/equilibrium on breakthrough in confined geometries which caused the 1-D model to fail. The effect of radial variations in porosity on velocity and concentration profiles is described. The 2-D simulation results are validated against experimental data and then compared to 1-D results to illustrate the need to account for these radial variations. The validated 2-D model is then used to investigate causes H_2O to exhibit more significant radial variations in concentration compared with CO_2 breakthrough.

This dissertation aims to reduce error in adsorption models by improving the measurement and prediction of several key model inputs. These results that are of great need to the adsorption community which depends upon precise knowledge of these input parameters for predictive models. This work directly addresses the need to improve model accuracy as industry increasingly relies on simulation-based design. This dissertation also provides a necessary investigation of the limitations of the axially disperse plug-flow model on predicting breakthrough in confined geometries *via* a combined experimental and simulation approach.

1.4 Organization of dissertation

The work presented in this dissertation is organized into eight chapters. Chapter 1 introduces fixed-bed adsorption and provides motivation for the dissertation work. Chapter 2 reviews the relevant literature. Chapter 3 presents a detailed investigation of the uncertainty of a fixed-bed adsorption model. This chapter includes details on the development of the one-dimensional model including the calibration method and source of model inputs. Novel isotherm fits for CO_2 and H_2O on zeolite 13X are presented in Chapter 4 and Chapter 5, respectively. Chapter 6 presents experimental measurements of centerline and mixed-exit concentration for CO_2 and H_2O breakthrough on zeolite 13X in two adsorbent beds and examines the limitations of the axially dispersed plug-flow model in predicting breakthrough in confined geometries. A 2-D model is developed in Chapter 7 to examine the interplay of wall-channeling and adsorption kinetics and capacity on breakthrough in confined geometries which caused the 1-D model to fail in Chapter 6. Finally, Chapter 8 summarizes the conclusions of this dissertation.

2. CALIBRATION AND UNCERTAINTY ANALYSIS OF A FIXED-BED ADSORPTION MODEL FOR CO_2 SEPARATION

Understanding the accuracy of predictive adsorption models is increasingly important as we transition to a simulation-based design and optimization approach. A comprehensive uncertainty analysis accounting for contributions from all the input parameters of a model that does not make simplifying thermal assumptions is lacking in the literature. We address this deficit in this chapter. A high-fidelity model of cylindrical adsorbent beds is developed which accounts for axial dispersion, local thermal nonequilibrium, nonlinear Toth isotherms, thermodynamically derived heats of adsorption, and temperature-dependent properties. We then follow the calibration method prescribed by Knox *et al.* [15] to independently determine the mass transfer rate (*i.e.*, LDF coefficient) and the axial dispersion coefficient. Upper and lower uncertainty bounds for each of the model inputs are found by comparison of experimental data from the literature to empirical correlations. Model uncertainty is then investigated by independently varying each model input between its individual upper and lower uncertainty bounds and observing the relative change in important output quantities.

The predicted effluent concentration and temperature profiles are most strongly affected by uncertainty in LDF coefficient, sorbent density, and void fraction. The uncertainty analysis further reveals that ignoring the effect of wall-channeling on apparent axial dispersion can cause significant error in the predicted breakthrough times of small-diameter beds. The material presented in this chapter was published in *Adsorption* [78].

2.1 Experimental facility

The fixed-bed adsorption breakthrough experiments of Knox *et al.* [11], [15] and Son *et al.* [80] are used in this chapter for model calibration. Cross-sectional drawings of the two test stands from these experiments, respectively called test stand A and B in this chapter, are shown in Figure 2.1 and their physical properties are listed in Table 2.1. Test stand A holds a 254 mm (10 in) long sorbent bed sandwiched between two layers of glass beads, each 127 mm (5 in) long. This bed is housed in a 47.6 mm (1.87 in) inner diameter canister, which equates to roughly 24 sorbent pellets

across the inner canister diameter. The sorbent bed in test stand B is shorter at 165 mm (6.5 in) in length, but is held in a much larger inner canister diameter of 93.6 mm (3.68 in), approximately 42 pellets across. For both test stands, five exposed-tip thermocouples measure the gas-stream temperatures upstream and downstream of the bed, and at three centerline locations within the sorbent bed, as shown in Figure 2.1.

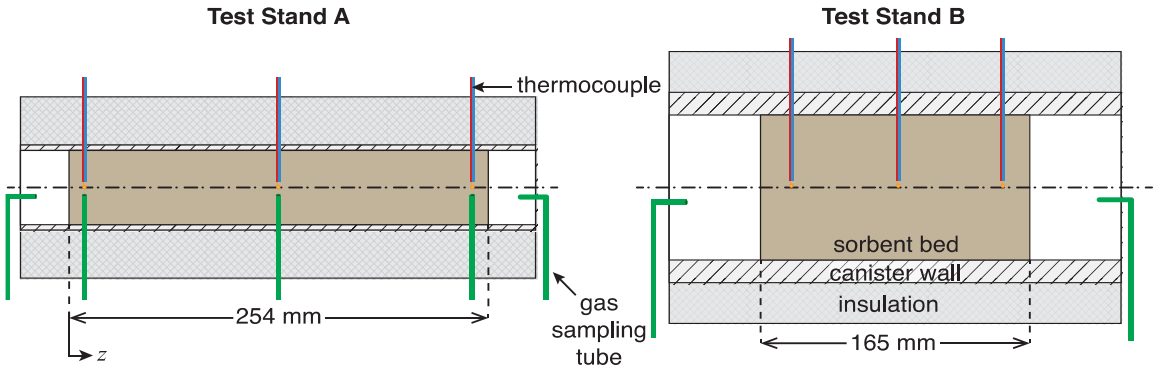

Figure 2.1 Cross-sectional views of the cylindrical canister and sorbent bed for test stand A and test stand B, showing the axial locations of intra-bed temperature and CO_2 sensors. Note that the inlet and outlet gas sampling tubes are physically located far away from the sorbent.

Table 2.1. Dimensions and physical properties of the test stand A [15] and B [80].

		Test stand A	**Test stand B**
bed length, L, m		0.254	0.165
void fraction, ε		0.35	0.35
inner canister diameter, $d_{can,in}$, mm		47.6	93.6
sorbent:	material	Grace Davidson grade 522[81]	UOP RK-38[82]
	mean pellet diameter, d_p, mm	2.32	2.1
	conductivity, k_s, W/(m K)	0.152	0.144
	heat capacity, $c_{p,s}$, J/(kg K)	920	650
	pellet envelope density, ρ_{env}, kg/m^3	1180	1179
canister:	material	stainless steel	aluminum
	thickness, t_{can}, mm	1.59	10.3
	conductivity, k_{can}, W/(m K)	14.2	205
	heat capacity, $c_{p,can}$, J/(kg K)	475	902
	density, ρ_{can}, kg/m^3	7833	2712
insulation:	material	Q-fiber®[83] and min-K®[84]	Pyropel® LD-6[85]
	thickness, t_{ins}, mm	25.4	15.9
	conductivity, k_{ins}, W/(m K)	0.038	0.032
	heat capacity, $c_{p,ins}$, W/(m K)	747	747
	density, ρ_{ins}, kg/m^3	88	100

The thermocouples in test stand A are factory calibrated T-type thermocouples (±1 °C accuracy). Test stand A is instrumented with a gas chromatograph (Shimadzu GC-14A with CR601 integrator, ±1.2% of reading uncertainty [11]) which monitors the centerline CO_2 concentration at five axial locations: (1) upstream of the bed, (2) 6.5 mm from the inlet of the bed (*i.e.*, 2.5% of the total bed length), (3) the middle of the bed, (4) 6.5 mm from the exit of the bed, and (5) far downstream of the bed. Total pressure was measured at each of these five-sampling locations in test stand A (Viatran pressure transducer, 0-30 psia range, and ±0.25% full-scale range uncertainty) which was connected to the gas sampling line during a separate pressure-drop test run at the same flow rate used for the breakthrough experiments. The thermocouples in test stand B are calibrated to measure temperature to within ±0.2 °C uncertainty using a dry-block calibrator with RTD sensor. Test stand B is instrumented with two continuous-sampling, infrared CO_2 sensors placed upstream and downstream of the bed (Sable Systems CA-10 CO_2 Analyzer, ±1% of reading accuracy over a range of 0-5% CO_2 by volume). In test stand B, the total pressure is measured before and after the bed by two absolute pressure transducers (Honeywell FP2000, 2-172 kPa range and ±0.10% full-scale range uncertainty) in real-time throughout the breakthrough experiment.

Detailed descriptions of the test stands and experimental methods can be found in Refs. [15], [11], and [80]. To match conditions in the CDRA, the experiments use zeolite 5A sorbent at similar superficial velocity (0.28 m/s) and inlet temperature (300 K) during breakthrough. The bed diameters, however, are significantly larger at ~20 pellets across for the bed in test stand A and ~42 pellets across for the bed in test stand B; thus, we expect that the empirically fit axial dispersion coefficients will be much lower than the axial dispersion in a CDRA channel with ~6 pellets across the bed, where flow channeling, caused by low porosity near the wall, dominates the axial mixing and leads to a high apparent dispersion. Breakthrough test data can be used to calibrate the mass transfer (LDF) coefficient and dispersion coefficient. To perform breakthrough tests, the beds, which are initially filled with only N_2, are exposed to an inlet flow of N_2 and CO_2 at $t = 0$. The inlet flow is maintained at a superficial velocity of 0.28 m/s and constant CO_2 partial pressure, while the outlet is maintained at a constant total pressure. The CO_2 is adsorbed by the sorbent as the gas mixture passes through the bed. Eventually, there is a small, but measurable quantity of CO_2 detected in the bed effluent. The time at which this occurs is termed the initial breakthrough time, t_b. For the purpose of this dissertation, the breakthrough time is defined as the time at which

the effluent concentration first reaches 1% of the influent concentration, c_0. The test continues until the bed is completely saturated, meaning that the effluent concentration matches the influent concentration to within 1%. This occurs at approximately t = 2 h.

2.2 Modeling approach

An axially dispersed plug-flow reactor model is developed based on the cylindrical bed geometries shown in Figure 2.1. We model the breakthrough process as described in section 2.1 above. The model is quasi-one-dimensional in that the temperature of the four separate constituents (gas phase, sorbent, canister wall, and insulation) can differ at the same axial position and are coupled via heat transfer coefficients. Thus, the model requires four separate energy balances, one for each constituent. The model additionally requires two mass balances for the gas phase and adsorbed CO_2 phase. These six governing equations (two mass balances and four energy balances) are coupled and solved to obtain the CO_2 concentrations and temperatures as a function of time and axial position.

2.2.1 Adsorbed-phase mass balance

The adsorbed phase concentration is computed using the linear-driving-force (LDF) approximation [13]. The physical process of adsorption is controlled by several mass transfer resistances, including macropore, micropore, and surface diffusion. The LDF approximation ignores the concentration gradient within a pellet and lumps these resistances into a single term. It is assumed that the adsorption rate ($\partial n/\partial t$) is linearly proportional to the difference between the adsorbate concentration in the gas phase, n, and the equilibrium adsorbed-phase concentration, n^*, as

$$\frac{\partial n}{\partial t} = k_l \left(n^* - n \right) \tag{2.1}$$

where the constant of proportionality, k_l, is termed the LDF mass transfer coefficient. The equilibrium adsorbed-phase concentration, n^*, corresponds to the CO_2 partial pressure, p_{CO_2}, at the adsorbent temperature, T_s, based on the equilibrium adsorption isotherm as described in Section 0 below. The bed is assumed to be initially devoid of CO_2 (*i.e.*, $n(t = 0) = 0$).

2.2.2 Gas-phase mass balance

The gas-phase mass balance is coupled with the adsorbed-phase mass balance via the rate of adsorption. This balance also accounts for advection and axial dispersion through the bed as

$$\frac{\partial c}{\partial t}+\left(\frac{1-\varepsilon}{\varepsilon}\right)\frac{\partial n}{\partial t}-D_{\text{ax}}\frac{\partial^2 c}{\partial z^2}=-\frac{\partial(u_{\text{i}}c)}{\partial z} \qquad 2.2$$

where c is the gas-phase concentration of the adsorbate (*i.e.*, CO_2). The axial dispersion coefficient, D_{ax}, is calculated from the parametric equation of Edwards and Richardson [86] as described in Section 2.2.4. We represent the experimental boundary conditions in our model with a constant flux boundary condition at the inlet and the Danckwert's boundary condition at the outlet, respectively defined as

$$-D_{\text{ax}}\left.\frac{\partial c}{\partial z}\right|_{z=0}=\frac{u_{\text{s,in}}}{\varepsilon}\left(c_0-c\right) \quad \text{and} \quad \left.\frac{\partial c}{\partial z}\right|_{z=L}=0\ . \qquad 2.3$$

2.2.3 Energy balances

Separate energy balance equations for the gas, adsorbent, canister wall, and insulation are included in the model to account for local thermal nonequilibrium. An analysis of the time constants for energy flow between these four constituents indicates that none can be neglected. It is critical to account for diabatic effects due to the large thermal mass of the container. All four energy balances account for transient heat storage and heat transfer between the separate regions. In addition to these terms, the adsorbent energy balance includes a heat of adsorption term that accounts for the exothermic and endothermic nature of adsorption and desorption, respectively.

The gas-phase energy balance includes transient heat storage, axial dispersion, advection, and convective heat transfer to the adsorbent and canister wall,

$$\varepsilon A_{\text{fr}}\rho_{\text{g}}c_{p,\text{g}}\frac{\partial T_{\text{g}}}{\partial t}=\varepsilon A_{\text{fr}}k_{\text{eff}}\frac{\partial^2 T_{\text{g}}}{\partial z^2}-\varepsilon A_{\text{fr}}\rho_{\text{g}}c_{p,\text{g}}u_{\text{i}}\frac{\partial T_{\text{g}}}{\partial z}+A_{\text{fr}}\left(\frac{A_{\text{s}}}{V_{\text{bed}}}\right)h_{\text{g-s}}\left(T_{\text{s}}-T_{\text{g}}\right)+\pi d_{\text{can,in}}h_{\text{g-can}}\left(T_{\text{can}}-T_{\text{g}}\right) \qquad 2.4$$

where $h_{\text{g-s}}$ is the convection coefficient between the gas and adsorbent, $h_{\text{g-can}}$ is the convection coefficient between the gas and canister wall. The effective axial thermal conductivity, k_{eff}, accounts for both the adsorbent- and gas-phase conductivities as well as axial thermal dispersion due to mixing. These coefficients are calculated using empirical correlations as described in the Section 2.2.4 below.

The adsorbent-phase energy balance accounts for transient storage, convective heat loss to the gas, and the heat of adsorption, but neglects axial conduction as the gas-phase energy balance already accounts for the adsorbent-bed conductivity,

$$A_{\text{fr}}\left(1-\varepsilon\right)\rho_{\text{env}}c_{p,\text{s}}\frac{\partial T_{\text{s}}}{\partial t}=A_{\text{fr}}\frac{A_{\text{s}}}{V_{\text{bed}}}h_{\text{g-s}}\left(T_{\text{g}}-T_{\text{s}}\right)-\left(1-\varepsilon\right)A_{\text{s}}\lambda\frac{\partial q}{\partial t}, \qquad 2.5$$

where A_{s} is the pellet external surface area. The isosteric heat of adsorption, λ, is derived from the Clausius-Clapeyron relationship as will be described further in Section 2.2.4.

The canister wall energy balance includes transient energy storage, axial conduction, and heat transfer with the internal gas-phase and the external insulation,

$$A_{\text{can}}\rho_{\text{can}}c_{p,\text{can}}\frac{\partial T_{\text{can}}}{\partial t}-A_{\text{can}}k_{\text{ can}}\frac{\partial^2 T_{\text{can}}}{\partial z^2}=\pi d_{\text{can,in}}h_{\text{g-can}}\left(T_{\text{g}}-T_{\text{can}}\right)+\pi d_{\text{can,out}}h_{\text{can-ins}}\left(T_{\text{ins}}-T_{\text{can}}\right), \qquad 2.6$$

where A_{can} is the cross-sectional area of the canister wall and $h_{\text{can–ins}}$ is the heat transfer coefficient between the canister and the insulation. A heat transfer coefficient of $h_{\text{can–ins}}$ = 3 W/(m^2 K) is assumed for both test stands having insulation loosely affixed to the canister wall.

The insulation energy balance accounts for transient energy storage, axial conduction, and heat transfer with the canister and ambient air,

$$A_{\text{ins}}\rho_{\text{ins}}c_{p,\text{ins}}\frac{\partial T_{\text{ins}}}{\partial t}-A_{\text{ins}}k_{\text{ ins}}\frac{\partial^2 T_{\text{ins}}}{\partial z^2}=\pi d_{\text{ins,in}}h_{\text{can-ins}}\left(T_{\text{can}}-T_{\text{ins}}\right)+\pi d_{\text{ins,out}}h_{\text{ins-amb}}\left(T_{\text{amb}}-T_{\text{ins}}\right), \qquad 2.7$$

where A_{ins} is the cross-sectional area of the insulation, and the heat transfer coefficient between the insulation and the ambient is assumed to have a value of $h_{\text{ins–amb}}$ = 3 W/(m^2 K).

2.2.4 Model inputs

The model described in Sections 2.2.1 to 2.2.3 above calls for several input parameters to predict the temperatures and concentrations within the sorbent bed. Table 2.1 provides the geometric dimensions and material properties of the adsorbent, canister, and insulation of the two test stands. The properties of the CO_2 and N_2 gas mixture are computed assuming that they are ideal gases and accounting for local temperature, pressure, and composition [87]. Table 2.2 summarizes the inlet and initial conditions measured during the breakthrough experiments [15], [80]. These conditions, representative of the conditions in the CDRA during adsorption, are used for all simulations in this chapter. The remaining model input parameters are either predicted from empirical correlations or

directly fit to experimental data. These inputs can generally be categorized as heat transfer coefficients, bed transport properties, or equilibrium isotherm parameters.

Table 2.2. Inlet and initial conditions for breakthrough of CO_2 on zeolite in test stands A [15] and B [80].

operational parameter	**Test stand A**	**Test stand B**
volumetric flow rate, V, SLPM	28.3	132
inlet temperature, $T_{g,in}$, K	298	299
initial temperature, T_{init}, K	299	299
ambient temperature, T_{amb}, K	298	297
inlet total pressure, $p_{g,in}$, kPa	106	126
inlet CO_2 partial pressure, $p_{CO2,in}$, kPa	0.816	0.689

The empirical correlations used to predict the heat transfer coefficients and bed transport properties are expressed in terms of the dimensionless Prandtl, Schmidt, and Peclet numbers defined in the *Nomenclature* section. A dimensionless pellet Reynolds number is also used in these correlations, defined using the superficial fluid velocity and the pellet diameter as the length scale,

$$Re_p = \frac{u_\infty d_p \rho_g}{\mu_g} \quad . \tag{2.8}$$

The interfacial gas-adsorbent heat transfer coefficient, $h_{g\text{-}s}$, is predicted from the empirical correlation of Wakao *et al.*[88],

$$Nu_{g\text{-}s} = \frac{h_{g\text{-}s} d_p}{k_g} = 2 + 1.1 Pr_g^{1/3} Re_p^{0.6} \quad . \tag{2.9}$$

The heat transfer coefficient between the gas and inner canister wall, $h_{g\text{-}can}$, is predicted using the empirical correlation from Li and Finlayson [89] as

$$Nu_{g\text{-}can} = \frac{h_{g\text{-}can} d_{can,in}}{k_g} = 2.03 Re_p^{0.8} e^{\left(-6 d_p / d_{can,in}\right)} \quad . \tag{2.10}$$

The effective axial thermal conductivity is calculated from the correlation of Yagi *et al.*[90] as

$$k_{eff,ax} = k_g \left(\frac{k_{eff}^0}{k_g} + 0.75 Pr Re_p \right) \tag{2.11}$$

where the effective axial thermal conductivity of a quiescent bed of spherical particles is given by the Krupiczka [91] equation,

$$k_{\text{eff}}^{0} = k_{\text{g}}\left(\frac{k_{\text{s}}}{k_{\text{g}}}\right)^{n} \quad \text{where} \quad n = 0.280 - 0.757\log_{10}\left(\frac{k_{\text{s}}}{k_{\text{g}}}\right). \tag{2.12}$$

The axial dispersion is predicted following the method described by Langer *et al.*[92] This method expresses the axial dispersion coefficient for the j^{th} species, $D_{\text{ax},j}$, in dimensionless form as

$$\frac{1}{Pe_j} = \frac{D_{\text{ax},j}}{d_{\text{p}}u_{\text{i}}} = \frac{\tau\varepsilon}{Re_{\text{p}}Sc_j} + \frac{Pe_{\infty}^{-1}}{1+\dfrac{\beta\tau\varepsilon}{Re_{\text{p}}Sc_j}} \tag{2.13}$$

where τ and β are empirically fit constants respectively termed the tortuosity and radial dispersion factor, Pe_{∞} is the Peclet number at infinite velocity, and Sc_j is the Schmidt number for the j^{th} species,

$$Sc_j = \frac{\mu_{\text{g}}}{\rho_{\text{g}}D_{\text{M},j}}. \tag{2.14}$$

We find the molecular diffusivity of component j in the mixture using the relation given by Fairbanks and Wilke [93],

$$D_{\text{M},j} = \frac{1-y_j}{\sum_{k\neq j} y_k / D_{jk}}, \tag{2.15}$$

where D_{jk} is the binary diffusion coefficient of species j in species k calculated from the kinetic theory of gases [94]. The coefficients τ and β in Eq. 2.13 were empirically determined by Edwards and Richardson [86] for flow through a uniformly packed bed of nonporous spherical particles to be 0.73 and 13, respectively. This correlation approximates only the pellet-driven dispersion and is valid for flow where $0.008 < Re_{\text{p}} < 50$ and $0.377 \text{ mm} < d_{\text{p}} < 6 \text{ mm}$. Theoretically, at infinite velocity, $Pe_{\infty} = 2$; however, experimental observations show that Pe_{∞} a strong function of pellet diameter [92]:

$$Pe_{\infty} = \begin{cases} 6.7\times\left(d_{\text{p}}/[cm]\right) & d_{\text{p}} \le 0.3 \text{ cm} \\ 2.0 & 0.3 \text{ cm} < d_{\text{p}} \end{cases}. \tag{2.16}$$

We use this empirically observed expression for Pe_{∞} when calculating D_{ax} in Eq. 2.13.

The equilibrium adsorbed-phase concentration is calculated using the Toth equilibrium adsorption isotherm [95] as

$$n^* = \frac{ap}{\left[1+(bp)^t\right]^{1/t}}; \quad b = b_0 \exp(E/T) \qquad 2.17$$
$$a = a_0 \exp(E/T) \qquad t = t_0 + c/T$$

where a is the saturation capacity, b is an equilibrium constant, E is the activation energy or energy of adsorption, and t is the heterogeneity parameter. Parameters a, b, and t are temperature-dependent as shown, whereas a_0, b_0, and t_0 are system-dependent, adsorption-isotherm parameters [57] given in Table 2.3. The isosteric heat of adsorption, λ, is derived from the Clausius-Clapeyron relationship for the Toth isotherm as

$$\lambda = \frac{a\rho_{env} p_{CO_2}}{\left(1+\left(b \cdot p_{CO_2}\right)^t\right)^{1/t}} \qquad 2.18$$

where p_{CO_2} is the partial pressure of CO_2 and a, b, and t are the temperature-dependent parameters from the Toth isotherm shown in Eq. 2.17.

Table 2.3. Toth equilibrium adsorption isotherm parameters for CO_2 on zeolite 5A [57].

a_0, mol/(kg kPa)	b_0, kPa^{-1}	E, K	f_0	c, K
9.875×10^{-7}	6.761×10^{-8}	5625	0.27	-20.02

2.3 Uncertainty bounds of model input parameters

We compare the available empirical correlations with published experimental data to estimate the uncertainty in the heat transfer coefficients, axial dispersion, and effective axial thermal conductivity. Experimental data for the gas-adsorbent Nusselt number, $Nu_{g\text{-}s}$, as a function of $Pr^{1/3}Re_p^{0.6}$ taken from Wakao and Kagei [96] (and originally published in Refs. [97]–[107]) are reproduced in Figure 2.2 along with the empirical correlation by Wakao *et al.* [88] (solid line). The coefficient of the $Pr^{1/3}Re_p^{0.6}$ term in the Wakao *et al.* [88] correlation was varied to obtain upper and lower uncertainty bounds (dashed lines) encompassing 95% of all the experimental data. Similarly, for the gas-wall Nusselt number, the coefficient of the $Re_p^{0.79}$ term in the Li and Finlayson [89] correlation was varied to obtain upper and lower uncertainty bounds (dashed lines) encompassing 95% of all the experimental data as shown in Figure 2.3. The experimental data in Figure 2.3 were taken from Li and Finlayson's [89] review of the literature and were originally published in Refs. [108] and [109].

A similar approach was taken to find upper and lower uncertainty bounds for the axial dispersion term. Delgado [46], [47] compiled experimental measurements of axial dispersion from several authors [86], [110]–[116]. These data were compared with the Langer *et al.* [92] correlation shown in Eq. 2.13. The empirical fits of Scott *et al.* [117] ($\tau = 0.57$, $\beta = 42$) and Wicke [118] ($\tau = 1$, $\beta = 0$) provide the widest range of predicted values for D_{ax}, encompassing 92% of the experimental data shown in Figure 2.4. We take these two correlations to be the upper and lower bounds on D_{ax}.

Özgümüş *et al.* [119] reviewed experimental studies measuring effective axial thermal conductivity for granular packed beds with a variety of bed materials and Reynolds numbers ranging from 0.001 to 3000. We compiled data from those studies [90], [120]–[124] which used spherical particles in a flowing gas (as opposed to water or other liquids). These data included a wide range of particle materials ranging from low thermal conductivity glass, $k_s = 0.1$ W/(m K), to high thermal conductivity nickel, $k_s = 90$ W/(m K). To account for the different particle and fluid properties, the quiescent-bed effective axial thermal conductivity, k_{eff}^0, was calculated for each experiment using the Krupiczka [91] equation (Eq. 2.12). We then subtract k_{eff}^0 from the reported k_{eff} and divided by the gas thermal conductivity, k_g, to obtain the normalized effective axial thermal conductivity, $k_{eff}/k_g - k_{eff}^0/k_g$. The normalized effective axial thermal conductivity is plotted against the product of Prandtl and Reynolds numbers, $PrRe_p$, along with the empirical correlation by Yagi *et al.* [90] (solid line) in Figure 2.5. The coefficient of the $PrRe_p$ term in the Yagi *et al.* [90] correlation was then varied to obtain upper and lower uncertainty bounds (dashed lines) encompassing 95% of all the experimental data.

The uncertainty in void fraction and pellet density comes directly from the uncertainty of measured values for test stand B as described by Son *et al.* [80]. The insulation-ambient heat transfer coefficient uncertainty comes from the typical full range of free-convection heat transfer coefficients given by Incropera *et al.* [125]. In the absence of a similar range of possible values for the canister-insulation heat transfer coefficient, we consider the two most extreme cases, an adiabatic interface ($h_{can\text{-}ins} \to 0$) and an isothermal interface ($h_{can\text{-}ins} \to \infty$). Knox *et al.* [11], [15] found that the uncertainty in LDF due to uncertainty in *ad hoc* prediction of axial dispersion when fitting to experimental data (following the method used in the present work) is approximately ±5%.

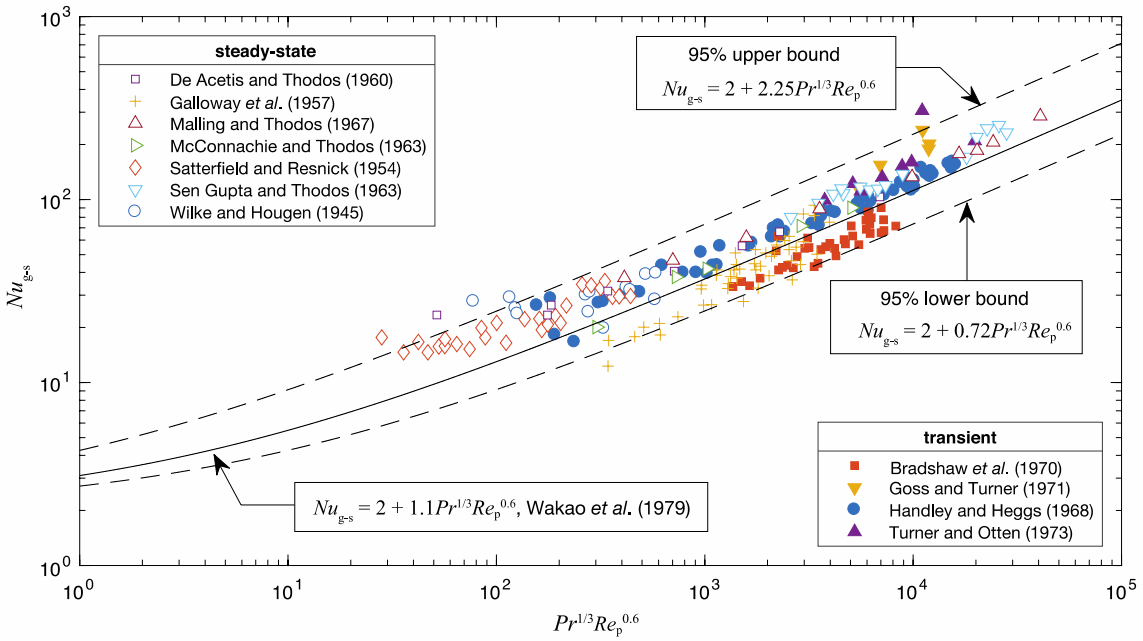

Figure 2.2. Experimental measurements [97]–[107]of interfacial gas-sorbent Nusselt number compared with the correlation of Wakao *et al.* [88] (solid line) and uncertainty bounds (dashed lines) encompassing 95% of data.

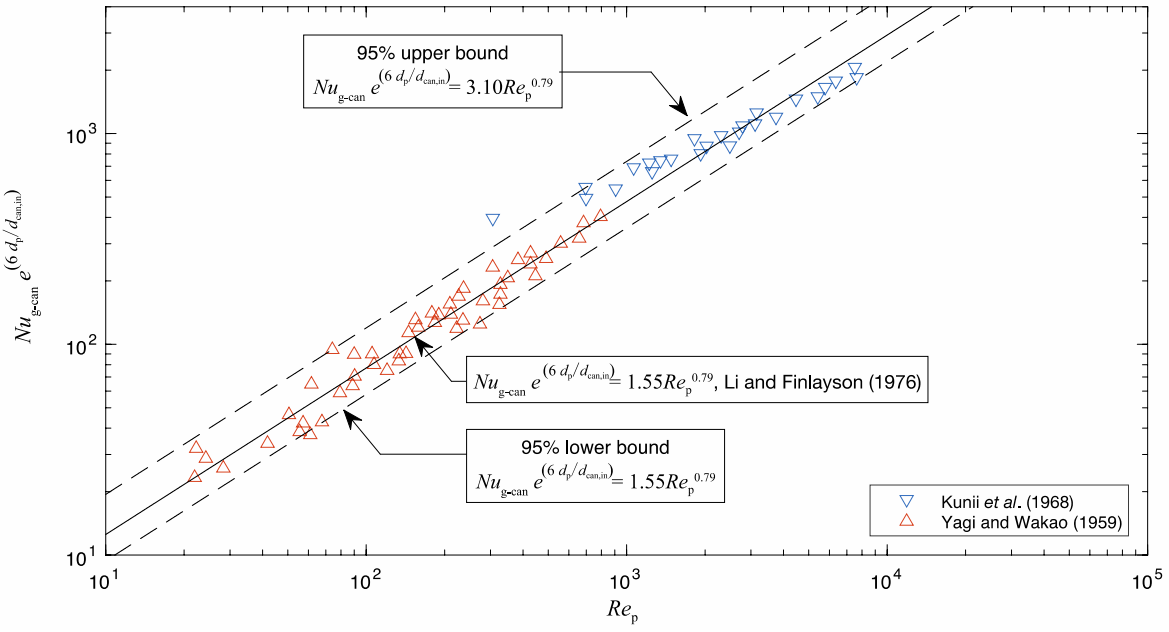

Figure 2.3. Experimental measurements [109],[108] of gas-canister Nusselt number compared with the correlation of Li and Finlayson [89] (solid line) and uncertainty bounds (dashed lines) encompassing 95% of data.

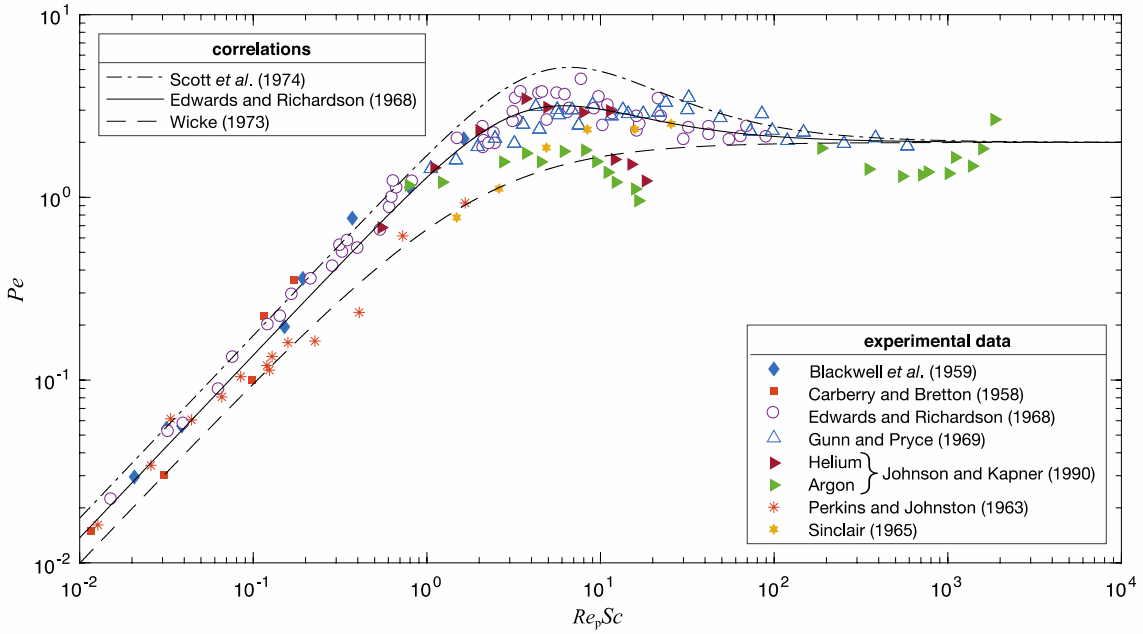

Figure 2.4. Experimental measurements [86], [110]–[116] of axial dispersion of gases through fixed beds of spherical particles compared with the correlation of Edwards and Richardson [86] (solid line). Upper and lower uncertainty bounds on D_{ax} are estimated from the correlations of Scott *et al.* [117] and Wicke [118], respectively.

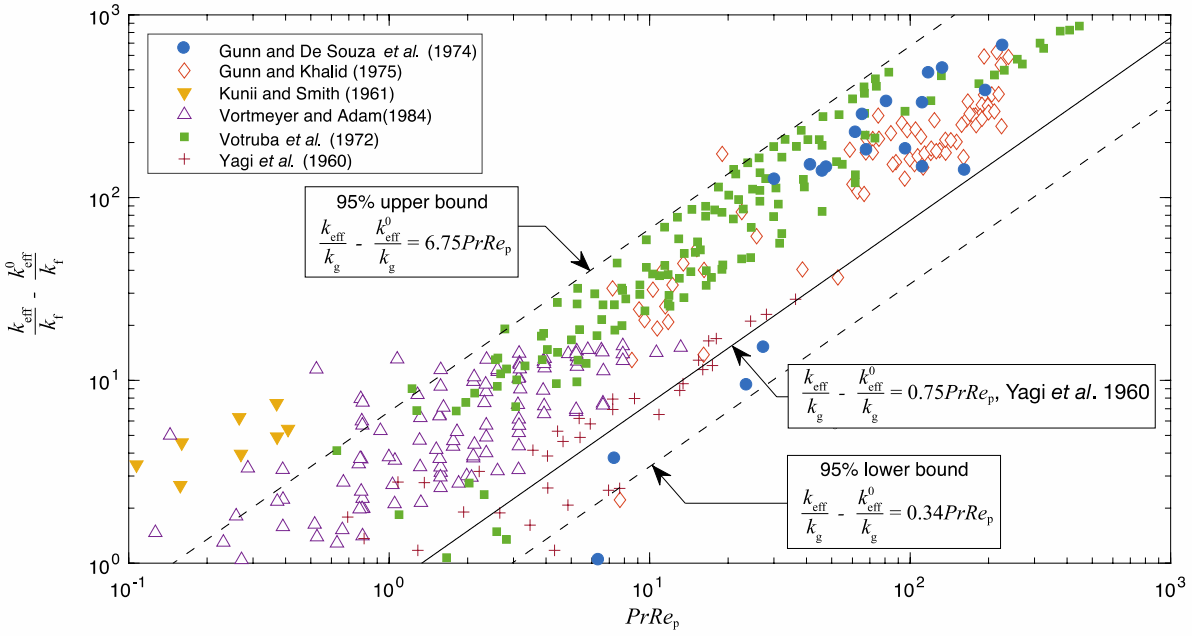

Figure 2.5. Experimental measurements [86], [110]–[116] of the effective axial thermal conductivity of a fixed bed of spherical particles with gas flow compared with the correlation of Yagi *et al.* [90] (solid line) and uncertainty bounds (dashed lines) encompassing 95% of data.

It is noted that we do not consider uncertainty in isotherm parameters, for which the adsorption model sensitivities have been extensively characterized and are well-known [17]–[20], [27], [33]–[36], [39], [42]–[44]. Thermophysical properties for the canister wall, insulation, and gas mixtures are well known and not considered in this uncertainty analysis. The model uncertainty due to other inputs, such as the geometric dimensions of the bed and inlet conditions, is also not studied because these quantities can be trivially and accurately measured.

2.4 Solution procedure

The governing equations as given by Eqs. 2.1–2.7 are coupled and solved in COMSOL Multiphysics [126]. A one-dimensional mesh is generated with a uniform element size of 1% of the total bed length. The PARDISO algorithm—a direct method based on LU decomposition—is used to solve linear equations and the Newton automatic highly nonlinear method to solve nonlinear equations. The solver uses the backward differentiation formula to dynamically modify the time step and improve computation time; we impose an initial time step of 1×10^{-8} s and a maximum time step of 120 s to improve stability. Convergence is reached when the relative residuals drop below 10^{-4} for all dependent variables, namely CO_2 concentration in the gas phase and adsorbed phase, pressure, and temperatures of the adsorbent, gas, canister, and insulation.

2.5 Results

The model is first calibrated using experimental data to determine the LDF coefficient, k_l, and the axial dispersion coefficient, D_{ax}. Then, an uncertainty analysis is performed by varying each model input between its upper and lower uncertainty bounds, as defined in Section 2.2.4 above, and observing the relative change in important output quantities.

2.5.1 Model calibration

Determining the axial dispersion coefficient from experiments using mixed, downstream concentration measurements is inaccurate for a small-diameter bed where wall channeling effects dominate the axial mixing behavior. Available empirical correlations for axial dispersion do not capture the influence of channeling in the near-wall region, as they are designed to predict pellet-driven axial dispersion [46]. Knox *et al.* [15] described a method to more accurately obtain the

LDF coefficient from small-diameter reactors by using centerline measurements of concentration immediately before the exit of the bed. We follow this procedure in the current work to independently extract the LDF and axial dispersion coefficients from the experimental measurements of test stand A. The procedure assumes that dispersion in the center of the bed (far from the canister wall) is pellet-driven, and thus the axial dispersion at the centerline of a bed can be accurately predicted by empirical correlations. Using this prediction of axial dispersion from correlations as an input, the model can then be fit to the centerline measurement of concentration by varying the value of the LDF coefficient; the value that provides the best fit is taken as the LDF coefficient extracted from this calibration process.

To extract the LDF coefficient from test stand A, we simulate breakthrough for LDF coefficients varying from 1.75×10^{-3} s^{-1} to 2.4×10^{-3} s^{-1} at increments of 5×10^{-5} s^{-1}, while using the Edward and Richardson correlation [86] to predict axial dispersion at the inlet conditions ($D_{ax} = 1.13\times10^{-3}$ m^2/s). The temporal, gas-phase-CO_2 concentration is then compared with experimental data at 97.5% of the bed length (z = 247.5 mm). Figure 2.6a shows the time dependence of the concentration of CO_2 at the bed exit breakthrough from the best-fit simulation (black line) alongside experimental measurements of the centerline concentration (red diamonds) for test stand A. This plot is commonly referred to as the breakthrough curve. The gray region in Figure 2.6a marks the span of the simulated breakthrough curves for LDF coefficient. Initially (at t = 0) the adsorbent is devoid of CO_2, and when the N_2-CO_2 gas mixture first enters the bed, it adheres to the first few layers of adsorbent, filling up the most easily accessed surface area with monolayers of CO_2. As time progresses, the adsorbent near the bed entrance becomes saturated, and the CO_2 penetrates farther into the bed; however, the CO_2 does not reach the bed exit until most of the bed becomes saturated. The breakthrough point as defined herein occurs when the CO_2 concentration in the effluent reaches 1% of the influent concentration (c/c_0 = 1%); this occurs at t = 0.45 h in Figure 2.6a.

Due to the finite rate of adsorption, a diffuse concentration front forms as the CO_2 progresses through the bed. This diffuse front is evident from the S-shaped portion of the breakthrough curve which shows a sharp initial rise in concentration near the breakthrough time and a gradual tapering off as the effluent approaches the influent concentration. The difference in curvature at these two locations is explained by the concentration dependence of the rate of adsorption. The rate of

adsorption is linearly proportional to the difference between the current and equilibrium concentrations of the adsorbed phase. Thus, the curvature of the effluent concentration is more gradual at the end of the test, when the bed is nearly saturated, compared with the sharp curvature seen in the initial concentration rise at breakthrough.

To evaluate the sum of squared errors (SSE) between the model prediction and the sparse experimental data, a cubic spline is used to interpolate values of experimental concentration (see red line in Figure 2.6a). Note that the saturation term of the Toth isotherm was increased by 16% to shift the model predictions along the time axis to be in closest agreement with the experimental data at the midpoint of the breakthrough curve. This is necessary because the isotherm parameters used in the model were not developed for the specific zeolite 5A formulation used in this study; furthermore, this capacity change has no influence on the slope of the curve and is thus inconsequential to the resulting best-fit k_l value. Only data in the middle 50% of the concentration range are used to compute the SSE as indicated by the dashed blue horizontal lines in Figure 2.6a. This is done to fit the LDF to the linear portion of the breakthrough curve. Figure 2.6b shows the SSE as a function of the LDF coefficient. The minimum SSE corresponds to $k_l = 2.1\times10^{-3}$ s^{-1}.

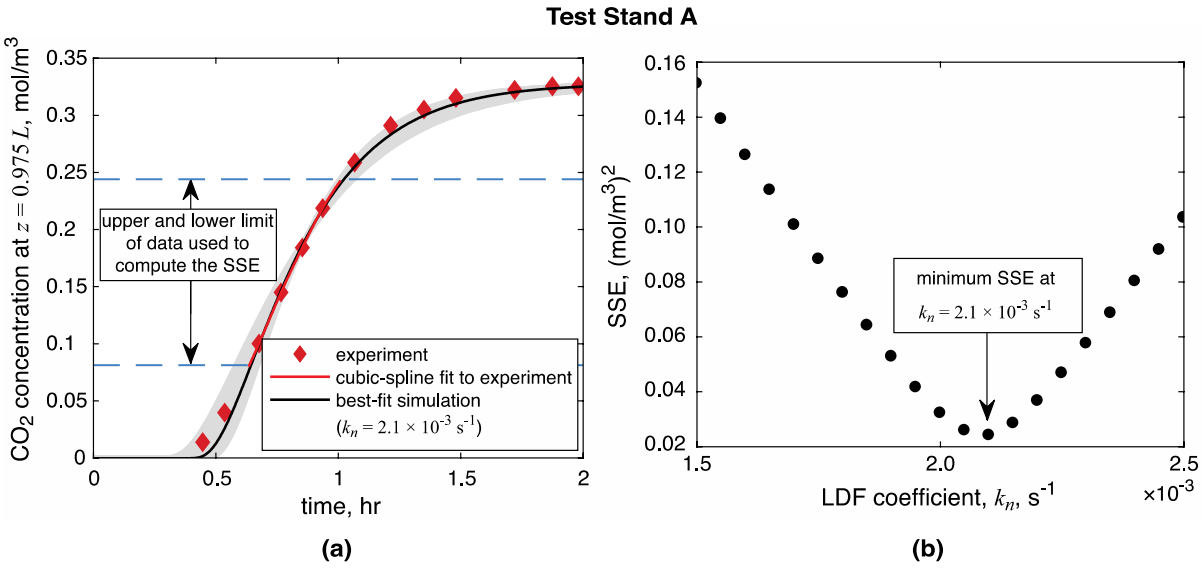

Figure 2.6. Calibration of LDF in test stand A: (a) model predictions shown alongside experimental measurements of exit concentration at 97.5% of the bed length for CO_2 breakthrough, and (b) SSE between the model prediction and cubic-spline fit to the experimental data as a function of LDF coefficient. The gray region in (a) marks the span of the simulated breakthrough curves for the range of LDF coefficients in (b). ($D_{ax} = 1.13\times10^{-3}$ m^2/s).

Using this LDF value, the effective axial dispersion of the entire bed (accounting for both the effects of pellet-driven dispersion and wall channeling) is determined by fitting the model predictions to the concentration of the mixed effluent, measured far downstream of the bed. Breakthrough is simulated for axial dispersion coefficients varying from 1×10^{-4} m^2/s to 1 m^2/s in logarithmic steps (forty steps per decade). Figure 2.7a shows the breakthrough curve from the best-fit simulation (black line) alongside experimental measurements of the mixed downstream concentration (red diamonds) in test stand A, and Figure 2.7b shows the SSE as a function of axial dispersion coefficient. Again, for comparing the simulated concentration with experimental data, a cubic spline is used to interpolate values at the simulated time steps, and only data in the middle 50% of the concentration range (indicated by the dashed blue horizontal lines in Figure 2.7a) are used to compute the SSE. The minimum SSE corresponds to an axial dispersion coefficient of D_{ax} = 1.2×10^{-2} m^2/s which is one order of magnitude larger than the axial dispersion coefficient predicted from the Edwards and Richardson [86] correlation, D_{ax} = 1.13×10^{-3} m^2/s. We attribute this significant difference to wall channeling effects that dwarf axial dispersion in beds with small bed-to-pellet diameter ratios. Our findings are consistent with those of Knox *et al.* [15], who also calibrated a one-dimensional adsorption model to experimental data from the same test stand. We attribute slight differences from their calibrated LDF and axial dispersion coefficients, 2.3×10^{-3} s^{-1} and 1.3×10^{-2} m^2/s respectively, to differences between our modeling approaches. Namely, the present model uses the Clausius-Clapeyron equation to determine the temperature-dependent isosteric heat of adsorption and separately models the canister wall and insulation, whereas Ref. [15] uses a constant heat of adsorption and combines the insulation and canister-wall energy equations. Additionally, we account for the effect of pellet diameter on Pe_∞[53], a term in the Edwards and Richardson [86] correlation, while Ref. [15] assumes that $Pe_\infty = 2$.

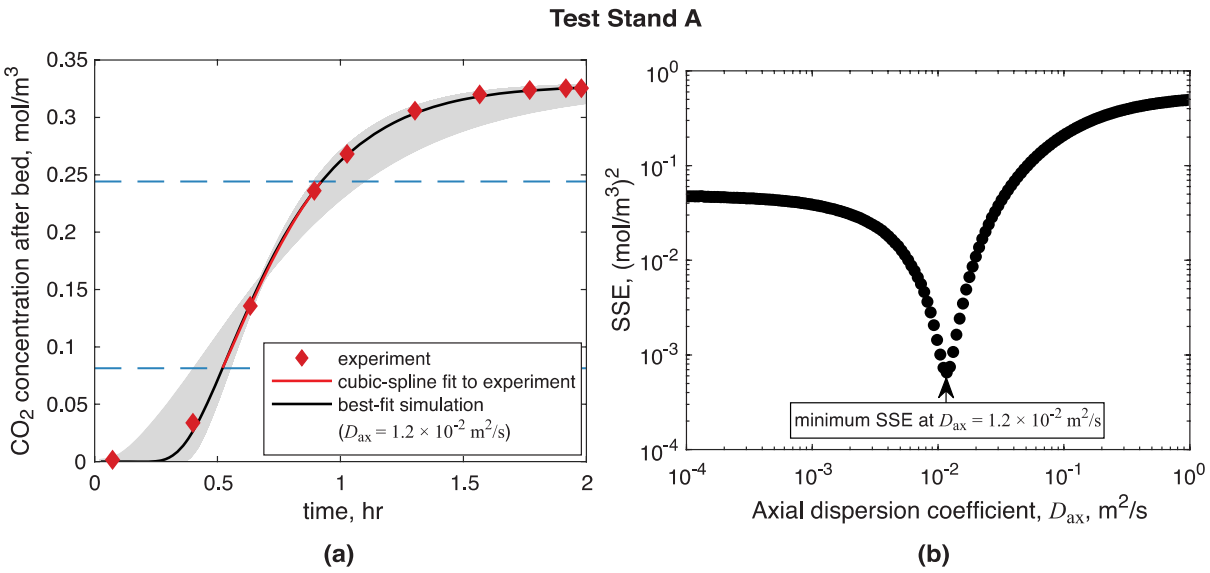

Figure 2.7. Calibration of D_{ax} in test stand A: (a) model predictions shown alongside experimental measurements of mixed concentration far downstream of the bed for CO_2 breakthrough, and (b) the SSE between the model prediction and cubic-spline fit to the experimental data as a function of D_{ax}. The gray region in (a) marks the span of the simulated breakthrough curves for the D_{ax} values simulated in (b). (k_l = 2.1×10^{-3} s^{-1}).

Unlike test stand A, test stand B is not instrumented to measure the centerline CO_2 concentration. As such, the same procedure cannot be followed to obtain the LDF coefficient independently. Experiments on both test stand A and B were conducted using clay bound zeolite 5A pellets of similar diameter. Considering that the mass transfer coefficient is in theory only a function of the sorbent-adsorbate pair, the LDF coefficient obtained from stand A (k_l = 2.1×10^{-3} s^{-1}) is used to determine D_{ax} for test stand B. Using this LDF coefficient, breakthrough simulations were run for test stand B while varying the axial dispersion from 1×10^{-7} m^2/s to 1 m^2/s in logarithmic steps (twenty steps per decade). The simulated concentration for each of these D_{ax} is compared with experimental data for the mixed concentration downstream of the bed. Figure 2.8a shows the breakthrough curve from the best-fit simulation (black line) and experimental measurements (red line) in test stand B, and Figure 2.8b shows the SSE as a function of axial dispersion coefficient, respectively. Concentration measurements in test stand B are taken at a sufficiently high temporal frequency to allow direct comparison with the simulation results when computing the SSE. Again, only data in the middle 50% of the concentration range are used for this calculation (indicated by the dashed blue horizontal lines in Figure 2.8a). The resulting plot of SSE over the range of axial dispersion values evaluated shows no clear minimum SSE in Figure 2.8b. Rather, the error

asymptotically approaches a constant minimum value as the axial dispersion coefficient tends toward zero, with the best fit to the experimental results being the lowest simulated value, D_{ax} = 1×10^{-7} m^2/s. This result indicates that axial mixing in test stand B is not dominated by channeling effects and the experiment is well represented by a plug-flow model. Furthermore, as the error remains relatively constant for all values of $D_{ax} \leq 2\times10^{-3}$ m^2/s, we can use the Edwards and Richardson [86] correlation for pellet-driven axial dispersion with good accuracy for test stand B. These calibrated k_l and D_{ax} are taken as the baseline model inputs for the analysis.

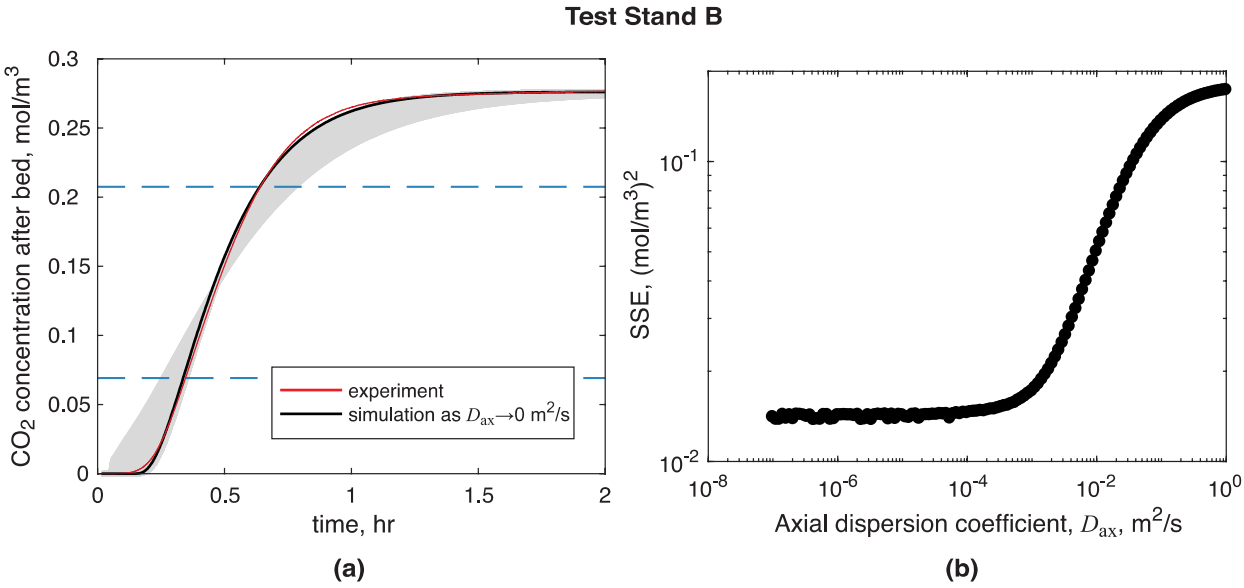

Figure 2.8. Calibration of D_{ax} in test stand B: (a) model predictions shown alongside experimental measurements of mixed concentration far downstream of the bed for CO_2 breakthrough, and (b) the SSE between the model prediction and the experimental data as a function of D_{ax}. The gray region in (a) marks the span of the simulated breakthrough curves for the D_{ax} values simulated in (b). (k_l = 2.1×10^{-3} s^{-1}).

2.5.2 Comparison to baseline

Using the calibrated LDF and the axial dispersion coefficients, we assess the model predictions for a case with all input parameters fixed at a set of baseline values. These model input parameters and their baseline values are given in Table 2.4 for test stands A and B. The parameters are subdivided into three categories: bed parameters, heat transfer coefficients, and adsorbent properties. The model predictions are assessed in terms of five different output performance metrics:

1. breakthrough time, t_b – the time when the concentration of adsorbate at the bed exit, c, first reaches 1% of the inlet concentration (*i.e.*, $c/c_0 \geq 0.01$);
2. stoichiometric breakthrough time, $\bar{t}_{stoich}$ – the time it would take to completely saturate the bed if there were no mass transport resistance, found via integration,

$$t_{stoich} = \int_0^\infty \left(1 - \frac{c(t)}{c_0}\right) dt \ ; \qquad 2.19$$

3. total capacity, χ – the mass of CO_2 adsorbed by the zeolite 5A bed after the bed is saturated (*i.e.*, $c/c_0 \geq 0.99$);
4. time to reach maximum outlet temperature, $t(T_{g,max})$ – the time when the bed exit gas temperature reaches its maximum value;
5. maximum temperature rise, $\Delta T_{g,max}$ – the maximum temperature difference of the gas across the bed (*i.e.*, $T_g(z = L) - T_g(z = 0)$); and
6. mean temperature rise, $\Delta T_{g,mean}$ – the time-averaged temperature difference of the gas across the bed.

The model is run with the input values as given in Table 2.4 to obtain baseline output parameters for both test stands. These results are tabulated in Table 2.5. Figure 2.9 shows the breakthrough curve from the baseline simulation (dashed line) alongside experimental measurements of the mixed downstream concentration for test stands A and B (panels a and b, respectively). The simulation breakthrough curve matches the experimental data very well. Test stand A takes approximately twice as long to break through (see solid green lines in Figure 2.9a and b). Given that both beds are subject to similar superficial velocities and bed void fractions (see Table 2.2), we attribute this difference in breakthrough time to the difference in bed length. For similar reasons, the stoichiometric breakthrough time of test stand A is greater than of test stand B (see dotted green lines in Figure 2.9a and b). The bed in test stand B is larger and thus holds more pellets and has a greater total capacity for holding CO_2. Normalizing the capacities of the two beds by the mass of adsorbent in each, we find that both beds hold approximately 5% CO_2 by mass at equilibrium. Figure 2.9 also shows the effluent temperature from the baseline simulation (dashed line) alongside experimental measurements of the mixed downstream concentration for test stand A and test stand B (panels c and d, respectively). The initial spike in the experimentally measured temperature of test stand A is attributed to N_2 adsorption. Recall that test stand A is kept in a helium environment prior to starting the breakthrough experiment. The introduction of nitrogen to

the adsorption bed results in a slight rise in temperature as a minute quantity is adsorbed onto the zeolites; this phenomenon is not captured in our simulation results, which treat nitrogen as inert. Apart from this discrepancy in test stand A, the simulation predictions closely follow the initial temperature rise and match the maximum temperature to within one degree. The outlet temperature peaks sooner in test stand B than A, again due to the difference in bed length. Notably, the outlet temperature peaks in test stand B simultaneously with breakthrough. We attribute this to the very low axial dispersion in test stand B which closely mimics ideal plug-flow behavior. This close match also indicates that the temperature gradient in the radial direction of the bed is small and thus the overall temperature gradient, which is primarily axial, is well represented by the one-dimensional model.

Table 2.4. Baseline values of the model input parameters varied in the sensitivity analysis.

model input parameter	**test stand A**	**test stand B**
linear-driving-force coefficient, k_l, s^{-1}	2.1×10^{-3}	2.1×10^{-3}
axial dispersion, D_{ax}, m^2/s	1.20×10^{-2}	1.13×10^{-3}
effective axial thermal conductivity, $k_{eff,ax}$, W/(m K)	0.673	0.726
void fraction, ε	0.35	0.35
gas-sorbent heat transfer coefficient, $h_{g\text{-}s}$, $W/(m^2K)$	128	148
gas-canister heat transfer coefficient, $h_{g\text{-}can}$, $W/(m^2K)$	16.9	10.8
canister-insulation heat transfer coefficient, $h_{can\text{-}ins}$, $W/(m^2K)$	3	3
insulation-ambient heat transfer coefficient, $h_{ins\text{-}amb}$, $W/(m^2K)$	3	3
sorbent envelope density, ρ_{env}, kg/m^3	1180	1179
sorbent thermal conductivity, k_s, W/(m K)	0.152	0.144
sorbent specific heat, $c_{p,s}$, J/(kg K)	920	650

Table 2.5. Output metrics for the baseline simulation and experimental results.

	test stand A		**test stand B**	
output metrics	**simulation**	**experiment**	**simulation**	**experiment**
breakthrough time, t_b, s	1000	N/A*	630	580
stoichiometric breakthrough time, t_{stoich}, s	2640	2676	1848	1876
total capacity, χ, g	17.1	18.9	43.3	45.3
time to max outlet temperature, $t(T_{g,max})$, s	1300	1497	510	650
max temperature rise, $\Delta T_{g,max}$, K	11.0	11.7	7.3	7.1
mean temperature rise, $\Delta T_{g,mean}$, K	3.6	4.8	1.8	2.0

* experimental data are not sufficiently resolved to determine the exact breakthrough time in test stand A

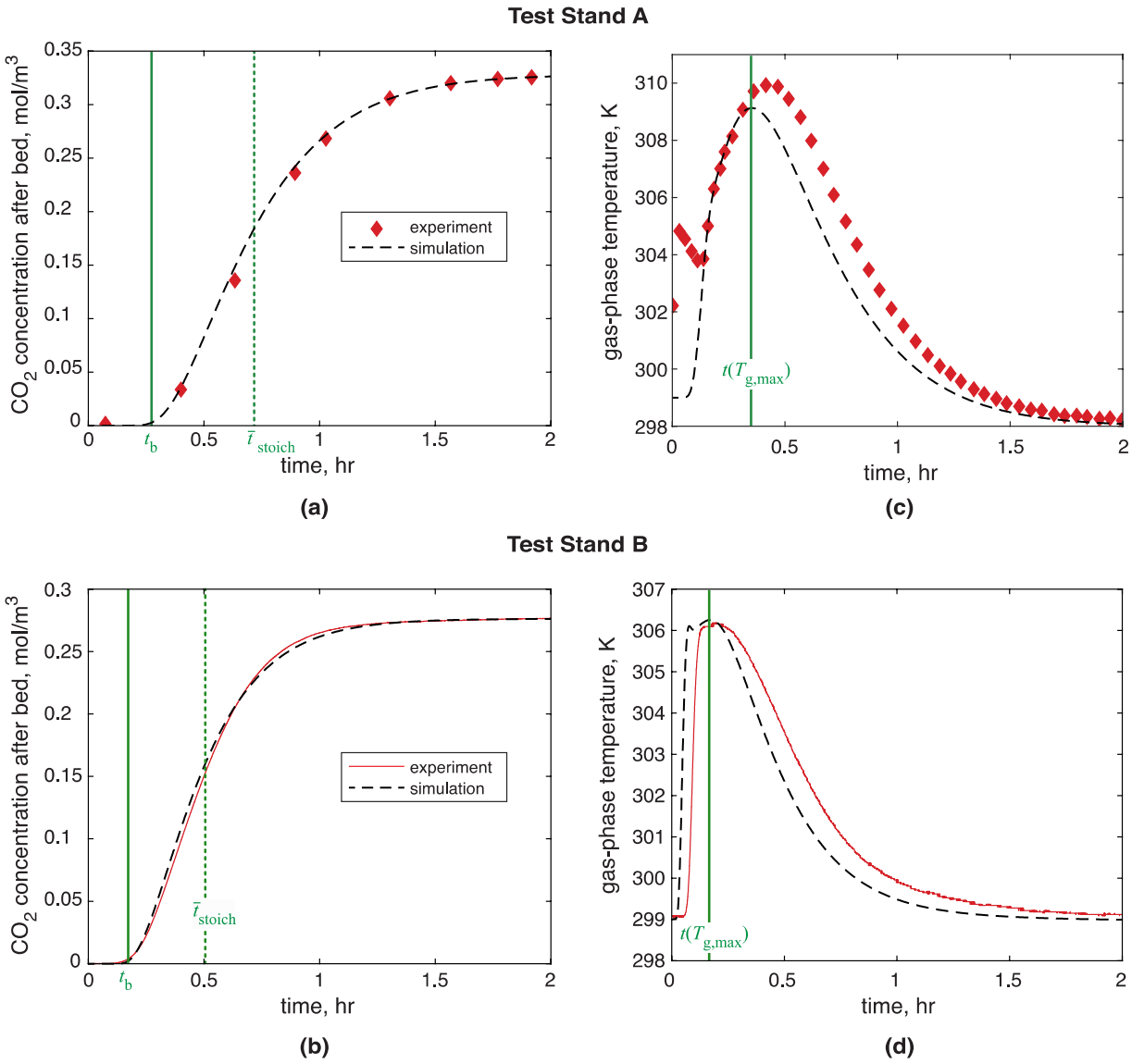

Figure 2.9. Comparison of baseline simulation and experimental data for test stand A (top) and test stand B (bottom). Left panels (a, b) show breakthrough curves and right panels (c, d) show exit temperature. All values are for mixed, downstream measurements.

2.5.3 Uncertainty analysis

We next perform an analysis of model uncertainty given the expected potential deviations from these baseline parameters as described in Section 2.2.4. The percent change versus the baseline case is evaluated using the six performance metrics (defined in Section2.5.2) for upper and lower bounding values of each model input parameter. These bounds are summarized in Table 2.7. Given the excellent agreement between the baseline model and experiments, we consider this analysis as an approximation of uncertainty in the model predictions. The adsorbent conductivity and specific heat are excluded from this table because uncertainty values were not provided by the manufacturers, and also based on the results from a sensitivity analysis which showed that, at ±10% uncertainty, these parameters would have a negligible effect on the simulated performance [77].

Simulations were performed for all high and low bounding values included in Table 2.7. The percent changes in the performance metrics were then compared to the baseline case. Table 2.8 reports these relative percent changes in the breakthrough time, stoichiometric breakthrough time, and total bed capacity. The analysis reveals that (for both test stands) the greatest uncertainties in the effluent concentration come from three parameters: LDF coefficient, void fraction, and pellet density. In addition to these parameters, uncertainty in axial dispersion is also important for test stand A. This is because wall channeling due to the small pellet-to-canister diameter ratio in test stand A results in significant axial mixing, which is not captured by the empirical correlations used to predict axial dispersion, as these correlations only account for pellet-driven dispersion. Thus, the baseline dispersion is almost an order of magnitude larger than the dispersion simulated for the uncertainty analysis.

Figure 2.10 shows the breakthrough curve of the four simulations for which the axial dispersion and the LDF coefficient were held at their upper or lower uncertainty bounds, in addition to the baseline results. As expected, it shows that the slope of the breakthrough curve increases as the LDF coefficient is increased from the baseline value, causing the bed to breakthrough earlier; decreasing the LDF has the opposite effect on breakthrough time. Simulations run using the upper and lower bounds of axial dispersion coefficient, D_{ax}, deviate significantly from the baseline in

test stand A. Both cases show a similar steepening of the curve which causes the breakthrough time to increase. The deviation in test stand A is due to the extremely high experimentally measured D_{ax} that is an order of magnitude larger than even the upper uncertainty bound on D_{ax}. We note that Figure 2.10 shows negligible deviation from the baseline case in test stand B as D_{ax} is changed. This is consistent with the results of Knox[44], who found that it is important to accurately capture the effects of wall channeling in small-diameter, fixed adsorbent beds. The high axial dispersion, which we found by fitting to experimental data, decreased the breakthrough time by 24% compared to *ad hoc* empirical predictions in test stand A (Table 2.8). This significant change in breakthrough time directly impacts the adsorption efficiency of the bed. Table 2.8 also shows that varying either the LDF coefficient or the axial dispersion has no effect on the capacity, which is expected considering that these parameters govern only the kinetics (and not equilibrium characteristics) of adsorption. Finally, we note that the uncertainty for both the stoichiometric breakthrough time and total capacity is approximately 1% for both test stands due to the accuracy with which we can determine porosity and void fraction.

We also evaluated the impact of changing the model inputs on the three metrics quantifying the temperature of the gas stream leaving the bed. Both the composition and temperature of this effluent stream are of great interest in modeling multi-bed sorption systems, such as the CDRA and the next generation of four-bed molecular sieves (4BMS), because the effluent of one bed becomes the influent stream of the next. We choose the time at which the maximum outlet temperature is reached as a metric because it quantifies the time at which the thermal wave exits the bed (analogous to the breakthrough time for mass transport). The results are tabulated in Table 2.8. Evaluation of the temperature metrics shows that several parameters are important to the model uncertainty: LDF coefficient, axial dispersion, effective axial thermal conductivity, gas–canister heat transfer coefficient, and canister–insulation heat transfer coefficient. The effect of axial dispersion on temperature is only significant in test stand A due to the order-of-magnitude difference between the predicted axial dispersion and the baseline measured D_{ax} for stand A. The effect of varying LDF coefficient and effective axial thermal conductivity are similar for both test stands; the exit temperature metrics for both test stands follow the same trend and show similar order-of-magnitude changes. However, the effluent temperatures of test stands A and B were sensitive to different heat transfer coefficients. We attribute this to differences in canister material

and thicknesses. Test stand A is constructed of a thin aluminum wall which has minimal thermal capacity and resistance; thus, heat easily flows through the canister wall and into the insulation. Conversely, test stand B has a thick, steel canister wall which acts as a large heat sink during the breakthrough process. Thus, test stand A was more strongly influenced by the canister-insulation heat transfer while test stand B was most strongly affected by the gas-canister heat transfer. It is important to note that the uncertainty bounds for the canister–insulation and insulation–ambient heat transfer coefficients were chosen to be extreme examples (*e.g.*, we vary $h_{\text{can-ins}}$ from 0 to ∞). Even with this very large range of values, the effect on the temperature behavior only changed by a few percents compared to the baseline. This is due to the weak temperature gradients observed during adsorption which are only on the order of 10 K. We expect that the model predictions would be significantly more prone to error due to uncertain heat transfer coefficients when modeling temperature-assisted desorption (where the bed is heated to nearly 300ºC). For test stand A, the maximum temperature rise across the bed is also sensitive to the axial dispersion coefficient; again, this is due to the order-of-magnitude discrepancy of our experimentally measured axial dispersion from the expected range of D_{ax}. The mean temperature rise is proportional to the total energy transferred to the gas-phase during adsorption, which is simply proportional to the total mass of CO_2 adsorbed less the heat loss to ambient and absorbed by the thermal mass of the test stand. As the thermal mass of the bed is small, we see that uncertainty in the mean temperature rise across the bed is mainly influenced by heat loss through the lateral walls.

The effluent temperature of the simulation cases for which the temperature profile was most strongly affected by the uncertain parameter being evaluated is shown in Figure 2.11, along with the baseline case. Figure 2.11a shows that the time to reach the maximum outlet temperature remains largely unchanged for test stand A, while the maximum temperature rise across the bed is strongly influenced by the canister-insulation heat transfer coefficient; the same trend is seen in test stand B, but with the gas-canister heat transfer coefficient having the strong influence (Figure 2.11b). From Figure 2.11b we also see that the upper bound of the effective axial thermal conductivity causes a noticeable drop in the maximum effluent temperature compared with the baseline, while the lower bound has a negligible effect. This is because the axial conduction in the baseline case is very low, much closer to the lower bound than the upper bound.

Table 2.6. Upper and lower bounds of model input parameters for uncertainty analysis.

parameter	**test stand A**		**test stand B**	
	lower bound	**upper bound**	**lower bound**	**upper bound**
linear-driving-force coefficient, k_l, s^{-1}	2.0×10^{-2}	2.2×10^{-2}	2.0×10^{-2}	2.2×10^{-2}
axial dispersion, D_{ax}, m^2/s	1.00×10^{-3}	1.20×10^{-3}	1.03×10^{-3}	1.22×10^{-3}
effective axial thermal conductivity, k_{eff}, W/(m K)	0.454	5.48	0.569	2.847
void fraction, ε	.343	.357	.343	.357
gas-sorbent heat transfer coefficient, $h_{g\text{-}s}$, $W/(m^2K)$	91.4	238	105	276
gas-canister heat transfer coefficient, $h_{g\text{-}can}$, $W/(m^2K)$	12.9	25.9	8.3	16.5
canister-insulation heat transfer coefficient, $h_{can\text{-}ins}$, $W/(m^2K)$	0	∞	0	∞
insulation-ambient heat transfer coefficient, $h_{ins\text{-}amb}$, $W/(m^2K)$	2	25	2	25
sorbent envelope density, ρ_{env}, kg/m^3	1168	1192	1167	1191

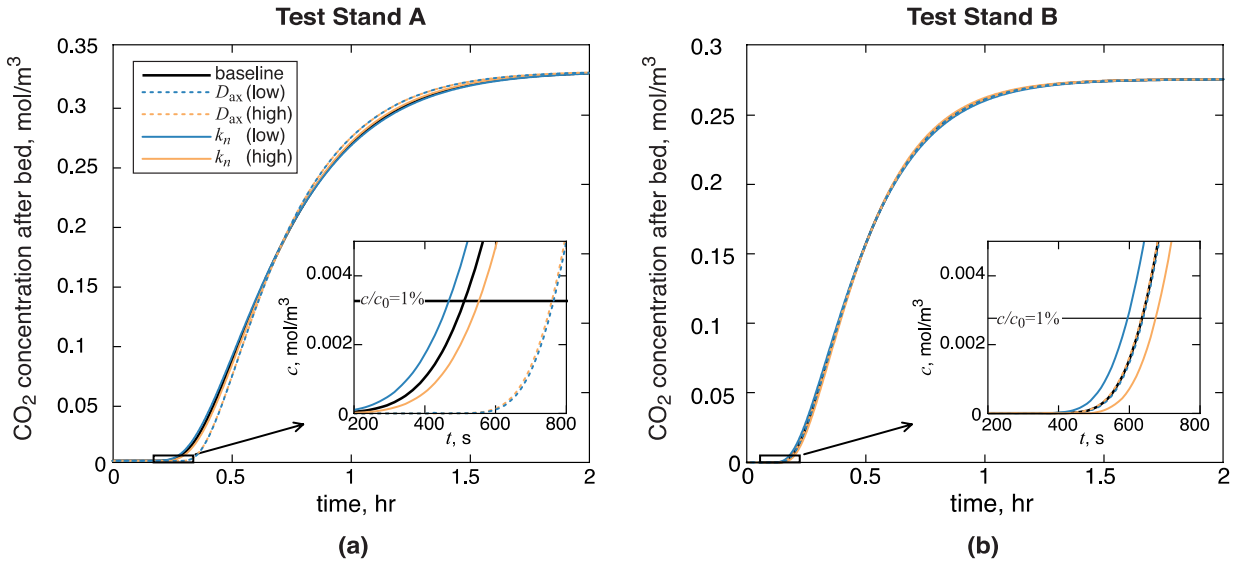

Figure 2.10. For test stand A (a) and test stand B (b): breakthrough curve for the baseline simulation input parameters compared with four simulations where either the LDF coefficient or the axial dispersion coefficient, were set to their upper or lower bound given in Table 2.6. The zoomed-in inset shows the time where the outlet concentration curve crosses the breakthrough point (c/c_0=1%), *i.e.*, the breakthrough time.

Table 2.7. Percent change in breakthrough time, stoichiometric breakthrough time, and total capacity from baseline case for model input parameters evaluated at their upper and lower uncertainty bounds as given in Table 2.6.

	breakthrough time				**stoichiometric breakthrough time**				**total capacity**			
	test stand A		**test stand B**		**test stand A**		**test stand B**		**test stand A**		**test stand B**	
parameter	**low**	**high**	**low**	**high**	**low**	**high**	**low**	**high**	**low**	**high**	**low**	**high**
k_l	-5.0%	4.0%	-6.3%	6.3%	-0.2%	0.1%	0%	0%	-0.3%	0.2%	-0.1%	0.1%
D_{ax}	24.0%	23.0%	0%	0%	0.5%	0.5%	0%	0%	0.7%	0.7%	0%	0%
$k_{eff,ax}$	-1.0%	1.0%	0%	1.6%	0%	-0.1%	0%	0%	0%	-0.1%	0%	0%
ε	2.0%	-3.0%	3.2%	-3.2%	1.1%	-1.1%	1.1%	-1.1%	1.0%	-1.0%	1.1%	-1.1%
h_{g-s}	0%	0%	0%	0%	0%	0%	0%	0%	0%	0%	0%	0%
h_{g-can}	0%	-1.0%	0%	0%	0%	0%	0%	-0.1%	0%	0%	0.1%	-0.1%
$h_{can-ins}$	-1.0%	1.0%	0%	0%	-0.1%	0%	-0.1%	0.1%	-0.1%	0%	-0.1%	0.1%
$h_{ins-amb}$	0%	0%	0%	0%	0%	0.1%	0%	0.1%	-0.1%	0%	0%	0.1%
ρ_{env}	-2.0%	1.0%	-1.6%	3.2%	-1.0%	1.0%	-0.9%	1.1%	-1.0%	1.0%	-0.9%	1.1%

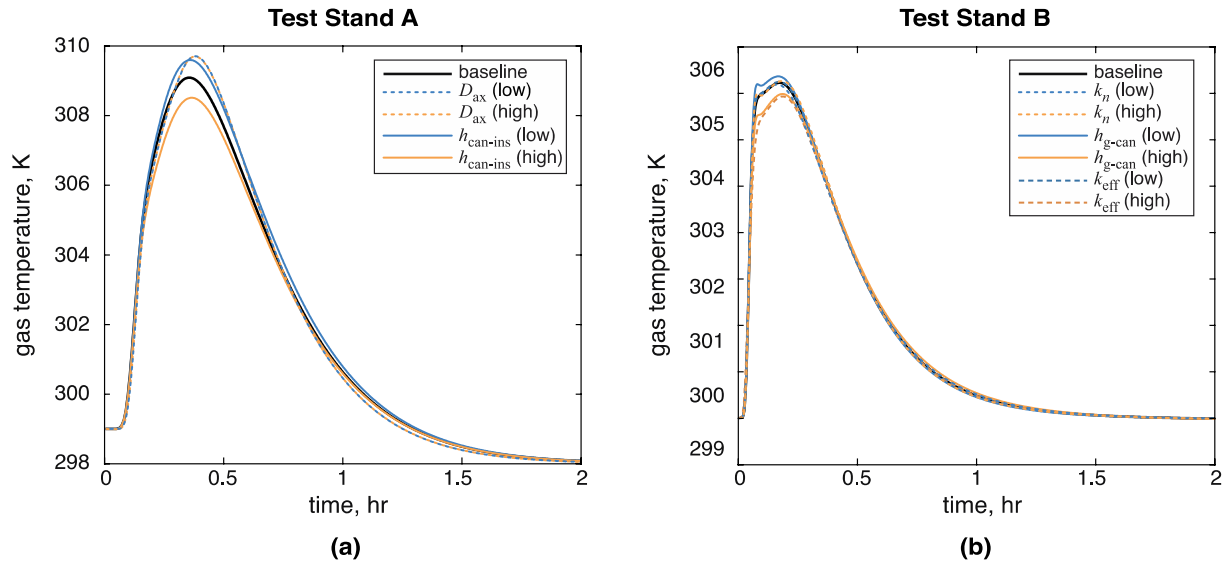

Figure 2.11. For test stand A (a) and test stand B (b): breakthrough curve for the baseline simulation input parameters compared with four simulations where either the LDF coefficient or the axial dispersion coefficient, were set to their upper or lower bound given in Table 2.6. The zoomed-in inset shows the time where the outlet concentration curve crosses the breakthrough point (c/c_0=1%), *i.e.*, the breakthrough time.

Table 2.8. Percent change in maximum/mean temperature rise across the bed from baseline model for model input parameters evaluated at their upper and lower uncertainty bounds as given in Table 2.6.

	time to max outlet temp.				**max temperature rise**				**mean temperature rise**			
	test stand A		**test stand B**		**test stand A**		**test stand B**		**test stand A**		**test stand B**	
parameter	**low**	**high**	**low**	**high**	**low**	**high**	**low**	**high**	**low**	**high**	**low**	**high**
k_l	-1.6%	1.6%	-6.3%	4.8%	-1.2%	1.2%	-0.5%	0.5%	-0.3%	0.3%	0%	0.2%
D_{ax}	7.0%	7.0%	0%	-1.6%	5.8%	5.8%	0%	0%	0.8%	0.8%	0.1%	0.1%
$k_{eff,ax}$	-0.8%	3.1%	-1.6%	6.3%	0.3%	-3.9%	0.3%	-4.1%	0.2%	-2.5%	0.2%	-2.9%
ε	1.6%	-1.6%	1.6%	-3.2%	0.4%	-0.4%	0.1%	-0.1%	1.0%	-1.0%	1.1%	-1.0%
h_{g-s}	0%	0%	0%	0%	0%	0%	0%	0%	0%	0%	0.1%	0.1%
h_{g-can}	-1.6%	1.6%	-4.8%	6.3%	-0.8%	1.9%	1.9%	-3.2%	0%	0%	0.3%	0.2%
$h_{can-ins}$	0.8%	3.1%	0%	-1.6%	4.5%	-5.2%	0%	0.4%	4.7%	-3.8%	2.4%	0.3%
$h_{ins-amb}$	0%	-0.8%	0%	0%	0.2%	-1.4%	-0.1%	0.4%	0.8%	-2.9%	0.1%	0.4%
ρ_{env}	-1.6%	0.8%	-3.2%	1.6%	-0.3%	0.3%	0.3%	0.5%	-1.0%	0.9%	-0.5%	1.4%

2.6 Conclusions

We performed an uncertainty analysis to understand the variation in predictions of a one-dimensional, fixed-bed adsorption model given expected potential deviations in several model input parameters including bed transport properties, heat transfer coefficients, and thermophysical adsorbent properties. The model was calibrated to experimental breakthrough data from two test stands of different lengths and bed-to-pellet diameter ratios. This work is the first documented validation of the calibration method proposed by Knox *et al.* [15]. We showed that the LDF extracted from centerline measurements in the smaller test stand A could be used to predict breakthrough in the larger test stand B yielding excellent agreement with experimental data. The uncertainty analysis was then performed for both test stands to which the model was calibrated by independently changing the model inputs between their lower and upper bounds of their predicted values. The model uncertainty was found by evaluating the resulting change in predicted performance metrics. Metrics such as the breakthrough time, total capacity, and time-averaged temperature rise across the bed were used to evaluate the model's sensitivity to these inputs for breakthrough of CO_2 on zeolite 5A in an N_2 carrier gas. These metrics were selected due to their importance when modeling multi-bed systems. Based on the breakthrough time and capacity, uncertainty in the LDF coefficient and axial dispersion were identified to be the greatest source of model uncertainty. Only two parameters had a notable effect on the stoichiometric breakthrough time or capacity—porosity and pellet density—though the uncertainty in the predicted stoichiometric breakthrough time and capacity were small (~1%). The uncertainty analysis further identified that it is important to accurately predict the axial dispersion coefficient accounting for dispersion effects beyond pellet-driven dispersion. As previously noted by Knox *et al.* [15], empirical prediction of this parameter can induce large errors in beds with small pellet-to-diameter ratio (such as the small channels in a CDRA adsorbent core), due to a failure to account for wall-channeling effects. The analysis also indicated that it is vital to obtain sufficiently accurate measurements of pellet density and bed void fraction to which the performance is highly sensitive. As we transition from a traditional design-build-test approach to simulation-based design, we need a firm understanding of the sensitivities and uncertainties of our models. This work should aid in the design of life support systems for deep space exploration as engineers continue to push the limits of model-based design and optimization.

3. MEASUREMENT AND PREDICTION OF HEAT OF ADSORPTION AND EQUILIBRIUM CONCENTRATION OF CO_2 ON ZEOLITE 13X

This chapter analyses isotherm data from NASA Ames Research Center and NASA Marshall Space Flight Center for CO_2 adsorption on zeolite 13X (Grace Davidson, MS-544HP-13X) over a pressure range of 0.001 kPa to 100 kPa and at ten distinct temperatures ranging from 0 °C to 200 °C. These measurements were originally reported by Huang *et al.* [127] and Cmarik *et al.* [128]. Data were carefully collected to eliminate sources of bias in previous data given by Wang and LeVan [57], where incomplete activation resulted in a reduced capacity. We fit the isotherm data to four isotherm models of increasing complexity (Langmuir, Toth, 2-site Langmuir, and 3-site Langmuir). Two variations are considered for each model, one with a constant saturation capacity and another with a temperature-dependent saturation capacity. The goodness of fit for each model is described both statistically, *via* the average error and correlation coefficient, and by visually comparing to experimental data. We also present the first calorimetric measurements of heat of adsorption for CO_2 on zeolite 13X across a wide range of temperatures (10 °C to 200 °C). The measured heats of adsorption are compared to predictions (using the Clausius-Clapeyron) based on the fitted isotherm models. Recommendations are made on the models to be used for fitting of isotherms and prediction of heats of adsorption for carbon dioxide on zeolite 13X.

The material presented in this chapter was published in the *Journal of Chemical Engineering Data* [129].

3.1 Experimental methods

3.1.1 Materials

The adsorbent material used for isotherm and heat of adsorption measurements is zeolite 13X (Grace Davidson, MS544-13X, Lot 1000216159). The sorbent is characterized in the manufactured form as pelletized, spherical pellets with a mean diameter of 2.1 mm. The CO_2 (99.99% purity) and He (99.995% purity) gases were supplied by Airgas (for measurement of isotherms from 0 °C to 75 °C) and Sexton Welding Supply Co. (for measurement of isotherms from 100 °C to 200 °C and all heat of adsorption measurements). Note that zeolite 13X is a

commercial name for sorbents comprised of type X zeolite skeletal structure with Na^+ as the major cation which are generally referred to as NaX zeolites. In this dissertation, we reserve NaX to describe studies on pure NaX-zeolite crystals that are not pelletized.

3.1.2 Apparatus and procedure: equilibrium adsorption isotherms

Isotherms for carbon dioxide adsorption on zeolite 13X were measured from 0 °C to 200 °C at intervals of 25 °C (with an additional measurement at 10 °C) and at equilibrium pressures ranging from 1×10^{-4} kPa to 100 kPa. Both low- and high-temperature isotherms were measured using a static volumetric type of apparatus following similar procedures. The low-temperature (0 °C to 75 °C) isotherms were collected at NASA Ames, as originally reported by Huang *et al.* [127], using a physisorption volumetric analyzer (Micromeritics ASAP 2020) and a water/glycol bath to control the temperature to within ±0.3 °C. The high-temperature isotherms (100 °C to 200 °C) were collected at NASA Marshall; these data are published in a technical memo by Cmarik *et al.* [128] without details on the measurement technique. The following is a detailed description of the measurement approach.

The high-temperature isotherms (100 °C to 200 °C) were measured with a physisorption volumetric analyzer (Quantachrome Autosorb-1C), equipped with a furnace which maintained the sample temperature constant with a precision of ±0.3 °C as monitored using RTD sensors. Additionally, the sample mass was measured (to determine loading) by activating the sample and measuring the mass on a balance (Scientech SA210, ± 0.1 mg accuracy).

After placing ~400 mg of zeolite 13X into the sample tube, the sorbent was activated by heating to 350 °C (at 1.8 °C/min) then holding it at this temperature under vacuum (< 1 mTorr) for 4 hr. This high activation temperature is necessary to completely desorb the zeolite of water; the authors found that lower activation temperatures (even at 300 °C) gave inconsistent results that were attributed to residual water loading affecting the CO_2 capacity. After the sample was activated, the sample tube was backfilled with helium to prevent ambient air from leaking into the tube while the sample was cooled to the measurement temperature.

The following is a description of the automated volumetric method used to measure loading at a single temperature (isotherm) across a range of pressures. First, helium gas is used to measure the free volume in the sample tube by injecting a known quantity of helium into the analysis manifold. The analysis manifold is a stainless-steel chamber of precisely known volume that is instrumented with high sensitivity pressure transducers (MKS Baratron, ±0.15% of reading accuracy) and a platinum resistance device (RTD, ± 0.3 °C). The mass of the injected helium is found from the known manifold volume and the measured pressure using the real-gas equation of state (*i.e.*, the ideal gas equation with compressibility factor). The manifold is then opened to the sample tube, allowing helium to flow into the zeolite pore space. The volume of the sample can then be calculated using the difference in pressures before and after opening the analysis manifold to the sample tube, assuming there is no adsorption of helium onto the pellets. After evacuating both the sample tube and analysis manifold, the adsorbed-phase equilibrium concentration is measured by first injecting a known quantity of CO_2 into the analysis manifold and then exposing the sample to this gas. The final pressure of CO_2 is measured after equilibrium is reached. A mass balance accounting for the state before and after CO_2 dosing allows calculation of the mass of CO_2 adsorbed on the sample. The two chambers are again separated by closing a valve, and more CO_2 is injected into the control-volume chamber. The pressure in this chamber is recorded before and after exposing the sample to this increased amount of CO_2. This process of increasing the CO_2 concentration, exposing the sample, and recording the change in pressure (*i.e.*, change in mass adsorbed) is repeated to obtain the equilibrium concentration of CO_2 at several partial pressures and a single temperature (isotherm). This entire process was repeated to obtain isotherms at ten different temperatures between 0 °C and 200 °C.

While it is difficult to quantify the measurement uncertainty of the closed-boxed commercial instruments used to measure the isotherms, we expect the intra-operator variability [127] and lot-to-lot variations [58] to dwarf any instrumentation uncertainty. We instead quantify the repeatability of our measurements as an indication of the measurement fidelity. All experimental values were measured in duplicate with a resulting repeatability (within a single lot) within 1.5%.

3.1.3 Apparatus and procedure: heat of adsorption

The calorimetric measurements of the heat of adsorption for carbon dioxide on zeolite 13X are measured from 25 °C to 200 °C at intervals of 25 °C (with an additional measurement at 10 °C) at CO_2 partial pressure of 0.17 kPa to 20.3 kPa. These measurements are made using simultaneous thermogravimetric and differential scanning calorimetry (Setaram, Sensys EVO TG-DSC) as shown in Figure 3.1. The TG-DSC combines the ability to measure mass changes in the sample at precisely controlled temperature (±0.1 °C) conditions with the ability to measure the heat released during adsorption. The main portion of the TG-DSC comprises two parallel channels formed by alumina tubes. There is a wire basket suspended in each channel; these baskets hang on a microbalance that measures the mass difference between the two.

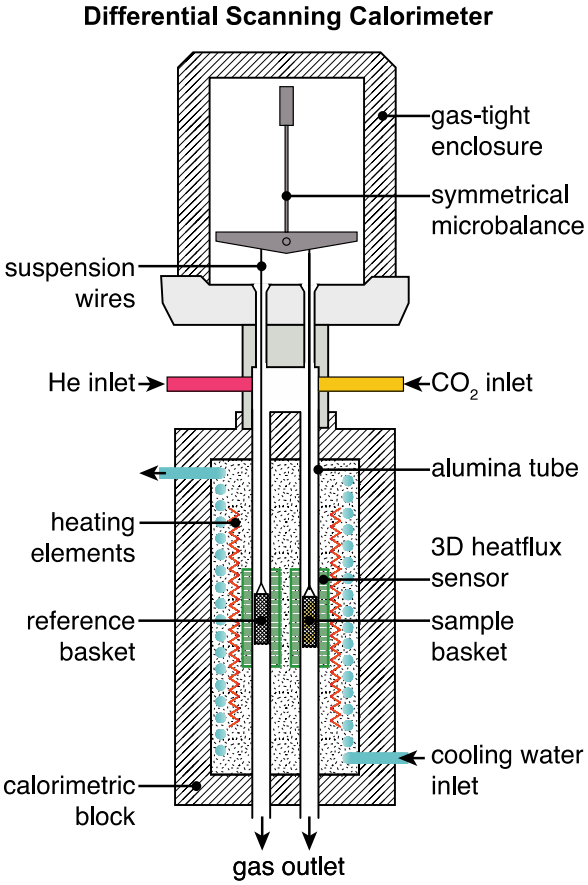

Figure 3.1. Schematic of the thermogravimetric, differential scanning calorimeter (TG-DSC) used to measure the heat of CO_2 adsorption on zeolite 13X pellets.

All measurements in the DSC were carried out under a flow of mixed He and CO_2 at atmospheric total pressure. The total flow rate was held constant at either 150 mL/min or 50 mL/min while adjusting the relative flow rates of He and CO_2 to obtain the desired CO_2 partial pressure. The He and CO_2 gas streams are controlled by separate flow controllers and mix in the dead-space above the channels. The mixed gas stream then splits and flows through the two channels in parallel. Before beginning measurements, the flow is adjusted to ensure equal distribution to each channel (*e.g.*, 150 mL/min total flow rate equates to 75 mL/min per channel). For clarity, all reported flow rates in this chapter are total flow rates.

After taring the balance with the two empty baskets, a sample of zeolite pellets (~60 mg) is added to the sample basket (on the right in Figure 3.1). The other basket remains empty and acts as a reference during the experiment. Both chambers are mounted in a calorimetric block that is water-cooled and joule-heated. The sample is activated *in situ* before each isothermal measurement at 350 °C under a flow rate of He of 150 mL/min for 2 hr. The sample was then cooled to the measurement temperature and allowed to thermally equilibrate with He continuing to flow at the total measurement flow rate (either 150 mL/min or 50 mL/min). Once the temperature stabilizes, a small portion of CO_2 begins to flow into the chambers at a rate of 0.25 mL/min; note that the helium flow rate is reduced to maintain a constant total flow rate. The He and CO_2 flow rates are maintained for 0.5 to 2 hours until equilibration of the adsorption of CO_2 on the sample is reached; during this time, the sample chamber requires less heating than the reference chamber to maintain a constant temperature due to the exothermic adsorption process. The DSC measures the difference in heat flow between the two chambers, Q, which can be used along with the change in sample mass, (m_i-m_f), to compute the heat of adsorption per mol of CO_2 adsorbed, λ, as

$$\lambda = \frac{Q}{\left(m_i - m_f\right) M_{CO_2}} \tag{3.1}$$

where M_{CO_2} is the molar mass of carbon dioxide. After the sample mass reaches equilibrium, the CO_2 flow rate is increased to 0.5 mL/min and again allowed to equilibrate. This step-wise process of increasing the CO_2 flow rate is repeated for CO_2 flow rates of (0.25, 0.5, 1, 2, 4, 6, 8, and 10) mL/min, corresponding to CO_2 partial pressures of 0.17 kPa to 6.7 kPa at a 150 mL/min total flow

rate and 0.51 kPa to 20.3 kPa at a 50 mL/min total flow rate. This measurement was repeated at nine different temperatures between 10 ℃ and 200 °C.

The uncertainty in the calculated heat of adsorption is determined using the root sum of the squares method accounting for both the microbalance accuracy and heat flux sensor accuracy which were observed to be approximately ±0.1 mg and ±5% of the reading, respectively.

3.2 Isotherm models fitting

Per the International Union of Pure and Applied Chemistry's (IUPAC) recommendations on the classification of gas-solid adsorption isotherms [130], the experimental isotherms obtained are of type I because the isotherm monotonically increases and approaches a limiting value at high pressures. Type I isotherms are observed for microporous solids, such as zeolites, where the capacity is limited by the accessible micropore volume rather than by the internal surface area.

In the present chapter, the experimental adsorption equilibrium data obtained are fit to the commonly used theoretical model of Langmuir [131] and semi-empirical Toth model [95], as well as the less-common multisite Langmuir model [124], [132]. Each model is fit both with and without the saturation capacity having temperature dependence. The resulting goodness of fits are then compared between models and recommendations are made for which model to use.

3.2.1 Langmuir model

The Langmuir isotherm describes monolayer adsorption on homogeneous flat surfaces. This isotherm assumes: (1) ideal gas at isothermal conditions; (2) adsorbed molecules are held at definite, localized sites which each can accommodate only one molecule; (3) the adsorption energy is constant over all sites (homogeneous surface); and (4) there is no interaction between neighboring adsorbate molecules. Based on the concept of dynamic equilibrium between the rate of adsorption and desorption, the amount adsorbed, n, is given as

$$n = \frac{abp}{1+bp} \tag{3.2}$$

where *a* and *b* are the saturation capacity and affinity parameter, respectively, and *p* is the adsorbate pressure. The saturation capacity and affinity parameter as functions of temperature are respectively given as

$$a = a_0 + c_0/T \quad \text{and} \quad b = b_0 \exp\left[\frac{E}{RT}\right] \qquad 3.3,3.4$$

where a_0, c_0, b_0, and *E* are fitted parameters. This version of the Langmuir model is sometimes referred to as the multitemperature Langmuir model because of the temperature dependence of *b*; because all our models account for the temperature dependence of *b*, we will drop the multitemperature adjective from the model names. The pre-exponential factor, b_0, is the affinity parameter and *E* is the adsorption energy of the single adsorbate. The product *ab* is often termed the Langmuir constant (or Henry's constant). The Langmuir isotherm reduces to Henry's law, $n = abp$, when the adsorbate concentration *n* is very low. The Langmuir isotherm can be simplified by neglecting the temperature dependence of the saturation capacity (*i.e.*, $c_0 = 0$) to reduce the number of fit parameters by one.

3.2.2 Toth model

The Toth isotherm is a popular empirical fit which satisfies Henry's law and yields a finite adsorbate concentration at high pressures. This semi-empirical model accurately describes many type-I isotherms, and it has the following form:

$$n = \frac{abp}{\left[1+(bp)^f\right]^{1/f}} \qquad 3.5$$

where, *a* and *b* are the saturation capacity and affinity parameter as given in Eqs 3.3 and 3.4, respectively. The Toth model includes an additional parameter to account for surface heterogeneity; this the temperature-dependent heterogeneity parameter is given as

$$f = f_0 + \alpha/T\ . \qquad 3.6$$

Eq. 3.5 reduces to the Langmuir isotherm when $f = 1$. The heterogeneity parameter is expected to approach unity as the temperature increases so that $f_0 \sim 1$.

3.2.3 Multisite-Langmuir model

The Langmuir model can be extended to account for surface heterogeneity by assuming that the adsorbent that is composed of *k* homogeneous, but energetically different, patches (or sites). This model is commonly called the dual-site Langmuir when *k*=2. All the assumptions of the Langmuir model apply to each individual site, and the sites do not interact with each other. Assuming the adsorbate-adsorbent free energy on each site is constant, the loading can be described as a summation of Langmuir isotherms, one for each site

$$n = \sum_{j=1}^{k} \frac{a_j b_j p}{1 + b_j p} \tag{3.7}$$

where a_j and b_j are respectively the saturation capacity and affinity parameter on the j^{th} site, and p is the adsorbate pressure. The saturation capacity and affinity parameter for each site are functions of temperature given as

$$a_j = a_{0,j} + c_{0,j}/T \quad \text{and} \quad b_j = b_{0,j} \exp\left[E_j / (RT)\right] \tag{3.8,3.9}$$

where $a_{0,j}$, $c_{0,j}$, $b_{0,j}$, and E_j are fitted constants for the j^{th} site. These parameters are analogous to their namesakes in the traditional Langmuir formulation. Henry's law constant is simply the sum of those on each site (*i.e.*, $\sum a_j b_j$).

3.2.4 Fitting method

The Generalized Reduced Gradient (GRG) nonlinear solving method was custom implemented using Excel to find the parameters which minimized the sums of squares error, *SSE*, defined as

$$SSE = \sum \left(n_{\text{pred}} - n_{\text{meas}}\right)^2 \tag{3.10}$$

where n_{meas} is the measured amount adsorbed and n_{pred} is the predicted amount adsorbed based on the isotherm model and fit parameters. The *SSE* is found by summing over all experimental measurements; thus, regions of data with higher pressures and lower temperatures having larger absolute values of n_{meas} and n_{pred} will lead to higher absolute differences and will be more emphasized in the resulting fit. The GRG nonlinear solver is converged to a residual of 1×10^{-12}. To improve convergence and prevent ill-conditioning, the parameters actively modified by the

solver are normalized to be the same order of magnitude every 1000 iterations. This is done by dividing the actual model fit parameters by their order of magnitude to obtain a value of ~1.

3.3 Prediction of the heat of adsorption

In *lieu* of direct measurement, the heat of adsorption can be indirectly estimated from the equilibrium adsorption isotherm using the Clausius−Clapeyron equation,

$$\lambda = RT^2 \left[\frac{\partial \ln p}{\partial T} \right]_n = -R \left[\frac{\partial \ln p}{\partial (1/T)} \right]_n \tag{3.11}$$

where R is the universal gas constant, p is the adsorbate pressure, and T is the temperature. Eq. 3.11 assumes that the gas-phase and adsorbed-phase are at the same temperature, ideal gas behavior, and that the adsorbed phase volume is negligible. The subscript n indicates the adsorbed-phase concentration is held constant while evaluating the partial derivative. Eq. 3.11 can be rewritten using the triple chain rule as [16]

$$\lambda = -\frac{RT^2}{p} \left(\frac{\left[\frac{\partial n}{\partial T} \right]_p}{\left[\frac{\partial n}{\partial p} \right]_T} \right) \tag{3.12}$$

where n is the adsorbed-phase concentration of adsorbate. Eq. 3.12 allows the heat of adsorption to be expressed as an analytic expression for any adsorption isotherm in the form $n = f(p,T)$ by simple partial differentiation of the isotherm model. The isosteric heat of adsorption can be predicted from the Langmuir isotherm found by substituting Eq. 2 into the Clausius-Clapeyron equation,

$$\lambda = -\frac{RT^2}{p} \left(\frac{\left[\frac{\partial n}{\partial T} \right]_p}{\left[\frac{\partial n}{\partial p} \right]_T} \right) = E + \frac{c_0 R}{a} (1 + bp) . \tag{3.13}$$

If the saturation capacity is held constant (*i.e.*, $c_0 = 0$), Eq. 3.13 reduces to

$$\lambda = E . \tag{3.14}$$

The isosteric heat of adsorption predicted from the multisite-Langmuir model is found by the same procedure to be:

$$\lambda = -\left(\frac{\sum_{j=1}^{k} \left(R\frac{c_{0,j}b_j}{1+b_j p} + E_j \frac{a_j b_j}{\left(1+b_j p\right)^2} \right)}{\sum_{j=1}^{k} \frac{a_j b_j}{\left(1+b_j p\right)^2}} \right). \quad 3.15$$

To predict the isosteric heat of adsorption from the Toth isotherm Eq. 3.5 is substituted into the Clausius-Clapeyron equation to find:

$$q = RT^2 \left[\frac{\partial \ln p}{\partial T} \right]_n = E + \frac{1}{f} R\alpha \left(\ln\left(bp\right) - \left[1+\left(bp\right)^f\right] \ln\left[\frac{bp}{\left(1+\left(bp\right)^f\right)^{1/f}} \right] \right) + R\frac{c_0}{a}\left(1+\left(bp\right)^f\right). \quad 3.16$$

3.4 Results and discussion

3.4.1 Comparison of isotherm data to literature

A comparison of the current isotherm results for carbon dioxide adsorption on zeolite 13X, measured at 25 °C and at equilibrium pressures ranging from 1×10^{-4} kPa to 100 kPa, to data from the literature is presented in Figure 3.2, which shows the equilibrium capacity of zeolite 13X as a function of CO_2 pressure. The data from Rege *et al.* [133] have the same slope as the current results in the low-pressure region but show a higher loading capacity. We attribute this difference to the variation in 13X samples characterized. Rege *et al.* [133] measured the 25 °C isotherm for CO_2 adsorption on pure zeolite X crystals (*i.e.*, no binder) whereas our sorbent was mixed with a small amount of binder to form pellets. The 25 °C isotherm from the present data were normalized against the data of Rege *et al.* [133] to estimate the binder content of Grace Davidson MS544-13X sorbent as being 18% by mass.

The effect of incomplete activation is also seen in comparing the current data to those of Wang and LeVan [57]. Both use the same zeolite 13X (Grace Davidson, MS 544HP), but the current data involved activation at 350 °C compared to a lower temperature of 175 °C used by Wang and LeVan [57] (both under vacuum). This high activation temperature of 350 °C was selected after an extensive comparison of isotherms from four separate research facilities (NASA Marshall, NASA Ames, University of South Carolina, and Vanderbilt University) showed that lower temperatures

(*e.g.*, 300 °C) caused an incomplete desorption of water and resulted in discrepancies between different isotherm measurements [58], [134, Fig. 6.2]. All discrepancies between the different research facilities and measurement techniques (*e.g.*, gravimetric versus volumetric) were resolved by using an activation temperature of 350 °C.

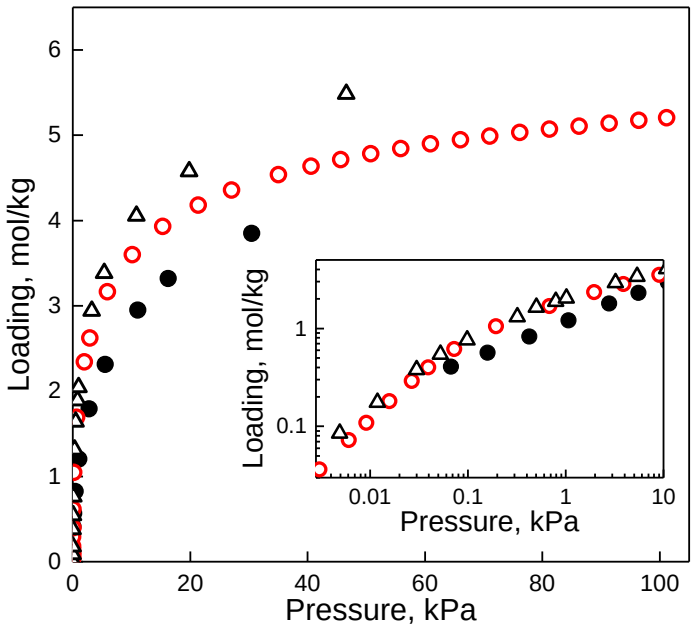

Figure 3.2. Comparison of 25 °C adsorption isotherms for CO_2 on zeolite 13X: current data (○), Rege *et al.* [133] (△), Wang and LeVan [57] (●).

The dimensionless Henry's constants, k_H, were determined from virial plots for each of our measured isotherms. These constants are listed in Table 3.1 and plotted as a function of $1/T$ in Figure 3.3. The temperature dependence of k_H can be expressed using the van't Hoff equation,

$$k_H = k_{H,0} e^{(-\Delta U/RT)} \qquad 3.17$$

where ΔU represents the change in internal energy at very low loadings and k_{H2O} is the limit of Henry's constant as $T \rightarrow \infty$. We fit our data using Eq. 3.17 to find $k_{H2O} = 7.44\times10^{-4}$ and $-\Delta U/R = 5230$ K. Figure 3.3 also plots k_H from Brandani *et al.* [135] for comparison; these constants were measured for CO_2 adsorption on a commercial low-silica zeolite X (Si/Al ratio of 1.0 and 18% clay binder by mass) using the zero-length column technique. These data sets match both in terms of slope and magnitude.

Table 3.1. Dimensionless Henry's constant, k_H, as a function of temperature.

***T*, °C**	k_H	***T*, °C**	k_H
0	158,000	100	836
10	83,700	125	358
25	32,600	150	178
50	7,140	175	102
75	2,260	200	46.5

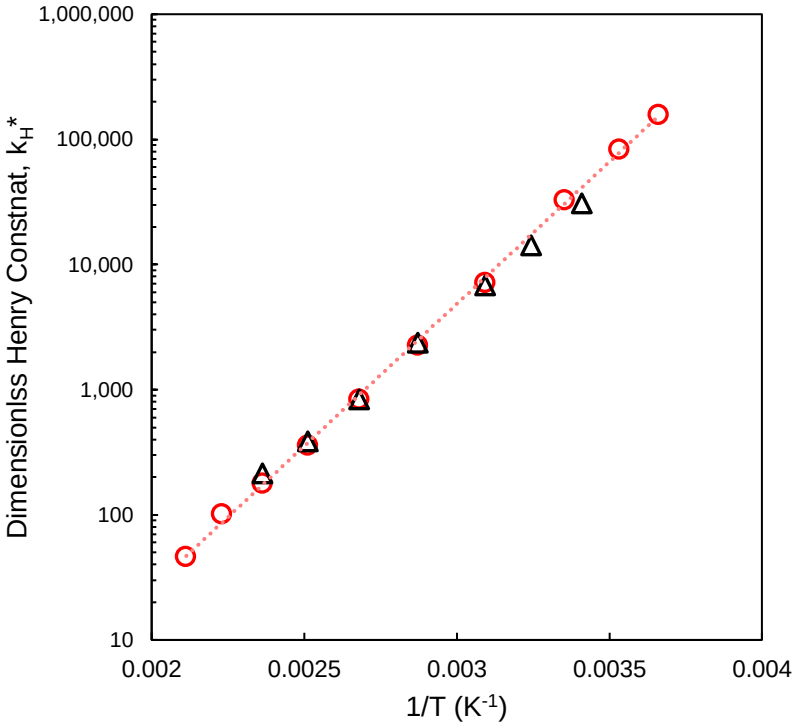

Figure 3.3. van't Hoff plot showing the temperature dependence of the dimensionless Henry's constants for CO_2 adsorption on zeolite 13X: current data (○), least-squares fit of Eq. 3.17 to current data (dashed line), Brandani *et al.* [136] (△)

3.4.2 Comparison of isotherm data to fitted models

The accuracy of each model fit to the experimental data is quantified using the root-mean-square error (*RMSE*), the maximum error, and the regression coefficient (R^2) as given in Table 3.2. The goodness of fit increases with the number of fit parameters as shown by the data in Table 3.2; however, this improved match against the experimental data comes at the expense of increased model complexity and risk of over-fitting. For example, the most complex 3-site Langmuir model with temperature-dependent saturation capacity, *a*, has the lowest overall error as evident by the *RMSE* and R^2 values (0.0313 mol/kg and 0.9997 respectively). However, the maximum error of this model is larger than that of a 3-site Langmuir with constant *a* due to overfitting; the latter model also fits the data exceptionally well (*RMSE* = 0.0337 mol/kg, R^2 = 0.9996), but has three fewer parameters, which reduces the risk of overfitting.

In general, including the temperature-dependent term in the saturation capacity does not significantly improve the goodness of fit for any of the models (*e.g.*, *RMSE* decreases by no more than 21%). Furthermore, there is a diminishing improvement in the goodness of fit as the number of fit parameters increases, indicating that a more complex model does not necessarily improve the prediction further. These goodness-of-fit statistics provide an objective comparison of the different models; however, it is also important to evaluate the distribution of errors before selecting a recommended fit.

Table 3.2. Comparison of the goodness of fits for different the isotherm models.

model	**No. of fit parameters**	***RMSE*, mol/kg**	**maximum error, mol/kg**	**R^2**
Langmuir (constant *a*)	3	0.3670	0.952	0.9526
Langmuir	4	0.3128	0.826	0.9656
Toth (constant *a*)	5	0.0682	0.153	0.9984
Toth	6	0.0680	0.152	0.9984
2-site Langmuir (constant *a*)	6	0.0641	0.23	0.9986
2-site Langmuir	8	0.0507	0.165	0.9991
3-site Langmuir (constant *a*)	9	0.0337	0.089	0.9996
3-site Langmuir	12	0.0313	0.11	0.9997

Figure 3.4 shows the experimentally measured isotherms compared with predictions for the Langmuir, Toth, 2-site Langmuir, and 3-site Langmuir models, both with temperature-dependent saturation capacity (solid lines) and with constant saturation capacity (dashed lines). For clarity, a reduced number of representative experimental points are included in Figure 3.4.

The Langmuir model poorly fits the measured isotherms at low temperatures (Figure 3.4). This agrees with the analysis of Khelifa *et al.* [137], who found that the Langmuir model (with no temperature-dependent parameters) poorly fit measured isotherms for several zeolite 13X samples at 0 °C and 30 °C. Choudhary *et al.* [138] likewise used a temperature-independent Langmuir model to individually fit two CO_2/13X isotherms at 32 °C and 80 °C. They observed a good match between the models and data; it should be noted, however, that they fit to sparse data (*e.g.,* 5 independent pressures), making it difficult to draw general conclusions about the goodness of fit. The Langmuir model shows the greatest change between the model fits with constant and temperature-dependent saturation terms. Figure 3.4 shows that the isotherms of these two models show very different slopes and actually cross over each other at low temperatures. While including the temperature-dependent term of a improves the model's agreement at higher pressures, there is still a large error at low temperatures (below approximately 100 °C). Furthermore, although Langmuir model with temperature-dependent a better matches the magnitude of measured isotherms, the Langmuir model with constant a more closely agrees with the slope of the measured data. We conclude that the Langmuir model inadequately captures the adsorption of CO_2 on zeolite 13X, even when allowing for temperature dependence of the saturation capacity.

In contrast, the Toth models with and without temperature-dependent a show negligible differences; they overlap in Figure 3.4 so much as to be indistinguishable. Both Toth models agree well with the measured data across the entire range of temperatures but not across the entire pressure range. Though all the isotherm models considered in this chapter obey Henry's law in low-pressure region, this behavior is not clearly identifiable for the Toth isotherms as plotted in Figure 3.4. Henry's law is a thermodynamic constraint which states that the amount adsorption will increase linearly with concentration at low pressures. This linear relation is only visually apparent for the Toth isotherms at extremely low pressures (~1×10^{-6} kPa), well below the limits of Figure 3.4. Though the Toth model captures the correct thermodynamic behavior, it diverges from

the measured data as pressure decreases (Figure 3.4). Even with this deviation from measured in the low-pressure region, both the Toth models outperform the Langmuir models. Wang and LeVan [57] similarly concluded that while the Toth isotherm gave the best agreement with their data (CO_2/13X adsorption for -45 °C to 175 °C), other models provided a better fit in the low-pressure range.

The 2-site Langmuir model shows excellent agreement with the measured isotherms. The model matches both the slope and magnitude of the measured data at low pressures as seen in the log-scale plot of Figure 3.4. Both the constant and temperature-dependent saturation capacity models continue to agree with the data as pressure increases. Note that there is a small deviation from measurements at the highest pressures for 0 °C which is slightly reduced by accounting for the temperature dependence of the *a*. We conclude that the 2-site Langmuir model with constant *a* is the simplest model which correctly captures the measured equilibrium isotherm behavior across the entire range of temperatures and pressures. Allowing *a* to vary with temperature results in a small improvement of the fit at the lowest temperatures and highest pressures.

Increasing the complexity to a 3-site Langmuir model provides a negligible improvement over the 2-site Langmuir model when comparing the fits in Figure 3.4. The difference between 2- and 3-site Langmuir is only evident from the goodness-of-fit metrics in Table 3.2. Based on this marginal improvement, and the unnecessary increase in complexity of the 3-site Langmuir model, we recommend using the 2-site Langmuir fitted model with constant saturation capacity for CO_2 adsorption processes on zeolite 13X. The fit parameters for this model are given in Table 3.3. Fit parameters for the other models considered in this chapter are listed in Appendix B. We advise using the isotherms only within the bounds of the experimental measurements (*i.e.*, 0.001 kPa to 100 kPa and 0 °C to 200 °C).

Table 3.3. Fit parameters for the 2-site Langmuir isotherm for CO_2 adsorption on zeolite 13X.

j (site)	$a_{0,j}$, mol/kg	$b_{0,j}$, kPa^{-1}	E_j/R, K
1	2.219	5.866×10^{-8}	5401
2	3.602	4.436×10^{-8}	4197

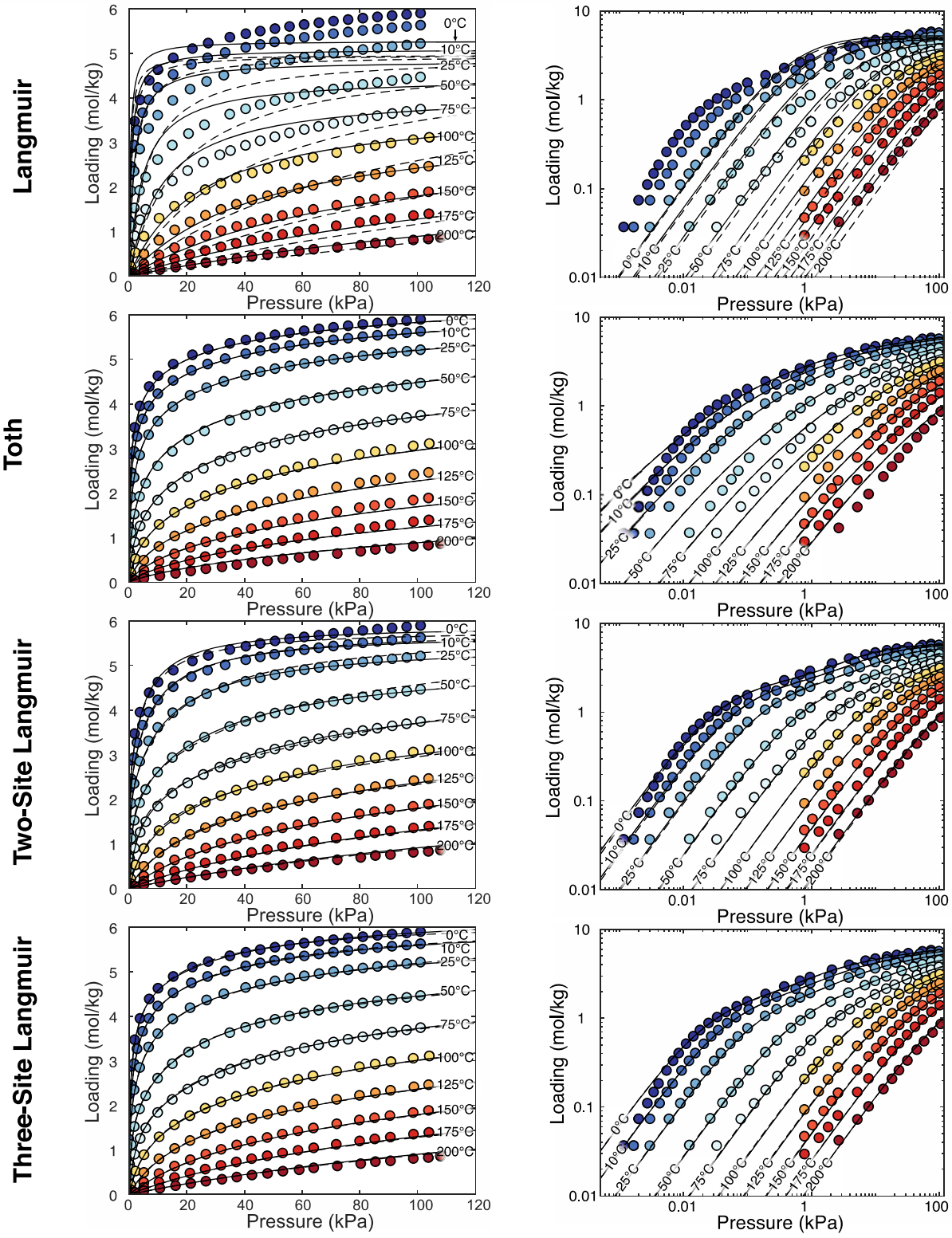

Figure 3.4. Measured isotherms (filled symbols) for CO_2 adsorption on zeolite 13X compared to model fits with either constant saturation capacity (solid lines) or temperature-dependent saturation capacity (dashed lines).

3.4.3 Comparison of heat of adsorption data to literature

We compare our heat of adsorption measurements at 25 °C to calorimetric measurements from the literature in Figure 3.5. Of these studies, half used pure NaX crystals [66], [68], [71], [72] (open symbols) while the others used commercially available, clay-bound zeolite 13X [67], [70], [73] (closed symbols). Note that the measurements of Bläker *et al.* [69], which were conducted using clay-bound zeolites, are not shown in Figure 3.5 for clarity because of a large amount of noise in their data.

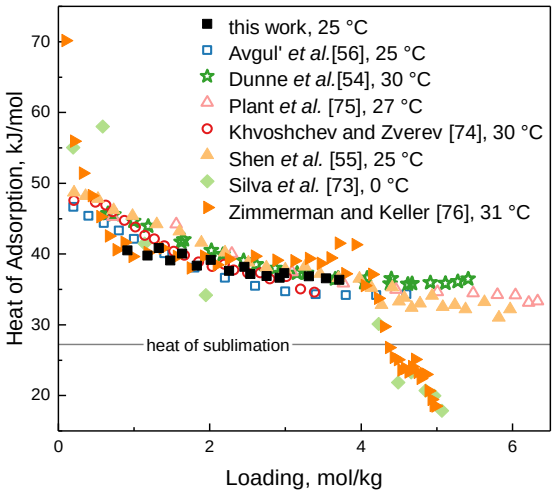

Figure 3.5. Comparison of the heat of adsorption of CO_2 on NaX zeolites found *via* calorimetric measurement. Open symbols denote measurements using pure zeolite crystals while closed symbols were using samples of zeolite pelletized with 20% binder.

Our data closely match other values from the literature, which all have similar values and trends at low loadings (<4 kJ/mol). Dunne *et al.* [66] found that the heat of CO_2 on NaX decreases sharply from 49 kJ/mol at the limit of zero loading, then gradually declines to a plateau value of 36 kJ/mol. The initially high heat of adsorption is due to the preferential interaction of CO_2 with stronger sites. Once these strong sites are filled, the heat of adsorption decreases as CO_2 begins filling weaker sites. This is typical behavior for microporous adsorbents and indicates the presence of chemical heterogeneities or specific adsorption sites of differing strength [74]. Avgul' *et al.* [68], Shen *et al.* [67] and Khvoshchev and Zverev [71] all observed similar trends with minor variations between the initial heat of adsorption and final plateau.

Notably, two studies [70], [73] measured a sharp decrease in the heat of adsorption at loadings above 4 mol/kg. Silva *et al.* [70] attributed this behavior to macroscopic condensation occurring in the larger pores of the adsorbate after the micropores were filled. Zimmerman and Keller [73] likewise attributed the decrease in heat of adsorption at high loadings to condensation and claimed that other studies did not observe this behavior because they used pure zeolites whereas their measurements were taken on sorbent pellets comprised of ~20% clay binder. This is contradicted by the results of Shen *et al.* [67], who used the same commercially available zeolite 13X (Honeywell UOP) as Zimmerman and Keller [73], but did not observe a steep drop in heat of adsorption at high loadings. Further experimental investigation of the heat of adsorption at high loadings is needed to explain this discrepancy.

3.4.4 Comparison heat of adsorption data to predictions

Figure 3.6 shows the experimentally measured heat of adsorption plotted as a function of CO_2 loading for temperatures between 10 °C and 200 °C. For clarity, data at low loadings with large uncertainties ≥25% are excluded from the plots, and only a reduced number of representative experimental points are shown. The original data are all given in Appendix A along with their respective uncertainties. Above loadings of ~1 mol/kg, the experimental data show a decreasing trend with increasing loading; there is insignificant temperature-dependence at these loadings. As mentioned previously, when comparing our experimental measurements at 25 °C to values from the literature, this decreasing trend with loading is expected for materials with type-I isotherms [74]. Below loadings of 1 mol/kg, the heat of adsorption shows a wide spread between different temperatures. No further conclusions can be drawn regarding the trends in this region given the relative uncertainty of the data.

Figure 3.6 also shows the heat of adsorption predicted *via* the Clausius-Clapeyron equation for each of the eight fitted isotherm models. Comparing these predictions against measurements highlights the pitfalls of using complex isotherm models with multiple fit parameters to predict the heat of adsorption. The Langmuir model with constant saturation capacity describes a completely homogenous material; this results in the prediction of a constant λ from the Clausius-Clapeyron equation. Interestingly, this constant λ predicted from the simplest isotherm model closely match

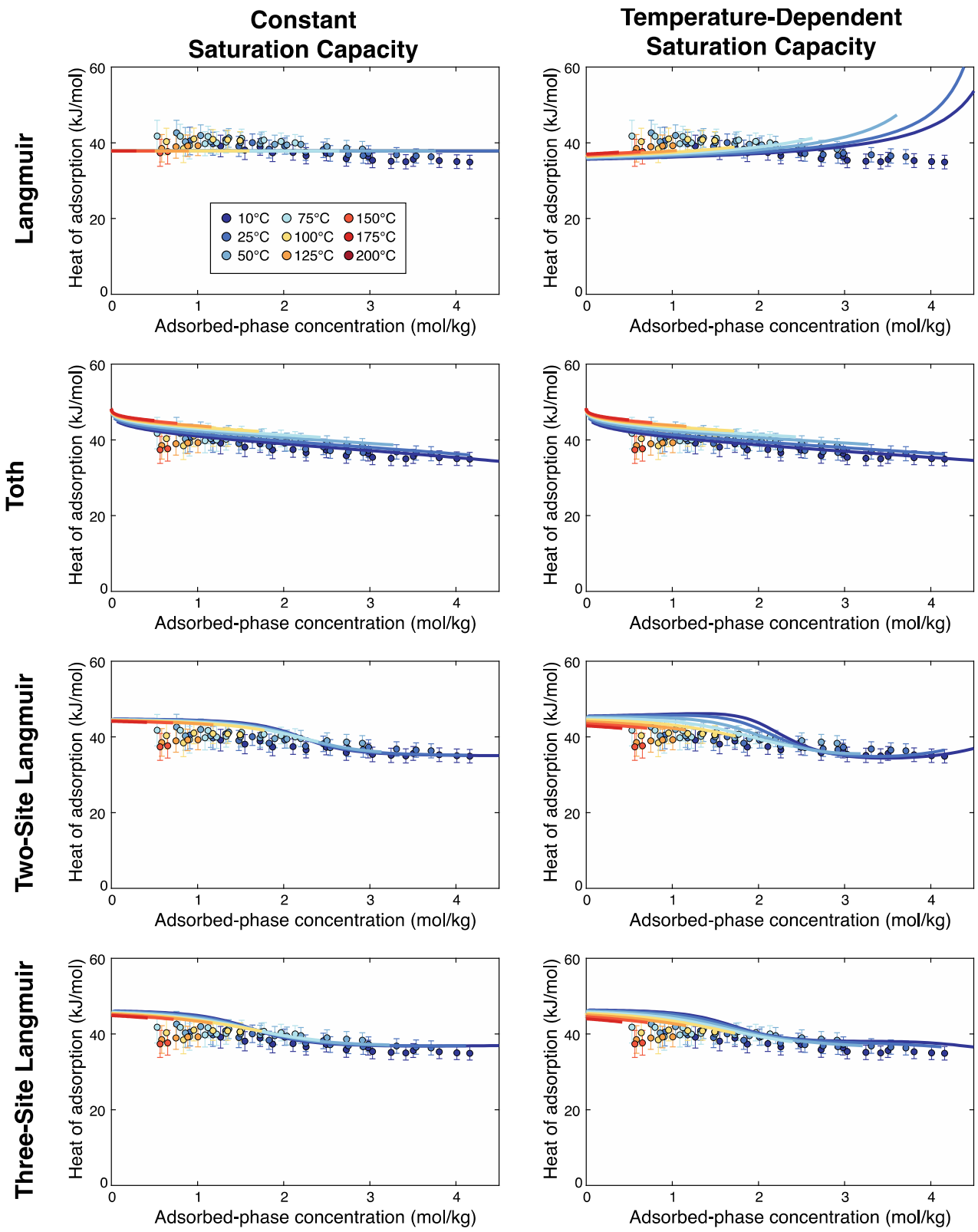

Figure 3.6. Heat of adsorption for CO_2 on zeolite 13X as a function of loading for temperatures of 10 °C to 200 °C. Experimental measurements are shown as symbols and predictions from the isotherm models are shown as lines.

the measured data, while the slightly more complicated Langmuir model with a temperature-dependent saturation capacity grossly overpredicts the λ at high loadings. The sharp rise in the heat of adsorption for this model at higher loadings is caused by the flattening out of the isotherms at high pressures (see Figure 3.4) since the heat of adsorption is proportional to $(\partial n/\partial p)^{-1}$. This illustrates the importance of matching the slope of a measured isotherm when fitting an isotherm model.

Heat of adsorption predictions based on the fitted Toth models provide the closest agreement with the measured data; note that the predicted λ is similar for both the constant and the temperature-dependent saturation coefficient Toth models due to the weak temperature dependence of the fitted a in the latter. Furthermore, the Toth models are the only isotherm models that correctly match the slope of the λ as loading increases. This implies that the formulation of the Toth isotherm model accurately describes the phenomena of CO_2 adsorption on 13X. This can be attributed to the heterogeneity parameter which accounts for a continuous distribution of sites to which CO_2 can adsorb, each with unique activation energy. This continuous distribution results in a steady decline and is distinct from the behavior of multisite Langmuir models, where the material is modeled as having a discrete number of homogenous sites, each of different energies. In other words, the multisite Langmuir model describes a surface with quantized adsorption energy

Predictions based on the more complex 2- and 3-site Langmuir models are of the same magnitude as the measured data and show a decreasing trend with increasing loading, but show nonphysical inflections around 2 mol/kg. These inflections are an artifact of the quantized adsorption energies. Such distinct changes in λ are experimentally observed for zeolites with patchy surfaces (*e.g.*, physical defects which strongly interact with the first monolayer of adsorbate at a higher energy [74]). The inflections predicted by the multisite Langmuir models, however, are not in agreement with our experimental λ measurements. This indicates that our surface comprises a continuous distribution of different-energy sites rather than a number of discrete sites. We also note that the nonphysical inflections are exacerbated in the version of these models with temperature-dependent saturation capacity; this implies that the models with temperature-dependent saturation capacity provided a better fit to the measured isotherms purely because it provides another fitting parameter, and not because the saturation capacity is physically a function of temperature. Hence, we

recommend against using a temperature-dependent saturation coefficient, due to the resulting poor prediction of λ. We furthermore conclude that while the Toth isotherm provides the best prediction of λ, the heat of adsorption is well approximated by a constant value across a wide range of loadings.

3.5 Conclusions

Isotherms for CO_2 adsorption on commercially available zeolite 13X (Grace Davidson MS544-13X), taken at ten temperatures from 0 °C to 200 °C and at pressures from 0.001 kPa to 100 kPa, were analyzed to determine the best-fit isotherm model. The 2-site Langmuir model with constant saturation coefficient (commonly known as the dual-site Langmuir) provides the best agreement with measured isotherms. Heats of adsorption were also measured at nine temperatures from 10 °C to 200 °C using a TG-DSC. These measurements were compared with predictions of the heats of adsorption based on the fitted isotherm models. This comparison of the predicted heat of adsorption to measured values supports our recommendation to use a constant saturation coefficient. We furthermore conclude that while the Toth isotherm provides the best prediction of the heat of adsorption, it can be approximated as constant across a wide range of loadings. The heat of adsorption is not a strong function of temperature for CO_2 on zeolite 13X.

4. EQUILIBRIUM ADSORPTION ISOTHERMS FOR H_2O ON ZEOLITE 13X

This chapter reports isotherm data from NASA Ames Research Center for H_2O adsorption on zeolite 13X (Grace Davidson, MS-544HP-13X) over a pressure range of 0.006 kPa to 25 kPa and a temperature range of 25 °C to 100 °C. Data were carefully collected to eliminate sources of bias in previous data given by Wang and LeVan [57], where incomplete activation resulted in a reduced capacity. We correlate the measured equilibrium data using the Aranovich–Donohue (A–D) model with four different isotherm equations (Sips, Toth, 2-site Langmuir, and 3-site Langmuir). The goodness of fit for each correlation is described in terms of several statistical metrics; this A–D Sips model is recommended for use based on its fit to the experimental data and simplicity.

The material presented in this chapter is currently under review [139].

4.1 Experimental methods

Isotherms for water adsorption on zeolite 13X are measured at 25 °C, 35 °C, 50 °C, 70 °C, and 100 °C and at equilibrium pressures ranging from 0.006 kPa to 25 kPa. All isotherms were collected at NASA Ames Research Center using a vacuum gravimetric sorption analyzer.

4.1.1 Materials

The adsorbent material used for isotherm is a commercial zeolite 13X (Grace Davison, MS 544). The adsorbent is characterized in the manufactured form as pelletized, spherical beads with a mean diameter of 2 mm which contain 18% binder on a dry weight basis. Deionized water (Millipore Milli-Academic, 18.2 MΩ) is used as the adsorbate. Note that zeolite 13X is extensively used in current NASA systems for life support and that MS 544 is the primary zeolite 13X candidate for next-generation adsorbent-based, life-support systems [8].

4.1.2 Sample preparation and activation

The zeolite 13X adsorbent is carefully activated prior to measuring the equilibrium adsorption capacity to ensure complete removal of water and other adsorbed constituents. First, ~30 mg of adsorbent (4–5 beads) is placed into the sample pan. The zeolite 13X is activated by heating the

sample *in situ* with the internal preheater to 350 °C (at 1.8 °C/min) and holding it at this temperature under vacuum (< 0.01 mTorr) for 4 h. This high activation temperature is necessary to remove all residual water from the adsorbent pores; lower activation temperatures (≤ 300 °C) were found to provide inconsistent results that were attributed to incomplete desorption of water affecting the measured capacity of other sorbates [129]. After the sample activation is complete, the sample is slowly cooled under vacuum to the desired temperature for isotherm measurements.

4.1.3 Measurement procedure

An automated gravimetric method is used to measure loading at a single temperature (isotherm) across a range of water vapor pressures. These isotherms are measured in a vacuum gravimetric sorption analyzer (Surface Measurement Systems, DVS Vacuum) [140]. This instrument is comprised of a microbalance in a vacuum chamber that holds the adsorbent sample, a flask of liquid water and flow controls to provide adsorbate gas to the sample, instrumentation, vacuum pumps, and a thermal chamber (see Figure 4.1). The thermal chamber houses most of these components—including the vacuum chamber and water flask—and sets the temperature of both the vapor-generation system and the adsorbent sample to within 0.1 °C. The thermal chamber serves to both prevent condensation and to provide a stable, accurate environment for measurement. Isotherm measurements are made using the *dynamic* measurement mode [140] of the DVS Vacuum sorption analyzer. In this mode, a continuous flow of water vapor is provided to the vacuum chamber throughout adsorption while constant pressure is maintained via a butterfly valve that meters the vacuum conductance. The DSV Vacuum sorption analyzer can measure isotherms in a temperature range of 20 °C to 70 °C within a relative humidity range 0.05% to 90% RH. Higher temperature isotherms can be measured, but only under a reduced relative humidity range. This is due to the maximum temperature of the thermal control chamber (70 °C) which limits the source water vapor pressure to approximately 28.2 kPa (*i.e.*, 90% of the saturated vapor pressure of water at 70 °C). The 100 °C isotherm is obtained using the preheater to maintain the adsorbent at 100 °C while the ambient chamber is held at 70 °C. This is the same preheater used during activation which can control the temperature of the sample chamber to within ± 1.0 °C.

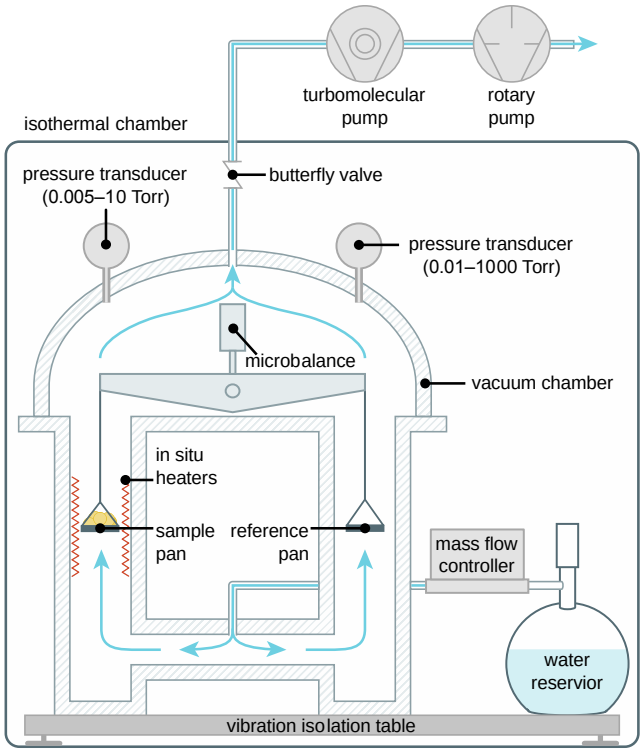

Figure 4.1. Schematic diagram of the Vacuum Dynamic Vapor Sorption (Surface Measurement Systems, DVS Vacuum) instrument [140] used to measure H_2O adsorption isotherms on zeolite 13X pellets.

To generate a desired water vapor concentration, water vapor inside the side-arm flask flows through a mass flow controller (Figure 4.1). The flask contains a two-phase mixture of liquid and vapor water at thermodynamic equilibrium with the temperature of the thermal chamber. Water vapor flow from the flask is induced by a low pressure in the vacuum chamber which pulls the vapor through the side-arm flask and up over the sample. Two vacuum pumps and a butterfly valve in series maintain this constant, subambient pressure in the vacuum manifold while the water vapor flow rate is independently controlled via a flow controller throughout adsorption. The butterfly valve maintains the desired pressure inside the vacuum chamber by adjusting the opening size in a feedback loop with the pressure transducers while changes in sample mass are simultaneously measured (Surface Measurement Systems, Ultrabalance™, 1–1000 mg full-scale range, 0.1 µg precision). This set-up allows for water vapor pressures within the vacuum chamber to reach approximately 90% of the saturated vapor pressure of the flask (*i.e.*, the saturated vapor pressure at the thermal chamber's temperature). Two pressure transducers (MKS Instruments, Baratron® transducers, 0.01–1000 Torr and 0.005–10 Torr full-scale ranges, ± 0.5% reading accuracy, 0.01%

FS resolution) continuously measure the pressure inside the vacuum chamber. The water vapor pressure is held constant until the adsorbent reaches equilibrium with the gas stream (dm/dt < 0.006%/min).

Further measurements are taken at successively higher concentrations of water vapor obtained by increasing the pressure within the chamber while maintaining the same total flow rate. This process of increasing the H_2O concentration, equilibrating the sample, and recording the change in mass is repeated to obtain the equilibrium concentration of H_2O at many partial pressures for a single isotherm. This entire process was repeated to obtain isotherms at five different temperatures between 25 °C and 100 °C.

4.2 Isotherm models

Per the International Union of Pure and Applied Chemistry (IUPAC) classification of gas-solid adsorption isotherms [130], the experimental isotherms obtained are of type II because they exhibit a sigmoidal shape with an apparent divergence of n to infinity as the water vapor partial pressure, p, approaches the water-vapor saturation pressure, p_{sat}. Type II isotherms are observed for materials with a range of pore sizes; there is initially monolayer adsorption within the microporous solid at lower H_2O partial pressures, followed by multilayer adsorption and then capillary condensation [141], [142]. The divergence of capacity at high p/p_{sat} values is caused by capillary condensation occurring in pores of increasing diameter [142] (*e.g.*, the macropores formed by the clay binder in the zeolite pellets [143]). Aranovich and Donohue [144] proposed the following model to account for the singularity at $p = p_{sat}$,

$$n = \frac{f\left(p,T\right)}{\left(1-p/p_{sat}\right)^{d}} \tag{4.1}$$

where n is the equilibrium adsorbed-phase concentration, T is the temperature of the adsorbent (*e.g.*, zeolite 13X), where $f(p)$ is a function describing the adsorption of the first molecular layer, d is an adjustable parameter, and p_{sat} is the saturation-vapor pressure as calculated by the Antoine equation [145],

$$p_{sat}(T) = 100\times 10^{4.6543-\frac{1435.264}{T-64.848}} \tag{4.2}$$

The function $f(p,T)$ can be expressed using several equilibrium adsorption isotherm models. In the present work, we consider four isotherm models for $f(p,T)$, including the Sips model [146],

$$f\left(p,T\right)=\frac{a\left(bp\right)^{1/h}}{1+\left(bp\right)^{1/h}} \tag{4.3}$$

Toth model [95],

$$f\left(p,T\right)=\frac{abp}{\left[1+\left(bp\right)^{h}\right]^{1/h}} \tag{4.4}$$

and multisite (*i.e.*, *k*-site) Langmuir model [124], [132],

$$f\left(p,T\right)=\sum_{j=1}^{k}\frac{a_j b_j p}{1+b_j p} \tag{4.5}$$

where a_0 is the saturation capacity, b is the temperature-dependent equilibrium constant,

$$b_j=b_{0,j}\exp\left[E_j/\left(RT_s\right)\right] \tag{4.6}$$

and h describes the surface heterogeneity. The parameters a, b_0, E, h, and d, are system-dependent, adsorption-isotherm parameters which we fit to the experimental data.

4.2.1 Fitting method

Isotherms are fit using the same method described in Section 3.2.4 and restated here. This method uses a custom implementation of the Generalized Reduced Gradient (GRG) nonlinear solver in Excel to find the parameters which minimized the sum of squares error, *SSE*, defined as

$$SSE=\sum\left(n_{\text{pred}}-n_{\text{meas}}\right)^2 \tag{4.7}$$

where n_{meas} is the measured amount adsorbed and n_{pred} is the predicted amount adsorbed based on the isotherm model and fit parameters. The *SSE* is found by summing over all experimental measurements; thus, regions of data with higher pressures and lower temperatures having larger absolute values of n_{meas} and n_{pred} will lead to higher absolute differences and will be emphasized more in the resulting fit. The GRG nonlinear solver converges to a residual of 1×10^{-12}. To improve convergence and prevent ill-conditioning, the parameters actively modified by the solver are normalized to be of the same order of magnitude every 1000 iterations. This is done by dividing the actual model fit parameters by their order of magnitude to obtain a value of ~1.

4.3 Results and discussion

Isotherms for water adsorption on zeolite 13X (Grace Davidson, MS 544) were measured at 25 °C, 35 °C, 50 °C, 70 °C, and 100 °C and at equilibrium pressures ranging from 0.006 kPa to 25 kPa or from relative humidities of 0.05% to 90%. The experimental adsorption equilibrium data are presented in Appendix C. The uncertainty in the pressure reading is ± 0.5% of the measured pressure. The uncertainty in measured loading is determined using the root sum of the squares method accounting for the microbalance accuracy (±0.3 μg). The experimental adsorption equilibrium data obtained in the present work are compared with H_2O/13X adsorption data from the literature. The present data are then correlated with the Aranovich–Donohue (A–D) Sips, Toth, and multisite Langmuir models. The resulting goodness of fits are then compared between models and recommendations are made for which model to use.

4.3.1 Comparison of isotherm data to the literature

Experimental data for water isotherms on zeolite 13X are collected from the literature along with details on the adsorbent, activation procedure, and measurement technique where available. Table 4.1 summarizes the adsorption isotherms extracted from the literature ([53], [57], [142], [147]–[158]); studies with isotherms which were found to be inconsistent either in shape (*e.g.*, crossing isotherms or negative slopes) or magnitude (*i.e.*, loading >50% discrepancy from the cluster of other isotherms) are excluded from this list. To allow for direct comparison between pure, crystalline samples and pelletized adsorbents, we normalize the reported loading as

$$n^* = \frac{n}{1-(\text{binder mass fraction})}. \tag{4.8}$$

Where a study does not explicitly state the binder's mass fraction, the binder mass fraction must be assumed. The commercial adsorbents used in Ryu *et al.* [147], Kim *et al.* [148], Ahn and Lee [142], Li *et al.* [152], and Ferreira *et al.* [153] are estimated to contain 20% binder by mass to make their measured loadings consistent with studies of crystalline 13X or pellets with a known binder mass fraction. The lab-made adsorbent in Zhu *et al.* [151] is estimated to contain 15% binder mass fraction following the same approach. This is the same method for estimating binder mass fraction used by Loughlin *et al.* [159] in their review of isotherms for multiatomic species on zeolites. All data plotted in Figure 4.2 to Figure 4.4 are normalized using Eq. 4.8 and the binder mass fractions listed in Table 4.1.

Table 4.1. Summary of the water vapor isotherms collected from the literature. A dash (-) in the binder column indicates pure crystalline samples were used (*i.e.*, no binder). Isotherms which exhibited a higher capacity are highlighted in green.

Authors	Year	Adsorbent Description	Binder	Activation	Measurement Technique	*T*, °C
Chuikina, *et al.* [149]	1976	lab-made	-	400 °C for 100 h (unspecified atmosphere)	calorimetric-volumetric	23, 100
Gopal, *et al.* [150]	1982	Linde powder	-	300 °C in ambient air for 24 h	N/A	25
Zhu, *et al.* [151]	1992	lab-made pellets	15%*	N/A	N/A	40, 60, 80, 100
Ryu, *et al.* [147]	2001	Aldrich pellets	20%*	340 °C for 7 h (unspecified atmosphere)	gravimetric	25, 35, 45
Kim, *et al.* [148]	2003	Aldrich pellets	20%*	320 °C in vacuum (10^{-3} Pa) for 24 h	volumetric (ASAP 2010, Micromeritics)	20, 40 ,60, 80
Ahn & Lee [142]	2004	Aldrich pellets	20%*	320 °C for 12 h (unspecified atmosphere)	N/A	25, 35, 45
Li, *et al.* [152]	2009	MOLSIV, UOP	20%*	320 °C (unspecified atmosphere and *t*)	gravimetric (IGA-002, Hiden Isochema, Ltd.)	25
Wang & LeVan [57]	2009	MS 544, Grace Davidson	18%	175 °C in vacuum overnight	volumetric	0–100
Ferreira, *et al.* [153]	2011	ZEOX OII pellets, Zeochem	20%*	375 °C in N_2 atmosphere for 6 h	gravimetric (Rubotherm)	35
		Z10-02ND pellets, Zeochem	20%*	375 °C in N_2 atmosphere for 6 h	gravimetric (Rubotherm)	35
Chen, *et al.* [154]	2012	Nanjing Inorganic Chemical Plant	-	450 °C for 2 h (unspecified atmosphere)	vacuum-gravimetric	25
Hefti, *et al.* [155]	2014	ZeoChem	20%	400 °C in vacuum for 4 h	gravimetric	45
Mette, *et al.* [156]	2014	13XBFK, Chemiewerk	-	350 °C in vacuum, $<10^{-5}$ mbar (unspecified *t*)	gravimetric (IGA-002, Hiden Isochema, Ltd.)	25–250
Kim, *et al.* [53]	2016	APG MOLSIV, UOP	20%	300 °C in vacuum for 12 h	volumetric (ASIQM0 V000-4, Quantachrome)	20, 30, 40
Lehmann, *et al.* [157]	2017	13XBFK, Chemiewerk	-	400 °C in vacuum, <0.05 Pa, for 16 h	gravimetric (IGA-002, Hiden Isochema, Ltd.)	31–250
Semprini, *et al.* [158]	2017	13XBFK, Chemiewerk	-	350 °C in vacuum, $<10^{-5}$ mbar (unspecified *t*)	gravimetric (IGA-002, Hiden Isochema, Ltd.)	25–250

*Estimated binder mass fraction.

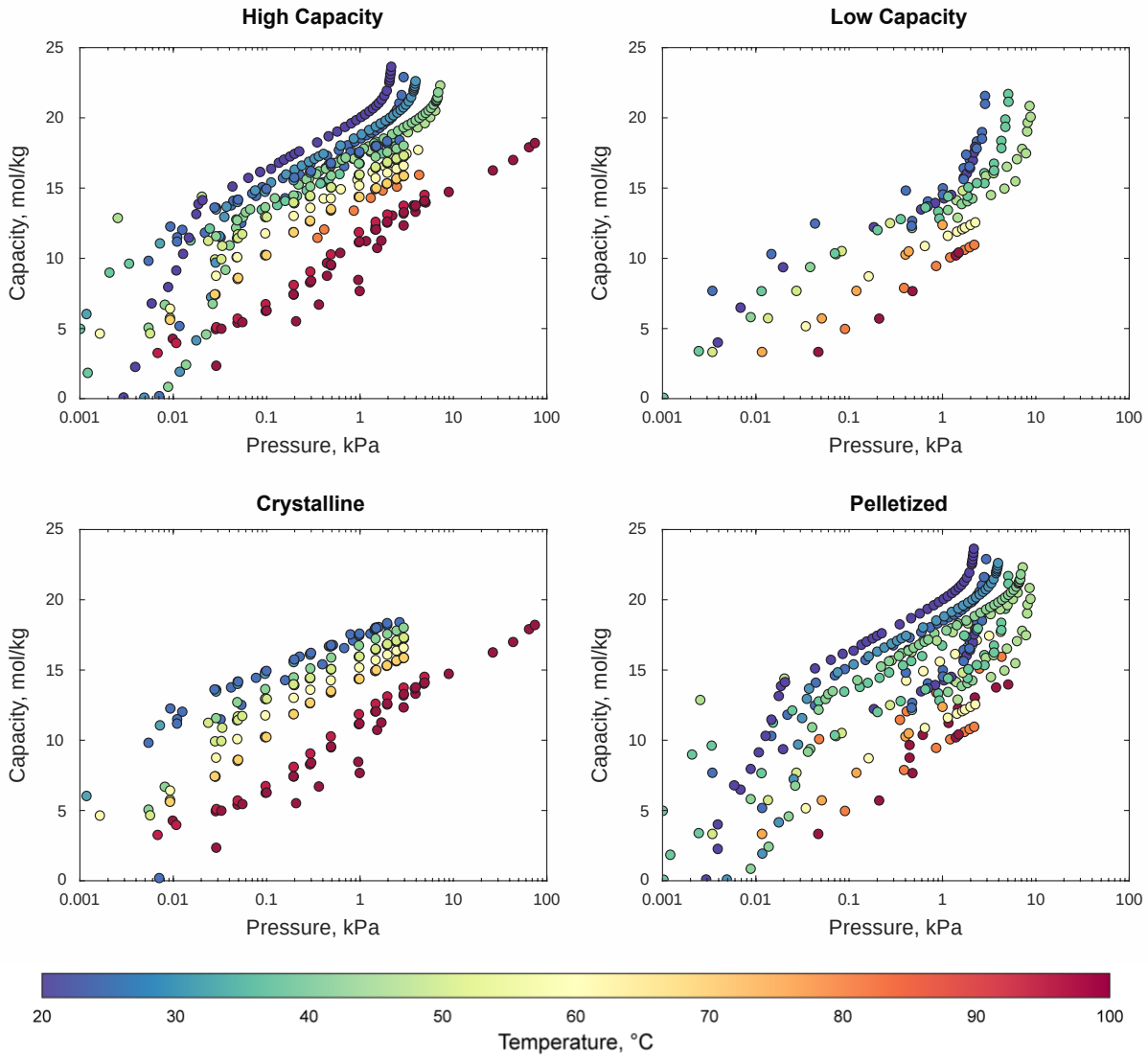

Figure 4.2. Water on zeolite 13X isotherms from the literature [53], [57], [142], [147]–[158]. The isotherms are grouped based on the adsorbent's capacity (top panels); most of the isotherms [53], [149]–[158] exhibit a high capacity for water (left), while a few ([57], [142], [147], [148], [153]) isotherms show a lower capacity (right). Isotherms are also grouped by adsorbent type (bottom panels), being either crystalline [149], [150], [154], [156]–[158] (left) or pelletized [53], [57], [142], [147], [148], [151]–[153], [155] (right).

The studies listed in Table 4.1 can be divided into two groups based on their capacity for H_2O adsorption. Most of the studies showed a similar, high capacity of approximately 18.5 mol/kg at 1 kPa of water vapor and 25 °C. These high-capacity isotherms are plotted in the upper left panel of Figure 4.2 and are highlighted in green in Table 4.1. Isotherms from remaining five studies—which show a significantly lower capacity of ~15 mol/kg at 1 kPa of water vapor and 25 °C—are plotted in the upper right panel of Figure 4.2. Ferreira *et al.* [153] measured isotherms for two different commercial 13X samples, Z10-02ND and ZEOX O_{II} (Zeochem). The first adsorbent, Z10-02ND, exhibited high water capacity and is plotted in the upper left panel of Figure 4.2 while the second adsorbent, ZEOX O_{II}, is grouped with the low-capacity isotherms in the upper right panel. We attribute this difference in capacity for these two Zeochem adsorbents to differences in their formulations. All three studies on Aldrich pellets consistently exhibited low-capacity isotherms compared to the bulk of isotherms from the literature, indicating a difference in pellet formulation which yields capacity similar to ZEOX O_{II}. We attribute the low-capacity isotherms from the final study [57] to incomplete activation caused by inadequate activation temperature.

Through extensive comparison of CO_2 isotherms on zeolite 13X from four separate research facilities (NASA Marshall, NASA Ames, University of South Carolina, and Vanderbilt University) NASA found that activation at lower temperatures (*e.g.*, 300 °C) caused incomplete desorption of water and resulted in discrepancies between different isotherm measurements [58]. All discrepancies between the different research facilities and measurement techniques (*e.g.*, gravimetric versus volumetric) were resolved by using an activation temperature of 350 °C. NASA's results confirm the findings of Brandani and Ruthven [59] who found that zeolite 13X needed to be activated at 350 °C to completely remove H_2O. In their study, Wang and LeVan [57] used the same adsorbent (Grace Davidson, MS 544) as the present work, however, they used a much lower activation temperature (175 °C). Based on our previous findings, we expected that these H_2O/13X isotherm data would be biased due to residual water loading. This theory is confirmed by comparing the isotherms of Wang and LeVan [57] to the current data (see Figure 4.3). The values reported by Wang and LeVan [57] are consistently lower by 1 mol/kg to 2 mol/kg with the largest discrepancies seen in the lowest temperature isotherms and in the low-pressure region. These results clearly show that a high activation temperature (*e.g.*, 350 °C) is required to obtain accurate water isotherm data.

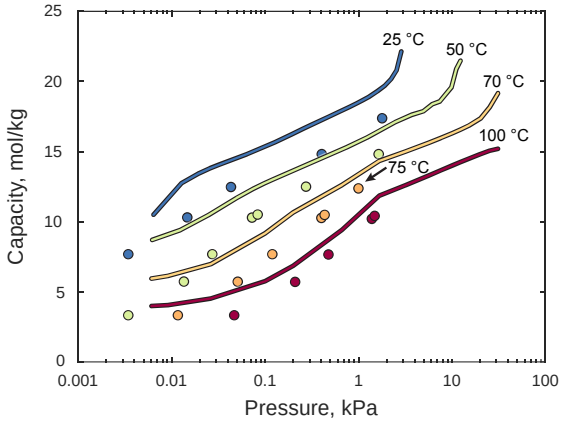

Figure 4.3. Comparison of isotherms for H_2O on zeolite 13X from current work (lines) to values from Wang and LeVan [57] (circles).

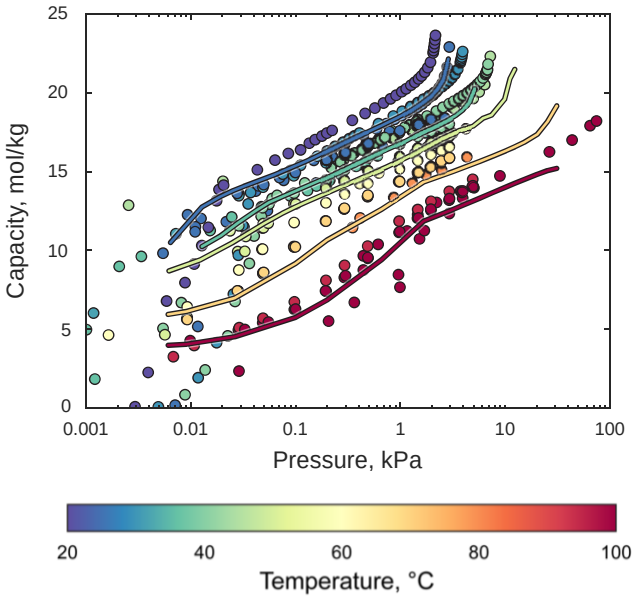

Figure 4.4. Comparison of isotherms for H_2O on zeolite 13X from current work (lines) to values from the literature [53], [149]–[158].

In addition to grouping isotherms based on capacity, isotherms from the literature can be grouped based on the type of adsorbent used in their measurements (*i.e.*, pelletized or crystalline) as shown in the bottom panels of Figure 4.2. Isotherms measured on pelletized adsorbents (right) showed different behavior than those measured on pure crystals (left) at high pressures. In pelletized adsorbents, the loading rapidly increases as the water vapor partial pressure approaches the saturation pressure, causing condensation within the mesopores and macropores of the pellets [142]. Because the isotherms obtained from the crystalline adsorbents do not extend into the region where the effects of binder are evident (*i.e.*, high pressures where macropore condensation occurs [16]), they can be directly compared with isotherms from pelletized adsorbents. As such, we retain data for crystalline adsorbents when comparing our measurements to isotherms from the literature.

A comparison of the current isotherm results for water adsorption on zeolite 13X to data from the literature ([53], [149]–[158]) is presented in Figure 4.4, which shows the equilibrium capacity of zeolite 13X as a function of H_2O pressure. Isotherm data measured on Aldrich and Zeochem ZEOX O_{II} adsorbents are excluded due to differences in the zeolite formulations. The data of Wang and LeVan [57] are also excluded due to the low activation temperature which was insufficient to remove residual water loading. Our data match both the slope and general magnitude of the literature data. We note that there is some scatter amongst the isotherms from the literature which we attribute to differences in the adsorbents tested. This scatter emphasizes the importance of measuring isotherm data for the specific adsorbent formulation of interest to achieve maximum accuracy. Water and carbon dioxide [129] adsorption on Grace Davidson MS 544 is of particular interest as MS 544 was recently selected for use in NASA's next-generation life-support systems [8].

4.3.2 Comparison of isotherm data to fitted models

The isotherm models given in Eq 4.4 through Eq 4.5 are fit to our experimental data as described in Section 4.2.1, with the resulting fits shown in Figure 3.4. The accuracy of each model fit to the experimental data is quantified using the root-mean-square error (*RMSE*), the normalized-root-mean-square error (*NRMSE*), the maximum error (E_{max}), the normalized-maximum error (NE_{max}), and the regression coefficient (R^2) as given in Table 3.2. The Aranovich–Donohue (A–D) 2-site Langmuir model predictions deviate from the experimental measurements as shown in Figure 3.4,

with the model predictions falling outside of the 95% confidence interval of measured loading values at low vapor pressures for the 40 °C and 100 °C isotherms. The A–D 2-site Langmuir model also yields the worst values for each goodness-of-fit metric considered in Table 3.2. Comparing the remaining three models requires a closer look at the plotted comparisons in combination with the values in Table 3.2. For example, while the A–D 3-site Langmuir model appears to provide an excellent fit based on the *RMSE* and R^2 values (0.404 mol/kg and 0.985, respectively), but the plotted model predictions show nonphysical artifacts. Most notably, the predicted isotherms diverge from the theoretically expected Henry's law behavior at low vapor pressures [141]. Not only are these inflections thermodynamically inconsistent with H_2O adsorption on zeolite 13X, but they can also result in significant model errors if the Clausius–Clapeyron equation is used to predict the heat of adsorption [129]. These spurious fitting artifacts are caused by a larger number of free parameters (*i.e.*, overfitting). The A–D Sips model also fits the data very well (*RMSE* = 0.472 mol/kg, R^2 = 0.979), but has half the number of fitted parameters, which significantly reduces the risk of overfitting.

The *RMSE*, max error, and R^2 values do not provide a complete picture of the goodness of fit at low loadings because they are absolute measures of the error. Two additional *relative* error metrics are therefore considered to better quantify the goodness of fit at low loadings; the normalized-maximum error, $NE_{\max}$, and the normalized-root-mean-square error (*NRMSE*),

$$NRMSE = \sqrt{\frac{1}{k}\sum_{i=1}^{k}\left(\frac{\left(n_{\text{pred}} - n_{\text{meas}}\right)^2}{n_{\text{meas}}}\right)}. \tag{4.9}$$

These normalized metrics highlight the risks associated with overfitting data. Note that the multisite Langmuir models have almost double the normalized-maximum error as the much simpler Sips or Toth models. The normalized metrics also show that the A–D Sips model (*NRMSE* = 0.0492 and $NE_{\max}$ = 0.149) provides a slightly better fit than the A–D Toth model (*NRMSE* = 0.0497 and $NE_{\max}$ = 0.151). Based on these goodness-of-fit parameters, we recommend using the A–D Sips isotherm model as given by Eqs 4.1–4.3 with the fitted parameters listed in Table 4.3. Fit parameters for the other H_2O isotherm models are provided in Appendix D. The isotherms are only recommended for use within the bounds of the experimental measurements (*i.e.*, 0.006 kPa to 25 kPa and 20 °C to 100 °C) and for zeolite 13X with similar formulation to the tested adsorbent.

Table 4.2. Comparison of the goodness of fit for the different isotherm models.

Model	No. of fit parameters	*RMSE*, mol/kg	*NRMSE*	E_{max}, mol/kg	NE_{max}	R^2
A–D Sips	5	0.472	0.0492	1.31	0.149	0.979
A–D Toth	5	0.463	0.0497	1.21	0.151	0.979
A–D 2-site Langmuir	7	0.612	0.0616	1.88	0.260	0.965
A–D 3-site Langmuir	10	0.404	0.0411	1.47	0.206	0.985

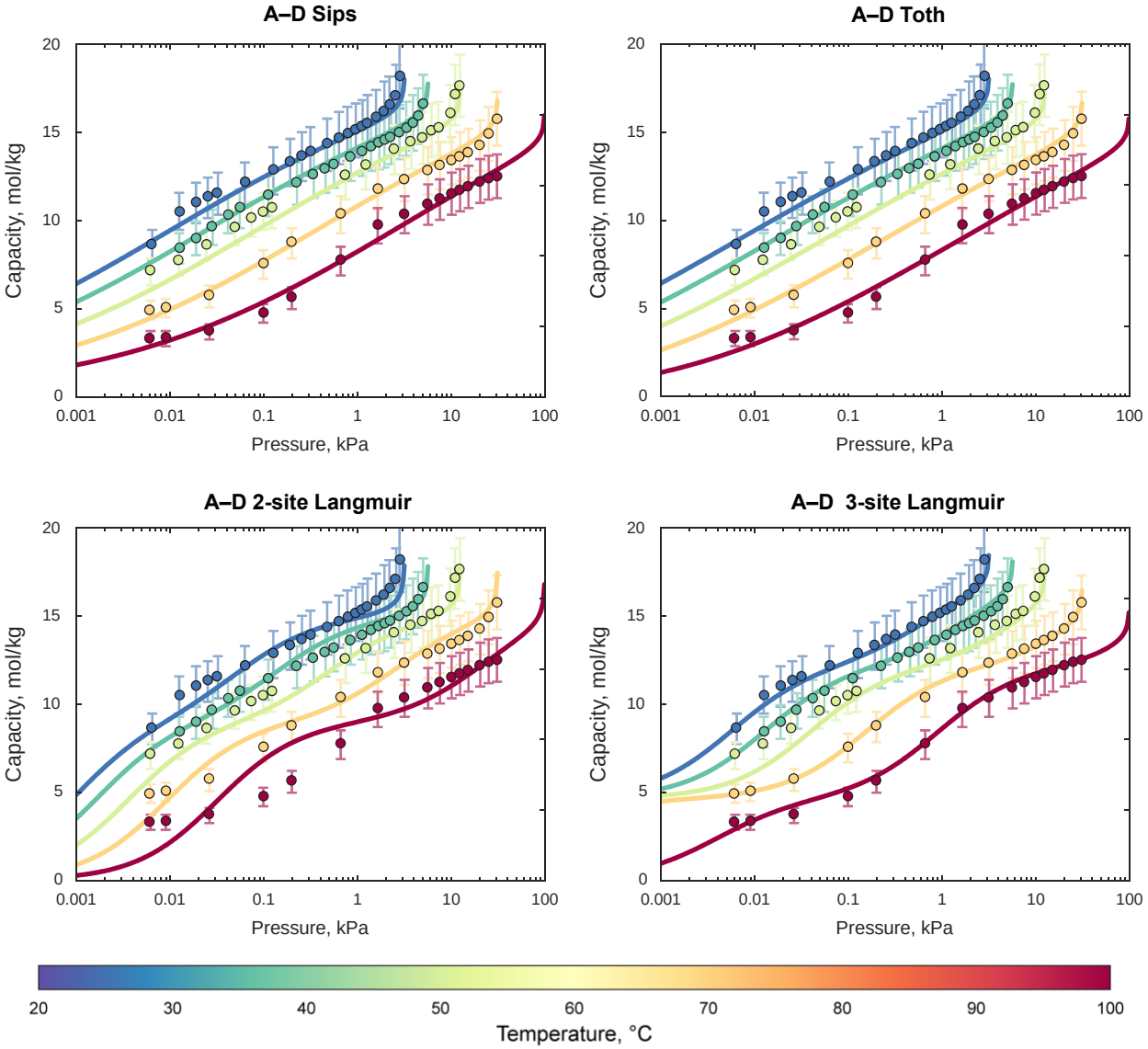

Figure 4.5. Measured isotherms from the current work (symbols) for H_2O adsorption on zeolite 13X compared to isotherm model predictions (lines).

4.4 Conclusions

Accurate isotherm fits are a critical component of predictive adsorption models; good isotherm fits depend on both precise measurements and appropriate selection of the equilibrium adsorption isotherm equation. Isotherms for H_2O adsorption on commercially available zeolite 13X (Grace Davidson MS 544), are measured at five temperatures from 25 °C to 100 °C and at pressures from 0.006 kPa to 25 kPa. Our measurements compare favorably to other isotherm measurements in the literature and show the importance of careful collection techniques. We specifically showed that a high activation temperature (350 °C) is needed to obtain accurate water isotherms by comparing against experimental results from the literature which showed a reduced capacity due to incomplete removal of water at a lower activation temperature (175 °C). We then fit the Sips, Toth, 2-site Langmuir, and 3-site Langmuir (all modified with the Aranovich–Donohue equation) to our experimental measurements to determine the isotherm model that offers the best representation of the measured data. From this comparison, we recommend using the A–D Sips isotherm model as given by Eqs 4.1–4.3 with the fitted parameters listed in Table 4.3 when modeling water adsorption on zeolite 13X. While the isotherm fit presented in this work was developed for modeling life-support systems, it can be broadly used in the design of numerous other adsorption systems such as gas stream dehumidification, industrial processes, and natural gas purification process.

Table 4.3. Fit parameters for the A–D Sips isotherm model for H_2O adsorption on zeolite 13X (Grace Davidson, MS 544).

a_0, mol/kg	b_0, kPa^{-1}	E/R, K	f_0	d
18.87	1.353×10^{-10}	8150	0.288	0.02772

5. LIMITATIONS OF THE AXIALLY DISPERSE PLUG-FLOW MODEL IN PREDICTING BREAKTHROUGH IN CONFINED GEOMETRIES

This chapter examines the ability of the axially disperse plug-flow model to accurately predict breakthrough in adsorbent beds confined by ridged walls. The axially disperse plug-flow model is used to independently extract mass transfer and axial-dispersion coefficients from breakthrough experiments via centerline and mixed-exit concentration measurements, respectively. Four experimental cases are considered: breakthrough of carbon dioxide (CO_2) and water (H_2O), in two cylindrical beds of zeolite 13X (NaX) each. The extracted axial-dispersion coefficients are compared to predictions from existing correlations which are ubiquitously used to predict mechanical dispersion in packed beds. We show that such correlations grossly underpredict the apparent axial dispersion observed in the bed because they do not account for the effects of wall channeling. The relative magnitudes of wall-channeling effects are shown to be a function of the adsorption/adsorbate pair and geometric confinement (*i.e.*, bed size). We show that the axially dispersed plug-flow model fails to capture the physics of breakthrough when nonplug-flow conditions prevail in the bed.

The material presented in this chapter is currently in preparation [160].

5.1 Experimental procedure

5.1.1 Description of the experimental facility

Adsorption breakthrough experiments are conducted in two adsorbent beds, installed in separate facilities having the same primary flow components and sensors; differences between the facilities are limited to the specific component sizes and sensor locations. Figure 5.1 shows the primary components of the facilities in a flow diagram. Each facility contains a fixed bed of zeolite 13X adsorbent (Grace Davidson MS544HP-13X, lot 1000216159) housed in a cylindrical canister. Table 5.1 summarizes the physical properties of the adsorbent from the manufacturer [81]. A system of flow controllers, a humidification loop, and a mixing chamber upstream of the bed provide a finely controlled flow of adsorbate/carrier gas to the sorbent bed. The facility is configured to use CO_2 or H_2O as the adsorbate in nitrogen carrier gas. The nitrogen carrier gas is

supplied by a facility N_2 line, and the CO_2 (99.99% purity) gas is supplied by Sexton Welding Supply Co. Both facilities use deionized water to humidify a flow of N_2 for the H_2O breakthrough tests. An in-line heater located immediately upstream of the bed maintains the inflow at a uniform temperature of 25 °C.

The gas composition is monitored at three locations during the breakthrough test. Sampling lines draw off a portion of the flow both upstream and downstream of the bed. These siphoned flows proceed through continuous-monitoring, infrared CO_2 analyzers (Sable Systems CA-10 CO_2 Analyzer, ±1% of reading accuracy over a range of 0–5% CO_2 by volume) and chilled mirror hydrometers (Edgetech, DewMaster X3SF, ±0.1 °C dew/frost point) before venting to the atmosphere. Because the downstream sampling line is installed more than a meter downstream of the bed, the flow is well-mixed. The concentration is also measured within the bed using a small sampling tube inserted into the bottom of the bed a few millimeters from the exit (see the inset in Figure 5.1). This tube redirects a portion of the flow from the centerline of the bed to a continuous-monitoring, infrared CO_2/H_2O analyzer (LICOR, LI-840, ±1% and ±1.5% of reading accuracy over a range of 0–2% CO_2 by volume and 0–60 mmol/mol for H_2O, respectively). A mass flow controller sets the flow rate through the centerline sampling tube such that the superficial velocity through the sampling tube is equal to the superficial velocity in the sorbent bed; this minimizes flow disturbance near the centerline tube. Total pressure is measured immediately upstream of the adsorbent bed in both facilities by an absolute pressure transducer (Honeywell FP2000, 2-172 kPa range and ±0.10% full-scale range uncertainty) throughout the breakthrough experiment.

There are two solenoid valves downstream of the bed in the large test stand which impose a significant pressure drop (~10 kPa) between the bed exit and the location where effluent vents to the atmosphere, leading to a higher pressure within the large-diameter bed than in the small-diameter bed. The mole fraction of adsorbate is adjusted to account for this difference in bed pressure such that experiments in both test stands have the same adsorbate partial pressures—approximately 0.3 kPa for CO_2 and 1.3 kPa for H_2O adsorption.

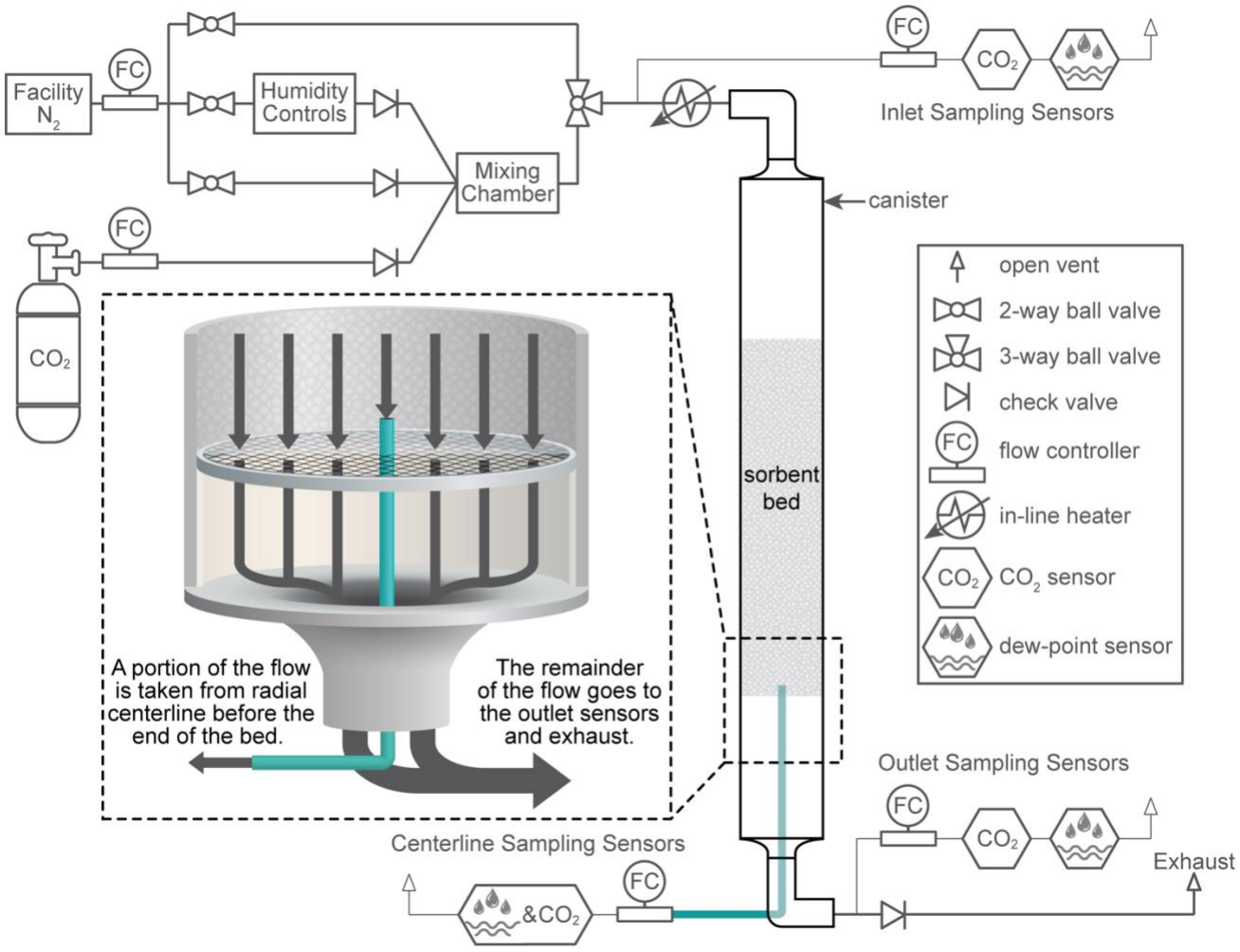

Figure 5.1. Schematic diagram of the experimental facility showing the flow paths and instrumentation. Note that the inlet and outlet gas sampling tubes are physically located far upstream and downstream respectively of the adsorbent bed.

Table 5.1. Thermophysical physical properties for Grace Davidson MS544-13X.

Property	Value
mean pellet diameter, d_p (mm)	2.0
conductivity, k_s (W/m-K)	0.15
heat capacity, $c_{p,s}$ (J/kg-K)	500
pellet envelope density, ρ_{env} (kg/m^3)	1054

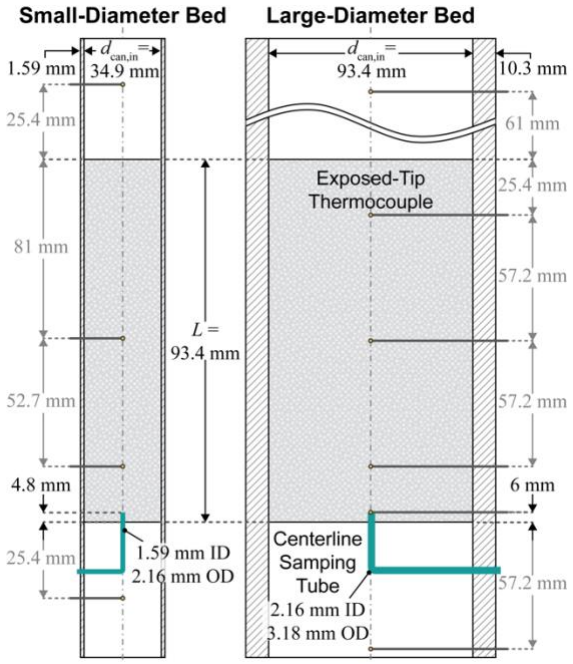

Figure 5.2. Cross-sectional views of the cylindrical canister and adsorbent bed for the small- and large-diameter test stands, showing the axial locations of intrabed thermocouples and centerline sampling tube. Note that all dimensions and locations are to scale.

Figure 5.2 shows dimensioned cross-sectional drawings of the aluminum (AL-6061) canisters which house the sorbent beds in the two experimental facilities, called the small-diameter and large-diameter test stands in this chapter. The first facility contains a canister that is 34.9 mm in diameter, or approximately 17 sorbent pellets across, and is insulated with 50.8 mm of Pyropel® LD-6 [85]. The second facility uses a much larger canister that holds approximately 48 pellets across its diameter ($d_{can,in}$ = 93.4 mm) and is insulated with 25.4 mm of Pyropel® LD-6. Exposed-tip thermocouples measure the gas-stream temperatures upstream and downstream of the bed, and along the centerline at multiple locations within the sorbent bed, as shown in Figure 5.2. All thermocouples are factory calibrated (T-type; ±1 °C accuracy).

The two facilities use different methods for humidifying the influent gas stream during H_2O breakthrough tests. The small-diameter test stand sparges N_2 through a temperature-controlled pool of water to humidify the gas; this humid stream then mixes with dry N_2 to achieve the desired dewpoint. The large-diameter test stand passes dry N_2 over a hollow-fiber, microporous membrane (EnerFuel, EFH-100WA), which allows humidification up to higher flow rates. The cross-flow of

N_2 picks up evaporating water on the gas side of the membrane while the liquid side of the membrane is continually replenished via internal capillaries of the hollow-fiber tubes. Water is supplied to the membrane from a reservoir maintained at a fixed temperature by a thermoelectric, liquid recirculating chiller (Solid State Cooling Systems, Thermocube 400, ±0.05 °C).

5.1.2 Sorbent activation and packing

The sorbent is activated in an oven at 350 °C for 15 h prior to packing the bed. During activation, a continuous stream of dry N_2 flows through the sorbent at a superficial velocity of ~0.25 m/s. The activated sorbent is moved to a dry-N_2 glove box (dew point ≤ -65 °C) where the cylindrical canister is then packed using the "snow-storm filling" method [161], [162]. This method involves pouring the sorbent over a pair of staggered wire screens which interrupt the flow of particles as they fall, causing radial dispersion of the particles. This radial dispersion reduces the possibility of particles segregating by size and results in uniform deposition across the entire cross-sectional area of the bed. To fill the bed, a beaker of sorbent is held against the rim of the snowstorm screen as the sorbent slowly poured through these screens into the canister, increasing the bed height at a rate between 0.5 and 5 mm/min to a total height of 165 mm (6.5 in).

After packing the bed, the canister is sealed and transported from the dry-N_2 glove box to the test stand. Installation of the canister is done with a constant flow of dry N_2 through the bed to prevent contamination by maintaining positive pressure in the canister. Installation takes ~2 min for the small canister and ~10 min for the large canister. Intrabed temperatures are monitored during this time to ensure that no ambient air entered the bed and caused water to adsorb on the sorbent, which would be detected as a noticeable temperature rise due to the high heat of adsorption.

5.1.3 Breakthrough experimental procedure

To perform breakthrough tests, the beds are initially filled with only N_2 and then exposed to an inlet flow of N_2 and adsorbate (either CO_2 or H_2O) at $t = 0$. The inlet flow is maintained at a constant superficial velocity and constant adsorbate concentration, while the outlet is maintained at a constant total pressure. The pellets adsorb CO_2 or H_2O as the gas mixture passes through the bed. Eventually, a small quantity of adsorbate begins to be detected in the bed effluent. The time at which this occurs is termed the initial breakthrough time, t_b. For this work, the breakthrough

time is defined as the time at which the effluent mole fraction first reaches 1% of the influent mole fraction, x_0. The test continues until the bed is completely saturated, *i.e.*, the effluent concentration matches the influent mole fraction to within 1%. Bed saturation occurs at the same time for both the small- and large-diameter beds—approximately t = 2 h for CO_2 and t = 6 h for H_2O—because the bed length and superficial velocity are the same for both stands.

Multiple CO_2 and H_2O breakthrough experiments are conducted to verify repeatability. The sorbent bed is activated in situ between repeated CO_2 breakthrough tests; in situ activation is carried out under a flow of dry N_2 at a superficial velocity of 0.3 m/s at 125 °C for ≥ 8 h and at 200 °C for ≥ 4 h for the large- and small- diameter test stands, respectively. Note that the in-situ activation temperature of the large-diameter test stand is limited by the proximity of temperature-sensitive pressure transducers to hot gases flowing through the bed. These activation procedures were selected after carefully testing to verify the resulting complete removal of CO_2 from the sorbent. In-situ activation between H_2O breakthrough tests is not possible in either test stand due to the strong affinity for H_2O of zeolite 13X, which requires heating up to 350 °C. Instead, after each H_2O breakthrough test, the sorbent is activated externally and repacked following the procedures in Section 5.1.2.

5.2 Modeling approach

An axially dispersed plug-flow model is used to model the breakthrough experiments described in Section 5.1.1. This quasi-one-dimensional model independently tracks the temperature of the separate constituents (gas phase, sorbent, and canister wall) using three energy balances. The model additionally requires two mass balances for the gas phase and adsorbed phase of the adsorbate (*i.e.*, CO_2 or H_2O). These five governing equations are coupled and solved to obtain the CO_2 or H_2O concentrations and temperatures as a function of time and axial position along the bed. This model is based on our prior work which analyzed the sensitivity [77] and uncertainty [78] of the axially dispersed plug-flow model, with a few distinctions. The present model omits the insulation energy balance and replaces it with an equivalent resistance. In addition, the current work uses different isotherms and an LDF definition appropriate for zeolite 13X which differs in equilibrium and kinetics from the zeolite 5A considered in our prior work.

5.2.1 Adsorbed-phase mass balance

The physical process of adsorption is controlled by several mass transfer resistances, including macropore, micropore, and surface diffusion. By neglecting the concentration gradient within a pellet and assuming that a single mass transfer resistance dominates, we can use the linear-driving-force (LDF) approximation [13] to express the adsorption rate as

$$\frac{\partial n}{\partial t} = k_l \left(n^* - n \right) \tag{5.1}$$

where n is the adsorbate concentration in the gas phase, n^* is the equilibrium adsorbed-phase concentration, and k_l is the LDF mass transfer coefficient. The LDF approximation is a physically consistent [163] model for fixed-bed adsorption that is frequently used due to its simplicity and accuracy [14]. When macropore diffusion is the rate-limiting mass-transfer step—as is the case for both CO_2 and H_2O adsorption on zeolite 13X [164], [165]—the LDF coefficient is inversely proportional to the equilibrium adsorbent-phase concentration,

$$k_l = \frac{k_0}{n^*} \tag{5.2}$$

where k_0 is a constant parameter that we will refer to as simply the mass transfer coefficient.

The equilibrium adsorbed-phase concentration, n^*, depends on the adsorbate partial pressure and the sorbent temperature. We use the isotherms developed in Chapter 3 and 4 for CO_2 and H_2O adsorption respectively. The bed is assumed to be initially devoid of CO_2/H_2O (*i.e.*, $n(t = 0) = 0$) and the simulation runs until the bed is saturated with adsorbate.

5.2.2 Gas-phase mass balance

The gas-phase mass balance is coupled with the adsorbed-phase mass balance via the rate of adsorption. This balance also accounts for advection and axial dispersion through the bed as

$$\frac{\partial c}{\partial t} + \left(\frac{1-\varepsilon}{\varepsilon} \right) \frac{\partial n}{\partial t} - D_{\text{ax}} \frac{\partial^2 c}{\partial z^2} = -\frac{\partial (u_i c)}{\partial z} \tag{5.3}$$

where c is the gas-phase concentration of the adsorbate (*i.e.*, CO_2 or H_2O). The axial-dispersion coefficient, D_{ax}, is either calculated from the parametric equation of Edwards and Richardson [86] to estimate the pellet-driven dispersion or extracted from mixed-exit breakthrough curves to estimate the apparent dispersion, as described in the Section 5.3. We represent the experimental

boundary conditions in our model with the commonly used Danckwerts boundary conditions defined as

$$-D_{\text{ax}}\left.\frac{\partial c}{\partial z}\right|_{z=0^+} = \frac{u_\infty}{\varepsilon}\left(c_\infty - c\big|_{z=0^+}\right) \quad \text{and} \quad \left.\frac{\partial c}{\partial z}\right|_{z=L} = 0\,. \qquad 5.4,\ 5.5$$

5.2.3 Energy balances

Separate energy balance equations for the gas, adsorbent, and canister wall are included in the model to account for local thermal nonequilibrium. All three energy balances account for transient heat storage and heat transfer between the separate regions. The gas-phase energy balance also accounts for axial advection and axial conduction,

$$\varepsilon A_{\text{fr}}\rho_{\text{g}}c_{p,\text{g}}\frac{\partial T_{\text{g}}}{\partial t} = \varepsilon A_{\text{fr}}k_{\text{eff}}\frac{\partial^2 T_{\text{g}}}{\partial z^2} - A_{\text{fr}}\rho_{\text{g}}c_{p,\text{g}}u_\infty\frac{\partial T_{\text{g}}}{\partial z} + A_{\text{fr}}\frac{A_{\text{s}}}{V_{\text{bed}}}h_{\text{g–s}}\left(T_{\text{s}} - T_{\text{g}}\right) + \pi d_{\text{can,in}}h_{\text{g–can}}\left(T_{\text{can}} - T_{\text{g}}\right) \qquad 5.6$$

where A_{fr} is the free-flow area, *i.e.*, the cross-sectional area of an empty canister. The interfacial gas-sorbent heat transfer coefficient, $h_{\text{g–s}}$, is predicted from the empirical correlation of Wakao *et al.* [88] and the heat transfer coefficient between the gas and inner canister wall, $h_{\text{g–can}}$, is predicted using the empirical correlation from Li and Finlayson [89]. The effective axial thermal conductivity, k_{eff}, is calculated using the correlation of Yagi *et al.* [90] which accounts for both the sorbent- and gas-phase conductivities as well as axial mixing. All these input parameters are calculated using the dimensionless Reynolds, Prandtl, Schmidt, and Peclet numbers as defined in the *Nomenclature* section.

The sorbent-phase energy balance accounts for transient storage, convective heat loss to the gas, and the heat of adsorption, but neglects axial conduction, as the gas-phase energy balance already accounts for the sorbent bed conductivity,

$$A_{\text{fr}}\left(1-\varepsilon\right)\rho_{\text{env}}c_{p,\text{s}}\frac{\partial T_{\text{s}}}{\partial t} = A_{\text{fr}}\frac{A_{\text{s}}}{V_{\text{bed}}}h_{\text{g–s}}\left(T_{\text{g}} - T_{\text{s}}\right) - \left(1-\varepsilon\right)A_{\text{fr}}\lambda\frac{\partial n}{\partial t}\,. \qquad 5.7$$

The isosteric heat of adsorption, λ, is derived as a function of adsorbate partial pressure and sorbent temperature using the Clausius−Clapeyron relationship [129].

The canister wall energy balance, accounts for transient energy storage, axial conduction, and heat transfer with the neighboring phases as

$$A_{\text{can}}\rho_{\text{can}}c_{p,\text{can}}\frac{\partial T_{\text{can}}}{\partial t}-A_{\text{can}}k_{\text{can}}\frac{\partial^2 T_{\text{can}}}{\partial z^2}=\pi d_{\text{can,in}}h_{\text{g–can}}\left(T_{\text{g}}-T_{\text{can}}\right)+\frac{1}{R'_{\text{can–amb}}}\left(T_{\text{amb}}-T_{\text{can}}\right). \qquad 5.8$$

$R'_{\text{can–amb}}$ represents the combined thermal resistance of the canister–insulation interface, conduction resistance across the insulation, and convection from the outside of the insulation to ambient air. These resistances are lumped together to combine several unknown/uncertain parameters (*e.g.*, $h_{\text{ins–amb}}$ and k_{ins}) into a single thermal resistance which we directly calibrate to each test stand as described in Appendix F. From this calibration, $R'_{\text{can–amb}}$ is found to be 2.04 K/(m W) and 3.82 K/(m W) for the small- and large-diameter test stands, respectively.

We use experimentally measured temperatures to set the initial temperatures of all three constituents. The test stand was at thermal equilibrium prior to the start of the test and initial temperatures were taken as the average of all thermocouples shown in Figure 5.2. The inlet gas temperature comes directly from experimental measurements and is a function of time,

$$T_g\big|_{z=0}=f(t). \qquad 5.9$$

The outlet gas-phase boundary and all boundaries of the other two constituents are assumed to be adiabatic.

5.2.4 Solution procedure

The governing equations, as given by Eqs. 5.1–5.9, are coupled and solved in COMSOL Multiphysics [126]. The properties of the gas mixture are computed using the ideal gas assumption and accounting for local temperature, pressure, and composition [87]. A one-dimensional mesh is generated with a uniform element size of 1% of the total bed length. The Newton automatic highly nonlinear method is used to solve the coupled-nonlinear equations. The solver uses backward differentiation to dynamically modify the time step and reduce computation time; we impose an initial time step of 1×10^{-8} s. Convergence is reached when the relative residuals drop below 10^{-4} for all dependent variables, namely adsorbate concentration in the gas phase and adsorbed phase, pressure, and temperatures of the sorbent, gas, canister, and insulation.

5.3 Results

Breakthrough experiments of carbon dioxide (CO_2) and water (H_2O) in the two cylindrical beds of zeolite 13X (NaX) are analyzed to extract the mass transfer coefficient and apparent axial dispersion. First, the mass transfer coefficient, k_0, is found by fitting simulations to the centerline breakthrough curves of each bed. These simulations use available correlations to predict the pellet-driven, axial-dispersion coefficient as an input to the model. Then the calibrated model (*i.e.*, with the k_0 extracted from centerline breakthrough curve data) is fit to the mixed-exit breakthrough curve to find the apparent axial-dispersion coefficient, $D_{ax,app}$. When determining both unknown parameters, k_0 and $D_{ax,app}$, by fitting the model to experimental data, the sum of squares error (SSE) was minimized for the median 50% of the curve (*i.e.*, $0.25 < x/x_0 < 0.75$) to focus the fit on the slope of the breakthrough curve.

5.3.1 Experimental breakthrough tests for CO_2 and H_2O vapor on zeolite 13X

Experimental breakthrough tests are run for CO_2 and H_2O vapor adsorption in the small-diameter ($d_{bed}/d_p = 17$) and large-diameter ($d_{bed}/d_p = 48$) beds of zeolite 13X. To verify repeatability, three and four repeated breakthrough experiments were respectively conducted for each adsorbate in the small- and large-diameter beds. All breakthrough experiments were performed at a superficial velocity of $u_\infty = 0.23 \pm 0.005$ m/s with a time-averaged, inlet temperature of $T_{g,in} = 25 \pm 0.5$ °C. Table 5.2 summarizes the test parameters for CO_2 and H_2O breakthrough; these values are averaged both over the duration of the breakthrough test (3 h for CO_2 and 7 h for H_2O breakthrough) and across all repeated tests.

The normalized mole fraction of the adsorbate (x/x_0) is plotted as a function of time in Figure 5.3 for CO_2 and H_2O breakthrough at the three measurement locations: the upstream inlet of the bed, at the centerline immediately before the exit of the bed, and downstream of the bed. The downstream measurements were taken sufficiently far away from the bed to ensure a well-mixed flow and are therefore referred to as the mixed-exit data. The centerline measurement location (Figure 5.2) is assumed to be sufficiently far from the walls to accurately neglect the effects of nonplug flow. We hypothesize that the difference between the adsorbate concentration at the centerline and mixed-exit sampling locations is an effect of near-wall-channeling.

Table 5.2. Summary of the inlet and initial conditions for CO_2 and H_2O breakthrough on 13X.

	CO_2		H_2O	
	Small	**Large**	**Small**	**Large**
time-averaged inlet temperature, T_{in} (°C)	25.0	25.3	25.4	25.0
initial temperature, T_{init} (°C)	24.9	25.1	25.0	24.9
ambient temperature, T_{amb} (°C)	23.1	25.3	23.3	25.0
gas flow rate, $\dot{V}$ (SLPM)	12.2	98.0	12.1	99.0
superficial velocity, u_∞ (m/s)	0.230	0.230	0.226	0.232
pressure at bed inlet, p_{in} (kPa)	101.82	114.55	103.38	114.91
inlet adsorbate mole fraction, $x_{CO2,in}$ or $x_{H2O,in}$	0.00304	0.00266	0.0123	0.0121
inlet adsorbate partial pressure, $p_{CO2,in}$ or $p_{H2O,in}$	0.306	0.304	1.27	1.39

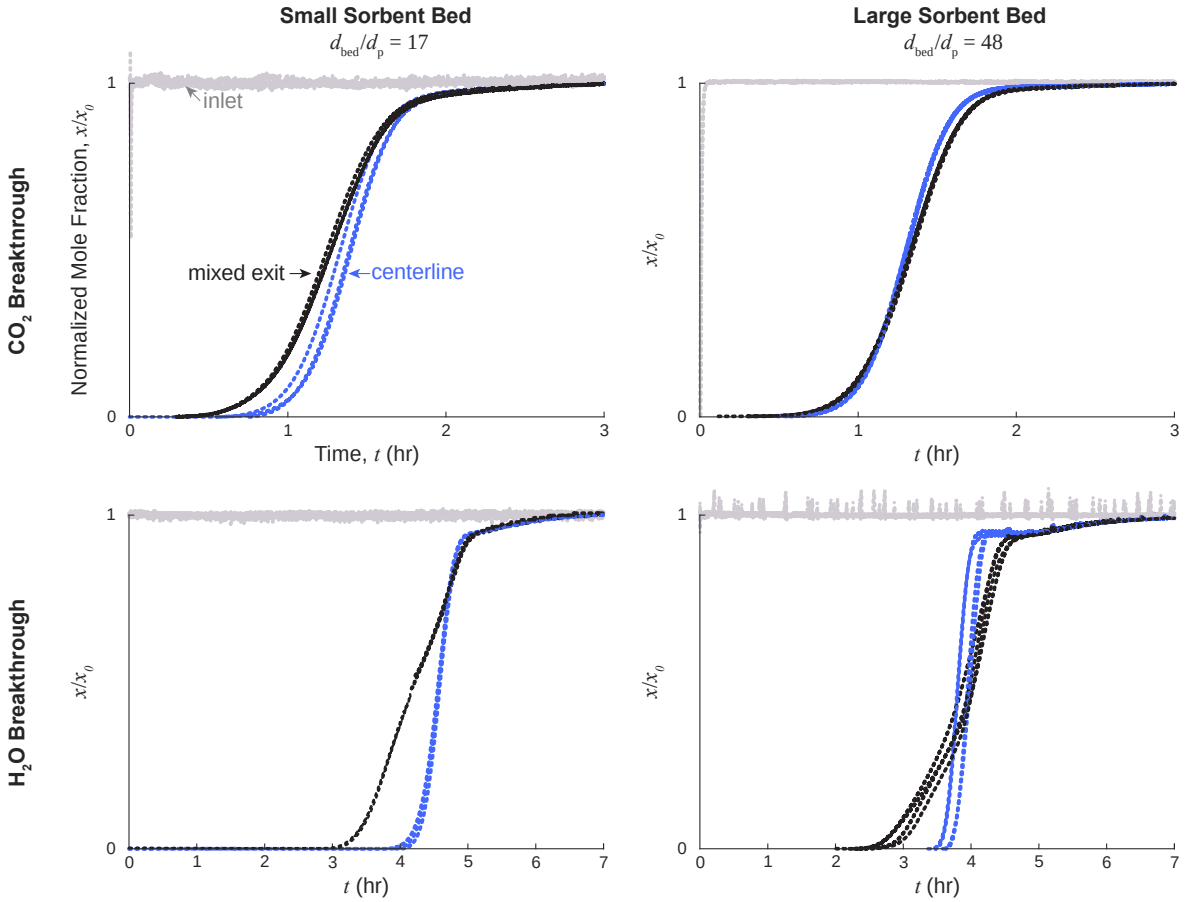

Figure 5.3. Experimental breakthrough curves of CO_2 (top) and H_2O (bottom) on zeolite 13X. These figures plot the mole fraction (normalized to the mean inlet mole fraction, x_0) at three locations: upstream of the bed (gray), at the radial centerline a few millimeters from the end of the bed (blue), and far downstream of the bed (black). Three repeat measurements are shown for the small test stand (left), and four repeat measurements for the large test stand (right).

In the breakthrough curves (*i.e.*, the gas-phase concentration profile histories), discrepancies between the centerline and mixed-exit data are observed for both adsorbates in the small-diameter bed and for water breakthrough in the large-diameter bed. Comparison of these centerline and mixed-exit breakthrough curves provides valuable insight into the nonplug-flow behavior in the beds. An earlier breakthrough in the mixed-exit data, compared with the centerline, is evidence of bed-scale mechanical dispersion. Mechanical dispersion is caused by differences in the flow paths that gas molecules can take through the bed. Pellet-driven dispersion is a well-studied type of mechanical dispersion caused by the stochastic nature of packed beds and is generally assumed to be the dominant dispersive mechanism. Pellet-driven dispersion occurs on the pellet scale and would not cause the differences observed in our experiments between the centerline and mixed-exit data; such differences could only be caused by variations in the velocity at the bed-scale due to wall channeling. Channeling occurs in confined geometries due to a higher near-wall gas velocity caused by increased void fraction close to the wall. While the relative importance of channeling on flow dynamics is known to increase with decreasing bed-to-pellet diameter ratio [166], the extent of wall-channeling effects as a function of bed diameter during confined breakthrough has not been established.

We observe earlier breakthrough of the mixed-exit data in all our experiments (Figure 5.3) implying that wall-channeling effects play a significant role. As expected, the large test stand shows a smaller variation between the centerline and mixed-exit data compared to the small test stand. However, it is noteworthy that wall-channeling effects are observed for the larger-diameter bed (d_{bed}/d_p = 48) as well, because a bed-to-pellet diameter ratio of 20 has been thought to be sufficiently large to obviate wall effects. [76] It is also worth noting that the discrepancy between the centerline and mixed-exit concentrations is significantly more pronounced for H_2O breakthrough than for CO_2 breakthrough tests, indicating that adsorption equilibrium and kinetics affect the degree of radial variation in concentration.

The experimental breakthrough curves can be nondimensionalized to allow for direct comparison between the two adsorbates. Figure 5.4 plots the normalized concentration at the centerline (solid lines) and mixed-exit (dashed lines) against the nondimensional time,

$$\bar{t} = \frac{t}{t_{\text{stoich}}}, \tag{5.10}$$

where the stoichiometric time [167] is defined using the mixed-exit concentration as

$$t_{\text{stoich}} = \int_0^{\infty} \left(1 - \frac{x_{\text{ME}}}{x_0}\right) dt\,. \tag{5.11}$$

The offset between the centerline and mixed-exit curves at x/x_0 = 0.5 should be independent of adsorbate for a system with constant mechanical dispersion. We observe that the mixed-exit curves in the small bed cross at $\bar{t}$ = 0.991 and 0.990 for CO_2 and H_2O, respectively, while the centerline curves cross at $\bar{t}$ = 1.076 for both adsorbates. This equates to a difference in nondimensional time $\Delta\bar{t}$ of 0.085 and 0.086 for CO_2 and H_2O, respectively. The large bed yields smaller differences between the centerline and mixed-exit curves ($\Delta\bar{t}$ = 0.024 and 0.025 for CO_2 and H_2O respectively), which is expected because the large bed should have reduced wall-channeling-induced dispersion effects. The results in Figure 5.4 confirm that, as expected based on the analysis of Knox *et al.*[15], the observed mechanical dispersion is a function of the bed diameter but independent of adsorbate/adsorbent pair.

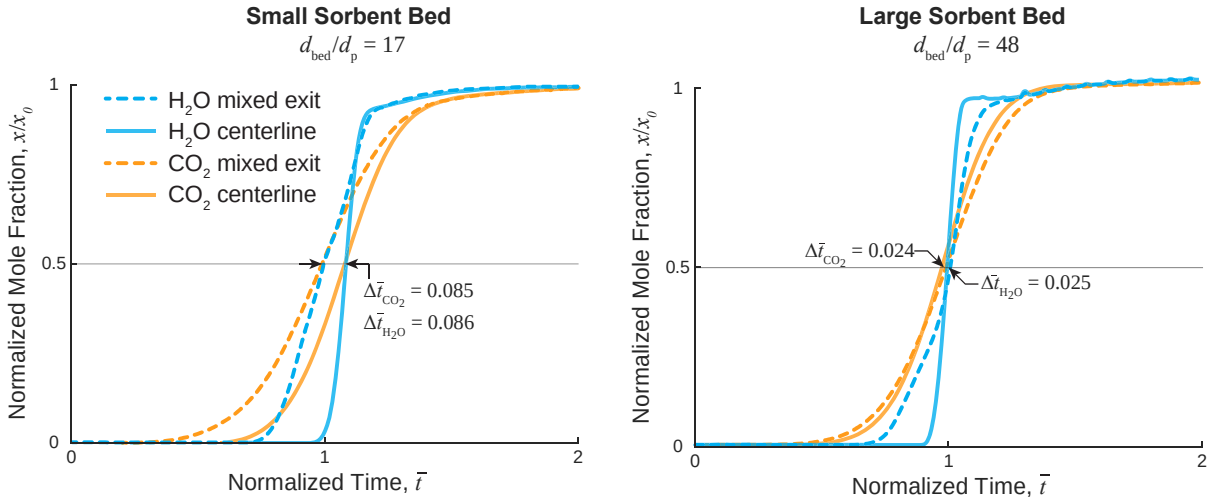

Figure 5.4. Experimental breakthrough curves of CO_2 and H_2O on zeolite 13X plotted against normalized time for the small-diameter bed and the large-diameter bed. Breakthrough curves measured at the mixed-exit and centerline locations are shown as dashed and solid lines respectively.

5.3.2 Extracting mass transfer coefficients

Traditionally, mass transfer coefficients are determined from breakthrough experiments by using mixed, downstream concentration measurements. This method is inaccurate for a small-diameter bed where wall-channeling effects dominate dispersion, because it requires that the axial mixing behavior is accurately described by *a priori* prediction of pellet-driven dispersion. Knox *et al.*[15] proposed a method to more accurately obtain the mass transfer coefficient from small-diameter reactors by using centerline measurements of concentration immediately before the exit of the bed. The method assumes that axial dispersion in the center of the bed (far from the canister wall) can be accurately predicted by empirical correlations for pellet-driven dispersion. We follow this procedure to extract the mass transfer coefficients from the experimental measurements.

Using the pellet-driven, axial-dispersion coefficient from the Edwards and Richardson correlation [86] and the centerline void fraction (calculated by the Cheng equation [168]) as inputs, the model is fit to the centerline measurement of concentration by varying k_0 to minimize the sum-of-squared error between experimental and simulation results. This fitting is repeated for each individual breakthrough curve and the average of these fitted values is listed in Table 5.3. Note that the equilibrium adsorbed-phase concentration was adjusted to match the capacity seen in the breakthrough experiments by multiplying the predicted capacity, n^*, by a constant value (listed in Table 5.3). We found that the required capacity adjustment for the large-diameter bed was consistently lower than the capacity adjustment for the small bed by ~10%; we attribute this to a minor amount of water contamination in the large bed caused by exposure during the longer installation time. Such capacity shifts have no impact on the slope of the curve and are thus inconsequential to the resulting mass transfer coefficient fit.

Table 5.3. Summary of the mass transfer coefficient (k_0) fitting for each adsorbate and test stand.

	CO_2		**H_2O**	
	Small	**Large**	**Small**	**Large**
void fraction at centerline, ε_{CL}	0.350	0.321	0.350	0.321
bulk void fraction, ε_{bulk}	0.368	0.327	0.368	0.327
equilibrium capacity adjustment	0.97	0.88	1.16	1.07
pellet-driven dispersion, $D_{ax,p}$ (m/s^2)	0.00095	0.0011	0.00099	0.0011
fitted mass transfer coefficient, k_0 (1/s)	57	51	140	170

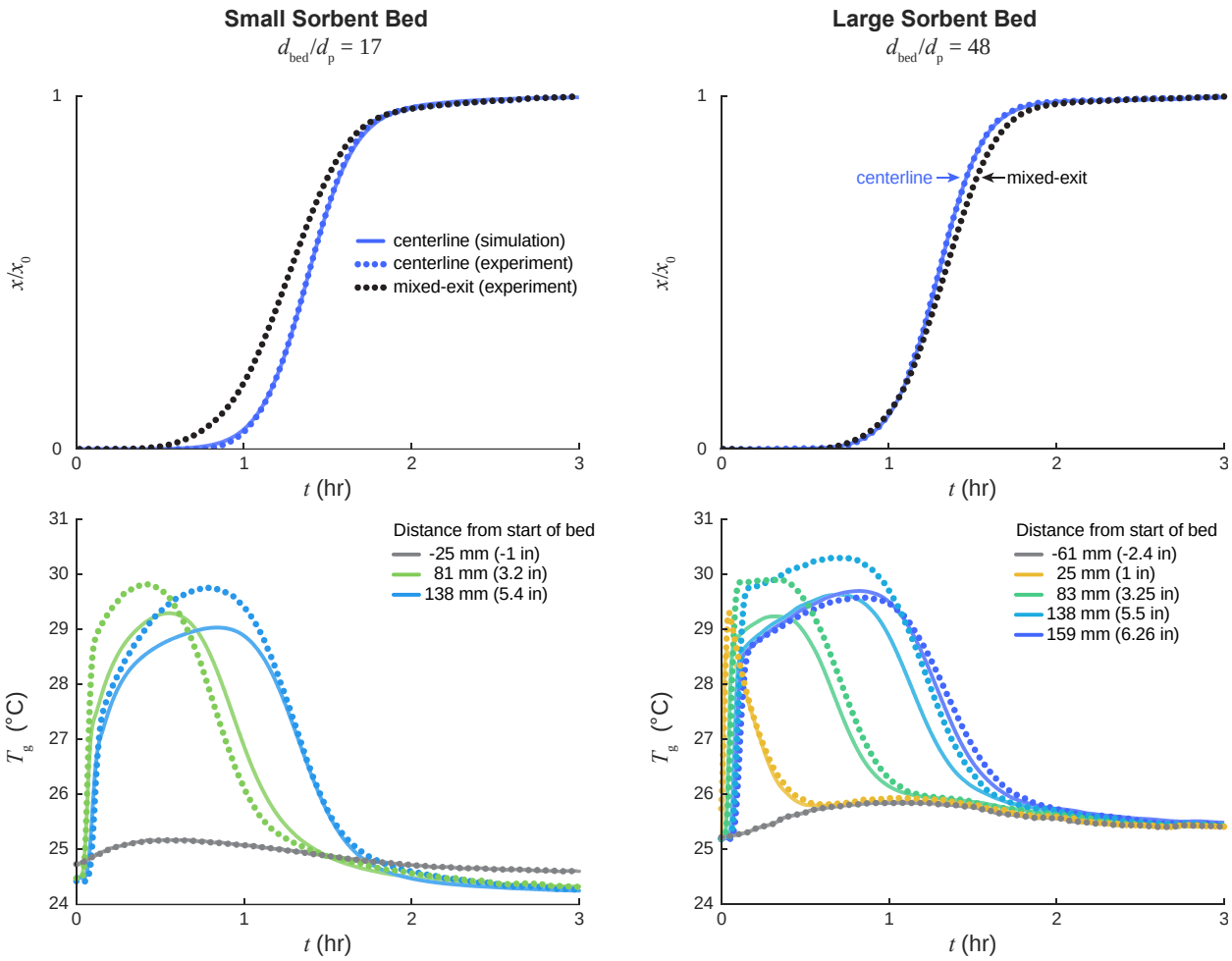

Figure 5.5. CO_2 breakthrough simulation results fitted to centerline data (with $D_{ax,p}$ and calibrated k_0 as given in Table 5.3) compared to experimental measurements. *Top panels*: Comparison of experimental (dotted) and simulated (solid) breakthrough curves. *Bottom panels*: Corresponding gas-temperature profile histories for simulations (solid) and experimental measurements (dotted): before (gray) and at several axial positions within (colored) the bed.

The calibrated best-fit simulation results are plotted over top of the experimental data for CO_2 breakthrough in Figure 5.5 and for H_2O in Figure 5.6, and the corresponding best-fit k_0 values are tabulated in Table 5.3. These plots include data from a single, representative breakthrough experiment; dotted lines represent experimental data, and solid lines represent simulation results. The upper panels of Figure 5.5 and for H_2O in Figure 5.6 plot the gas-phase mole fraction of adsorbate normalized to the inlet adsorbate mole fraction, x/x_0, at the centerline and mixed-exit sampling locations; the lower panels contain temperature profile histories at several axial locations within the bed.

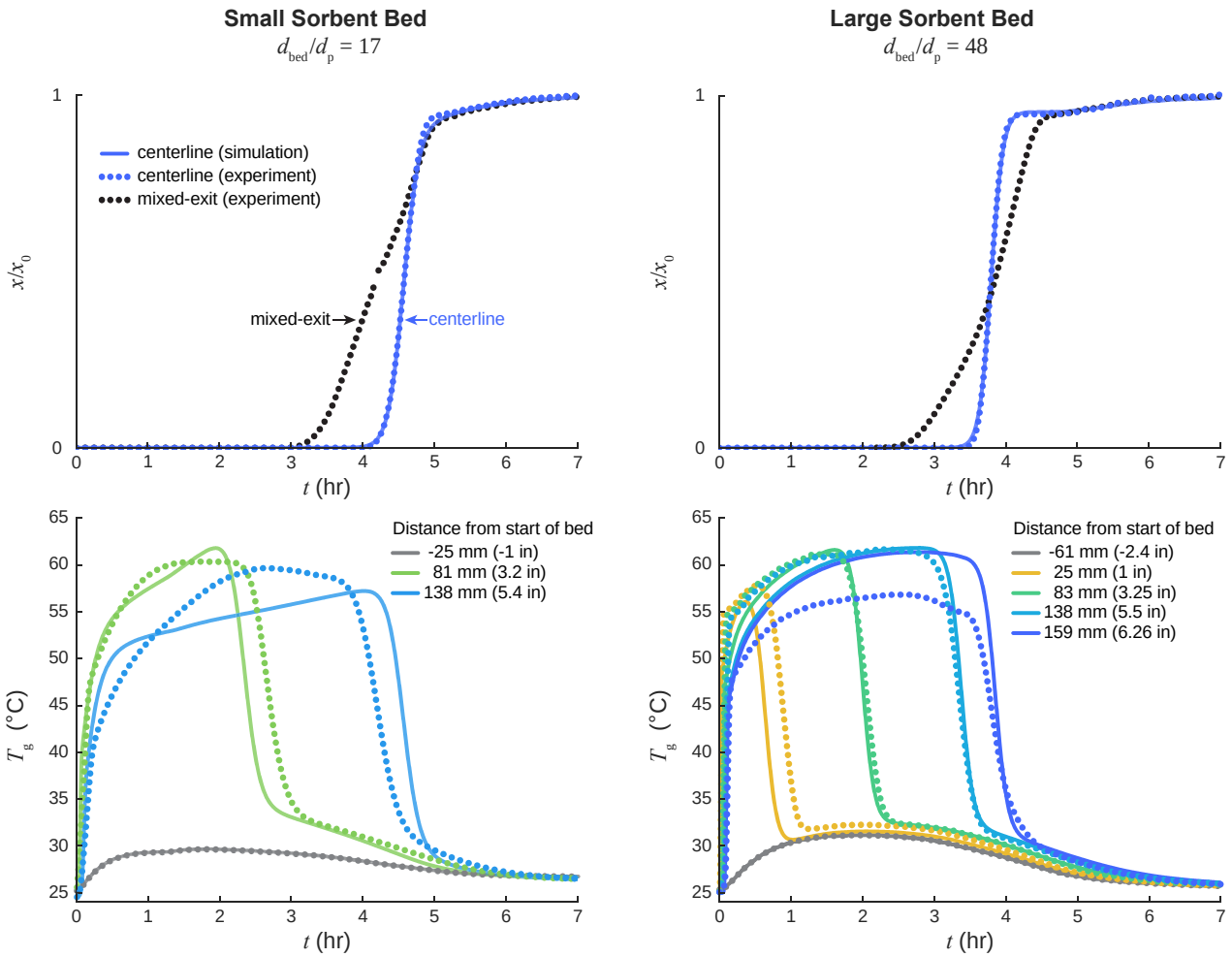

Figure 5.6. H_2O breakthrough simulation results fitted to centerline data (with $D_{ax,p}$ and calibrated k_0 as given in Table 5.3) compared to experimental measurements. *Top panels*: Comparison of experimental (dotted) and simulated (solid) breakthrough curves. *Bottom panels*: Corresponding gas-temperature profile histories before (gray) and at several axial positions within (colored) the bed.

Note that the simulation is one-dimensional and thus cannot capture radial variations in concentration; when referring to the *centerline* simulation data we are referring to simulation results that correspond to the axial location of the centerline tube in the bed (*i.e.*, $z = 0.97L$ and $z = 0.96L$ for the small and large-diameter beds respectively). Similarly, *exit* simulation data refer to data from the end of the bed ($z = L$), which is the simulation equivalent to the mixed-exit sampling location from experiments. The fitted model predictions show good agreement with centerline experimental data. The simulated and experimental concentration at the centerline sampling location (blue) overlap substantially, such that the individual curves are indistinguishable.

The model also provides a good match to the measured temperatures within the bed. The shapes of the simulated and experimental curves agree throughout the breakthrough period, and the temporal locations of peak temperatures are well-matched. We attribute the slight discrepancies in the magnitude of peak temperatures to temperature nonuniformities caused by radial heat loss within the bed, which cannot be captured in a 1-D model. The slopes of both the model and experimental gas temperatures are closely matched in the decreasing region (below approximately 29 °C for CO_2 breakthrough and 55 °C for H_2O breakthrough) where mass transfer effects dominate the temperature profile. This match indicates that the correct mass transfer coefficient was extracted from fitting the model to the experimental centerline breakthrough curves.

The resulting best-fit k_0 are given in Table 5.3. The mass-transfer coefficient of H_2O adsorption is larger than that of CO_2 by a factor of approximately three; this is expected given the strong affinity of zeolite 13X for water [169]. More importantly, we see that the fitted mass transfer coefficient, k_0, is independent of the sorbent bed diameter; for both adsorbates, k_0 fit to data from the small- and large-diameter beds matches to within 20% (on the same order of magnitude as test repeatability). These results for two beds of vastly different sizes validates the method proposed by Knox *et al.* [15] for extracting k_0 from the centerline breakthrough curve and demonstrates that the extracted mass transfer coefficients are independent of bed diameter as they anticipated.

To further illustrate the importance of measuring the centerline adsorbate concentration, we used the traditional method of extracting the mass transfer coefficient from the mixed-exit data of the small-diameter test stand. Using the traditional fitting method, we find that $k_0 = 37\ s^{-1}$ for CO_2 adsorption and $k_0 = 28\ s^{-1}$ for H_2O adsorption. Both mass transfer coefficients are significantly different from the values we obtained via the centerline data (Table 5.3). The traditional fitting method erroneously yields a k_0 that is approximately half the actual value for CO_2 adsorption and one-fifth the actual value for H_2O adsorption.

5.3.3 Extracting apparent axial dispersion coefficients

In Section 5.3.1, we discussed the discrepancy in centerline and mixed-exit breakthrough curves caused by wall channeling within the bed. We then used a method for extracting mass transfer coefficients from the centerline breakthrough curve in Section 5.3.2. The current section describes

the extraction of the apparent axial dispersion—which includes wall-channeling effects on dispersion—from the mixed-exit breakthrough curve. This is followed by a discussion of the extracted apparent dispersions as well as the limitations of the axially dispersed plug-flow model to predict adsorption of strongly attractive species (*i.e.*, H_2O on 13X).

After extracting the mass transfer coefficient, the apparent axial-dispersion coefficient, $D_{ax,app}$, can be determined from the mixed-exit concentration measurements. The mass transfer coefficient, k_0, obtained from the centerline breakthrough curve and the bulk void fraction are used as inputs (see Table 5.3). The model is then fit to the mixed-exit breakthrough curve by varying the value of D_{ax}; the value that provides the best fit is taken as the apparent axial dispersion of the system, $D_{ax,app}$. These fitted, apparent dispersions are tabulated in Table 5.4 along with the pellet-driven dispersion derived from the empirical correlation of Edwards and Richardson [86] for comparison.

Figure 5.7 compares the fitted model predictions to experimental measurements for CO_2 breakthrough. The top panels show simulation predictions of the gas-phase concentration breakthrough curves at multiple axial locations along the bed, as well as experimental data from the centerline and mixed-exit sampling locations. The corresponding derivatives (*i.e.*, slopes of these concentration breakthrough curves) of the simulation predictions are plotted in the bottom panels. The simulation model captures the shape of the mixed-exit experimental breakthrough curve (black dotted line) for both the small- and large- diameter beds. To achieve this match, the model required axial-dispersion coefficients that were significantly larger than the pellet-driven dispersion predicted by Edwards and Richardson [86].

Table 5.4**.** Summary of axial-dispersion coefficients (D_{ax}) for each adsorbate and test stand.

	CO_2		**H_2O**	
	Small	**Large**	**Small**	**Large**
pellet-driven dispersion, $D_{ax,p}$ (m/s^2)	0.00095	0.0011	0.00099	0.0011
fitted apparent dispersion, $D_{ax,app}$ (m/s^2)	0.0043	0.0015	-	-

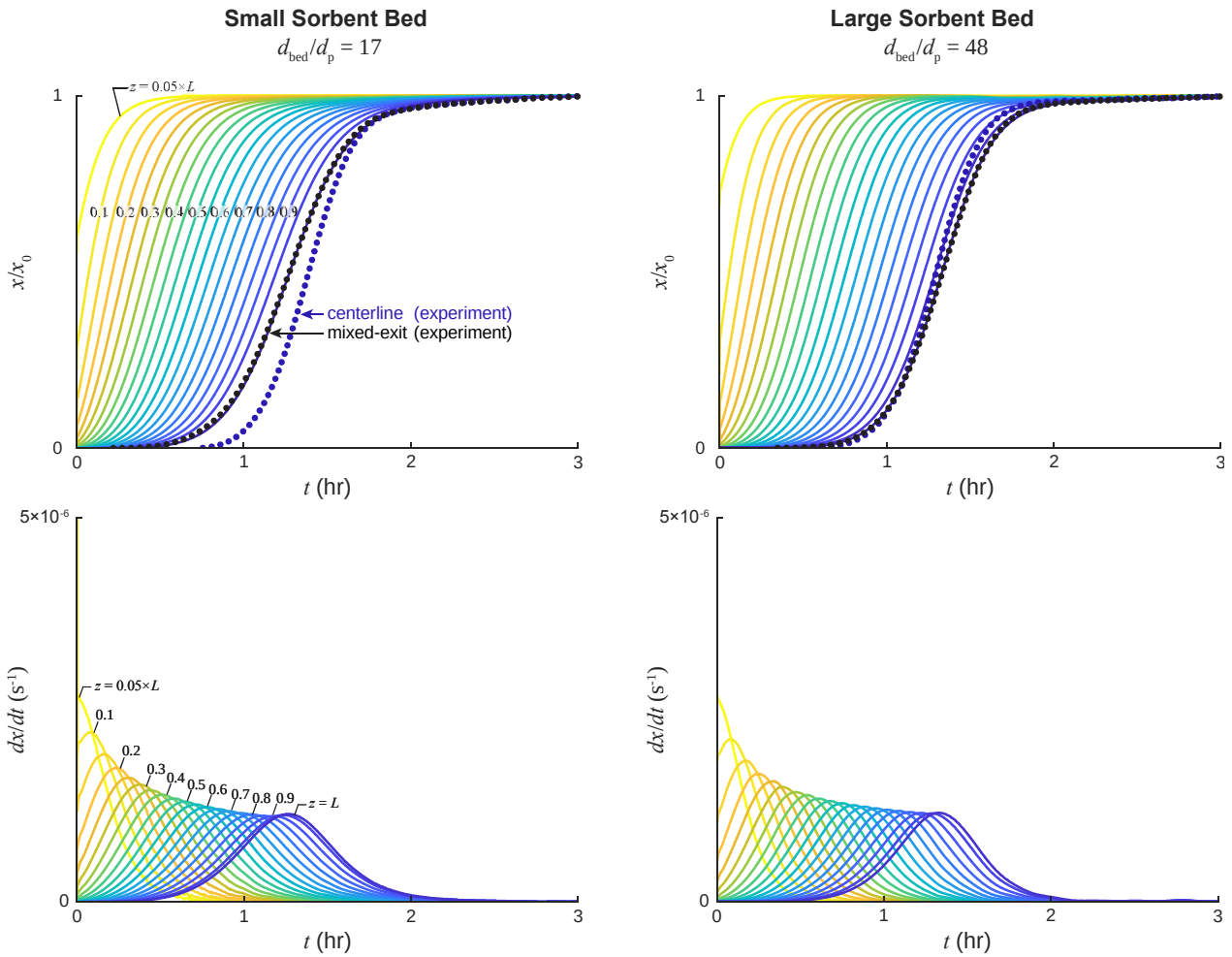

Figure 5.7. CO_2 breakthrough simulation results fitted to mixed-exit data (with calibrated k_0 and $D_{ax,app}$ as given in Table 5.3 and Table 5.4 respectively) compared to experimental measurements. *Top panels*: Comparison of and experimental breakthrough curves (dotted) and simulation curves (solid) which show the time-history of concentration in 5% increments along the bed. *Bottom panels*: Corresponding derivatives of the simulated breakthrough curves.

The apparent dispersion of the small-diameter bed is approximately four times larger than that of the large-diameter bed. Furthermore, the $D_{ax,app}$ extracted from CO_2 experiments in the large-diameter test stand is only 45% larger than the pellet-driven dispersion predicted by the Edwards and Richardson [86], indicating that pellet-driven dispersion accounts for most of the axial dispersion in the large bed. In contrast, the $D_{ax,app}$ fitted to the small-diameter bed is 300% larger than the predicted pellet-driven dispersion. Given that both beds were exposed to identical inlet conditions ($p_{CO2,in}$ = 0.3 kPa, u_∞ = 0.23 m/s, and $T_{g,in}$ =25 °C), differences in $D_{ax,app}$ must be caused by variations in geometry between the two beds. As described in Section 5.3.1, differences in the

centerline and mixed-exit breakthrough curves indicate that there are spatial variations in velocity throughout the bed. In both beds, there is a radial variation in porosity caused by inefficient packing near the wall which in turn leads to higher velocities in the near-wall region. The portion of the affected by these porosity variations is inversely proportional to the size of the bed; thus, the spatial variation in velocity and apparent dispersion increase as the bed becomes more confined.

Further conclusions about the flow behavior can be drawn from the slopes of the simulated breakthrough curves. In the bottom panels of Figure 5.7, the highest point of each individual dx/dt curve represents the slope of the corresponding breakthrough curve at $x/x_0 = 0.5$. The peaks of these curves approach a constant value with increasing depth into the bed. This trend is characteristic of constant pattern behavior (CPB), defined by an adsorbate concentration front that propagates through the bed without changing shape. CPB is a widely established phenomenon that is theoretically expected [141] and has been experimentally confirmed [170], [171] to occur for systems with favorable Type I isotherms [170], [171], such as CO_2 adsorption on 13X.

There is an even more pronounced difference between the mixed-exit and centerline concentration time-profiles in the H_2O breakthrough experiments (bottom panels of Figure 5.3). This difference is so significant that the model begins to show nonphysical behavior as the apparent axial-dispersion coefficient is increased in an attempt to match the slope of the mixed-exit breakthrough curve. Figure 5.8 compares the experimental measurements for H_2O breakthrough on zeolite 13X in the large-diameter bed with simulation predictions using an apparent axial dispersion that is 1, 10, and 100 times greater than that predicted from the Edwards and Richardson [86] correlation. Note that the top panel corresponds to a value of $D_{ax} = D_{ax,p}$, as used in Section 5.3.2 to extract the mass transfer coefficient. As such, the model closely matches the shape of the experimentally measured centerline breakthrough curve (top panel in Figure 5.8), but very poorly captures the mixed-exit data.

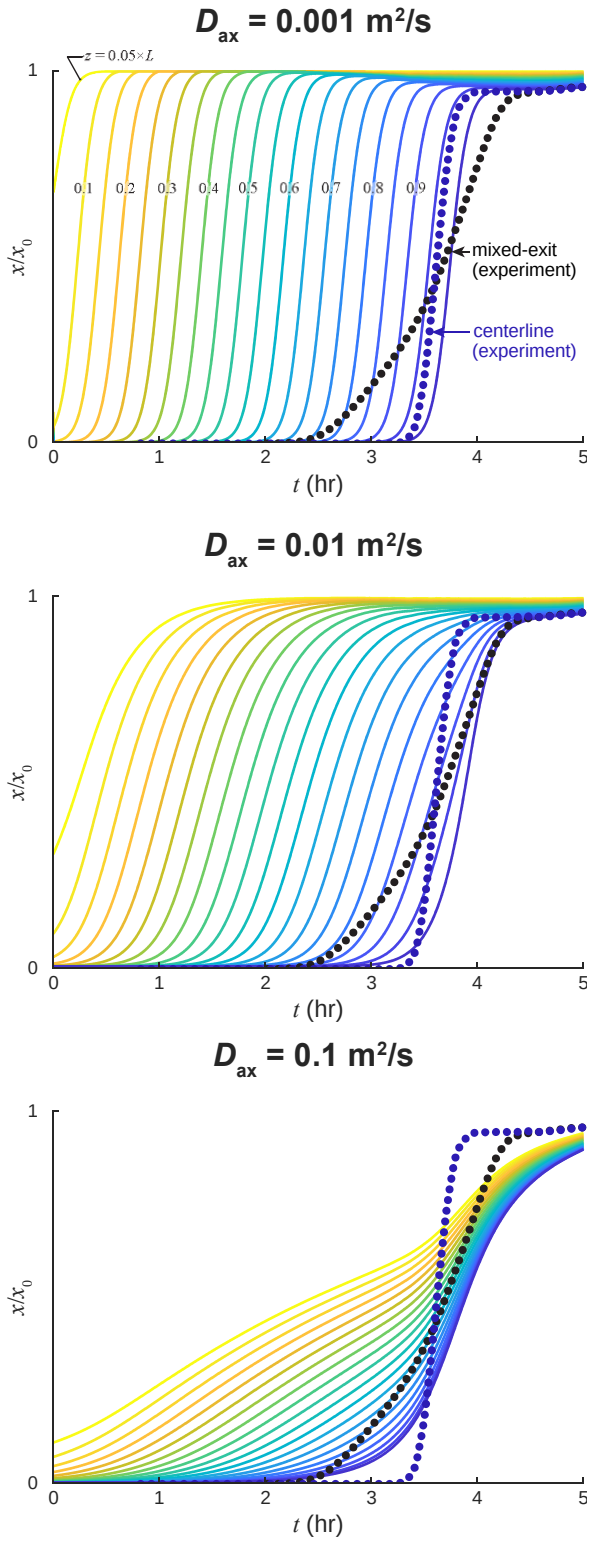

Figure 5.8. Comparison of simulated (solid) and experimental (dotted) breakthrough curves of H_2O on zeolite 13X in the large-diameter bed as measured at the radial centerline. Simulation curves show the time-history of concentration in 5% increments along the bed length.

As $D_{ax,app}$ is increased, the gas-phase concentration curves become distorted near the beginning of the bed. While this distortion is confined to a small portion of the bed entrance for low to moderate dispersion coefficients (*e.g.*, 0.01 m^2/s), the distortion extends to the full length of the bed at high apparent dispersion coefficients (*e.g.*, 0.1 m^2/s). This distortion is an unphysical artifact that arises when attempting to capture the highly 2-D flow effects by tuning the axial-dispersion coefficient in a 1-D model. Unlike the CO_2 breakthrough experiments, the 1-D assumption breaks down for H_2O breakthrough experiments.

The H_2O simulations required a far higher value for $D_{ax,app}$ (>100 × $D_{ax,p}$) to capture the slope of the experimentally measured breakthrough curve measured downstream of the bed relative to that required for the CO_2 system (only 4 × $D_{ax,p}$), revealing that the interplay of the adsorbate/adsorbent system and the mechanical dispersion mechanisms can induce significant radial variations in concentration. While the exact nature and extent of this interplay is not clear, it is apparent that the water/zeolite 13X breakthrough curves are dominated by 2-D flow conditions, and therefore, the axially dispersed plug-flow model cannot be applied to this system. As such, we do not list values for the apparent axial-dispersion coefficient for H_2O breakthrough Table 5.4 because the model itself breaks down for this adsorbate/adsorbent pair.

5.4 Conclusions

This chapter examined the effect the effect of geometric confinement on apparent axial dispersion in fixed-bed adsorption systems using experimental measurements and an axially dispersed plug-flow model. Breakthrough experiments of CO_2 and H_2O on beds of zeolite 13X were performed in two cylindrical test stands with d_{bed}/d_p = 17 and 48. Measurements of the adsorbate concentration were collected at a location far downstream of the bed where the effluent is well-mixed, and at a centerline location within the bed immediately before the exit. An axially dispersed plug-flow model was developed and fit to these experimental data to extract mass transfer and axial-dispersion coefficients.

The intrabed, centerline breakthrough curve was used to extract the mass transfer coefficient, k_0, in the two beds under identical inlet and initial conditions. Similar mass transfer coefficients were obtained for both beds even when the beds experienced considerable near-wall channeling, *i.e.*, a

nonplug-flow mechanical dispersion. This confirmed the recommendation of Knox *et al.* [15] that k_0 can be extracted from centerline breakthrough curves, independent of the bed diameter, even when nonplug-flow conditions prevail in the bed. In comparison, k_0 values extracted using the traditional method of fitting to mixed-exit breakthrough curve yielded significant differences relative to those extracted from centerline data (deviations of 40% for CO_2 and 500% for H_2O). Our results demonstrate how inaccurate prediction of D_{ax}—due to the prevalence of nonplug-flow conditions—can lead to severe errors in the mass-transfer coefficients fitted to mixed-exit breakthrough curves.

This work also compared the mixed-edit and centerline measurements to identify when nonplug-flow conditions dominate the flow. A priori predictions of axial dispersion from existing correlations—which do not account for the effects of confinement—were shown to grossly underpredict the apparent axial dispersion in confined geometries. As a result, the breakthrough time predicted using a 1-D model was found to be incorrect by as much as 1 h (compared with experimental measurements). Wall channeling effects were observed to be significant even at $d_{bed}/d_p = 48$. This is in stark contrast to the prevailing consensus in the literature, which states that wall effects as negligible for beds with $d_{bed}/d_p \geq 20$. Furthermore, the degree to which the 1-D model predictions deviated from experimentally observed breakthrough was a strong function of the adsorbent/adsorbate pair with H_2O showing significant greater wall-effects compared to CO_2, even though experiments for both adsorbates were run with identical flow conditions. Attempts to match the slope of the experimental mixed-exit breakthrough curve yielded nonphysical model predictions for water; the axially disperse plug-flow model with the Danckwert's outlet boundary condition fails to capture the physics of these experiments.

Despite the limitations of the axially disperse plug-flow model in describing confined geometries, this model can be used to extract accurate mass-transfer and dispersion information from experimental breakthrough curves when measured both inside and outside the bed. We recommend that intrabed concentration be measured when extracting mass transfer coefficients from breakthrough experiments.

6. EFFECT OF RADIAL FLOW VARIATIONS ON BREAKTHROUGH IN CONFINED GEOMETRIES

This chapter uses a two-dimensional adsorption model to examine the interplay of wall-channeling and adsorption transport on breakthrough in confined geometries. Experimental results for breakthrough of carbon dioxide (CO_2) and water (H_2O) in a bed of zeolite 13X are compared to illustrate how the adsorbate/adsorbent pairing affects the radial variation in concentration. To examine this behavior, the effect of radial variations in bed porosity on the flow velocity profile is implemented into two-dimensional, axisymmetric adsorption model. The 2-D simulation results are validated against experimental data and compared to 1-D results to illustrate the critical need to account for these radial variations. The validated 2-D model is then used to investigate the specific adsorption kinetics and equilibrium parameters that cause H_2O to exhibit more significant radial variations in concentration during breakthrough compared with CO_2. It is found that breakthrough concentration profiles are sensitive to the mass-transfer resistance, and that radial variations in concentration due to wall-channeling effects become more pronounced as the mass-transfer resistance decreases. Therefore, wall-channeling effects can be significant at larger-than-expected bed-to-pellet diameter ratios (~50) for adsorbate/adsorbent pairings having fast adsorption kinetics.

6.1 Experimental procedure

Experimental results are taken from Chapter 5 (Son *et. al.* [160]) to provide data for model validation. A detailed description of the experimental facility and results can be found in Chapter 5. The main features of the facility are summarized here.

The experimental facility contains an aluminum canister which houses a fixed-bed of zeolite 13X adsorbent (Grace Davidson MS544-13X). The canister and bed dimensions are provided in Figure 5.1, and the thermophysical sorbent properties from the manufacturer [81] are listed in Table 5.1. A system of flow controllers, a humidification loop, and a mixing chamber upstream of the bed provide a finely controlled flow of adsorbate/carrier gas to the sorbent bed. The gas composition is monitored at three locations during the breakthrough test: (1) far upstream of the bed, (2) far

downstream of the bed, and (3) within the bed. The downstream sampling location is located sufficiently far away from the bed that the flow is well mixed, we thus refer to this as the mixed-exit location. The intrabed sampling location measured a small portion of the flow at the radial centerline, 6 mm away from the end of the bed as shown in Figure 5.1. This centerline location of the flow is assumed to be sufficiently far from the walls to neglect nonplug effects.

To perform breakthrough tests, the bed is initially filled with only N_2 and then exposed to an inlet flow of N_2 and adsorbate (either CO_2 or H_2O) at $t = 0$. The inlet flow is maintained at a constant superficial velocity and constant adsorbate concentration, while the outlet is maintained at a constant total pressure. The pellets adsorbed CO_2 or H_2O as the gas mixture passes through the bed while allowing the N_2 carrier gas to pass through uninhibited. Eventually, there is a small quantity of adsorbate detected in the bed effluent. The time at which this occurs is termed the initial breakthrough time, t_b. For this work, the initial breakthrough time is defined as the time at which the effluent mole fraction first reaches 1% of the influent mole fraction, $x/x_0 = 0.01$. The test continued until the bed is completely saturated (*i.e.*, $x/x_0 \geq 0.99$). Table 6.1 summarizes the experimental thermal and flow conditions, which were kept the same for both adsorbates, and Table 6.2 summarizes the mass transfer coefficient and equilibrium capacity of each adsorbate.

Table 6.1. Summary of the flow and thermal conditions for H_2O and CO_2 breakthrough experiments.

Quantity	Value
inlet temperature, T_{in} (°C)	25
initial temperature, T_{init} (°C)	25
ambient temperature, T_{amb} (°C)	25
superficial velocity, u_∞ (m/s)	0.23
pressure at bed outlet, p_{out} (kPa)	111
canister–ambient heat transfer resistance, $R'_{can-amb}$ K/(m W)	0.304

Table 6.2. Summary of inlet adsorbate mole fraction, adsorbent capacity, and mass transfer coefficient for breakthrough of CO_2 and H_2O on zeolite 13X.

Quantity	CO_2	H_2O
inlet adsorbate mole fraction, x_{in}	0.00266	0.0121
equilibrium concentration at inlet conditions, n^* (mol/kg)	1.3	15.2
Mass transfer coefficient, k_0 (s^{-1})	51	170

6.2 Modeling approach

A two-dimensional, axisymmetric model of the sorbent bed is used to model the water breakthrough experiment described in Section 6.2. For this model, we assume that:

1. the rate of adsorption can be modeled using the linear-driving force assumption;
2. porosity is a function of radial position (*i.e.*, distance from the wall);
3. all bed properties are axially uniform but can vary radially as a function of local porosity;
4. the gas phase behaves as an ideal gas.

This two-dimensional, axisymmetric model of the sorbent bed comprises two mass balances, a momentum balance, and three energy balances; the latter allows independent tracking of the temperature of the gas, sorbent, and canister wall. These six governing equations are coupled and solved to obtain the adsorbate concentration and temperatures as a function of time and radial/axial position within the bed.

6.2.1 Conservation of mass

The gas-phase mass conservation accounts for adsorption, advection, and axial dispersion as

$$\varepsilon_r \frac{\partial c}{\partial t} + (\mathbf{u}\cdot\nabla)c - \nabla\cdot(\varepsilon_r \mathbf{D}\nabla c) = -(1-\varepsilon_r)\frac{\partial n}{\partial t} \tag{6.1}$$

where c is the gas-phase concentration of the adsorbate (*e.g.*, H_2O), n is the adsorbed-phase concentration of the adsorbate, ε_r is the radially dependent porosity, **u** is the local superficial velocity (*i.e.*, the Darcy velocity), and **D** is the dispersion coefficient tensor. The local porosity is calculated by the empirical expression of Giese [172] as,

$$\varepsilon_r(r) = \varepsilon_\infty\left[1 + 1.36\exp\left(-5.0\frac{r_{\text{bed}} - r}{d_p}\right)\right] \tag{6.2}$$

where r is the radial distance from the centerline of the bed and ε_∞ is the porosity far from the wall. Integrating Eq. 6.2 over the cross-sectional area of the bed and equating with the experimentally measured [160] average bed porosity ($\bar{\varepsilon}$ = 0.327), we find ε_∞ = 0.320. The dispersion coefficient tensor,

$$\mathbf{D} = \begin{bmatrix} D_{\mathrm{r}} & 0 \\ 0 & D_{\mathrm{ax}} \end{bmatrix} \tag{6.3}$$

is composed of the axial- and radial-dispersion coefficients, respectively calculated per the empirical correlations of Delgado [47] as

$$D_{\mathrm{r}} = D_{\mathrm{M}} \left[\frac{1}{\sqrt{2}} + \frac{1}{12} \frac{u_{\mathrm{i}} d_{\mathrm{p}}}{D_{\mathrm{M}}} \right] \tag{6.4}$$

where D_{M} is the molecular diffusivity of water, and Edwards and Richardson [86] as

$$D_{\mathrm{ax}} = d_{\mathrm{p}} u_{\mathrm{i}} \left[\frac{0.73\varepsilon}{Re_{\mathrm{p}} Sc} + \frac{Pe_{\infty}^{-1}}{1 + \dfrac{9.49\varepsilon}{Re_{\mathrm{p}} Sc}} \right] \tag{6.5}$$

where [92]

$$Pe_{\infty} = \begin{cases} 6.7 \times \left(d_{\mathrm{p}} / [cm] \right) & d_{\mathrm{p}} \le 0.3 \text{ cm} \\ 2.0 & 0.3 \text{ cm} < d_{\mathrm{p}} \end{cases} . \tag{6.6}$$

See the *Nomenclature* section for definitions of the Reynolds number Re_{p} and Schmidt number Sc.

We use the linear-driving-force (LDF) approximation [13] to express the adsorption rate as

$$\frac{\partial n}{\partial t} = k_l \left(n^* - n \right) \tag{6.7}$$

where k_l is the LDF mass transfer coefficient and n^* is the equilibrium adsorbed-phase concentration. The equilibrium adsorbed-phase concentration is input to the model a function of adsorbate partial pressure and sorbent temperature using the Aranovich–Donohue model and Sips isotherm as described by Son *et al.* [139]. Adsorption on zeolite 13X is rate-limited by macropore diffusion [164], [165]; thus the LDF mass transfer coefficient should be expressed as [16]

$$k_l = \frac{k_0}{n^*} \tag{6.8}$$

where k_0 is a constant parameter referred to as simply the mass transfer coefficient. We previously found [160] the mass transfer coefficient for water adsorption on zeolite 13X to be $k_0 = 170 \text{ s}^{-1}$ by empirical fitting.

6.2.2 Conservation of momentum

Gaeini *et al.* [173] recently surveyed models for flow through a fixed-bed adsorber considering the effects of radial variation in porosity in the near-wall region. They found that the Brinkman extension to the Darcy–Forchheimer equation with an effective viscosity expression by Bey and Eigenberger [174] and radial bed void fraction profile by Giese [165] (Eq. 6.2) best represented the experimentally observed velocity profile in a bed of zeolites. Following this recommendation, we account for the Brinkman viscous dissipation, Darcy viscous dissipation and Forchheimer inertial dissipation terms. We additionally extend the momentum balance to account for radial velocities—which we observed to have significant impact on the predicted initial breakthrough time. The conservation of momentum equations can thus be written as,

$$\frac{\rho_{\mathrm{g}}}{\varepsilon_r}\left(\frac{\partial \mathbf{u}}{\partial t}+\left(\nabla\cdot\mathbf{u}\right)\frac{\mathbf{u}}{\varepsilon_r}\right)=-\nabla p+\nabla\cdot\left[\frac{\mu_{\mathrm{eff}}}{\varepsilon_r}\left\{\nabla\mathbf{u}+\left(\nabla\mathbf{u}\right)^{\mathrm{T}}-\frac{2}{3}\left(\nabla\cdot\mathbf{u}\right)\mathbf{I}\right\}\right]-\mathbf{u}\left(\frac{\mu_{\mathrm{eff}}}{\kappa}+\beta\left|\mathbf{u}\right|-\frac{1}{{\varepsilon_r}^2}\frac{\partial n}{\partial t}\right) \quad 6.9$$

and

$$\frac{\partial}{\partial t}\left(\varepsilon_r\rho_{\mathrm{g}}\right)+\nabla\cdot\left(\rho_{\mathrm{g}}\right)\mathbf{u}=\frac{\partial n}{\partial t} \quad 6.10$$

where ρ_{g} is the gas-phase density determined by the ideal gas law. The effective viscosity is predicted from the model of Bey and Eigenberger [174] as

$$\mu_{\mathrm{eff}}=\mu_g\left[1+\left(7\times10^{-6}\frac{d_{\mathrm{bed}}}{d_{\mathrm{p}}}+2\times10^{-5}\right){Re_p}^2\right]. \quad 6.11$$

The empirical correlation of Cheng [168] is to express the bed permeability,

$$\kappa(r)=\frac{{\varepsilon_r}^3}{\left(1-\varepsilon_r\right)^2}{d_p}^2\left[185+17\frac{\bar{\varepsilon}}{1-\bar{\varepsilon}}\left(\frac{d_{\mathrm{bed}}}{d_{\mathrm{bed}}-d_{\mathrm{p}}}\right)^2\right]^{-1}M^2 \quad 6.12$$

and the Forchheimer drag coefficient,

$$\beta(r)=\frac{1-\varepsilon_r}{{\varepsilon_r}^3}\frac{\rho_{\mathrm{g}}}{d_{\mathrm{p}}}\left[1.3\left(\frac{1-\bar{\varepsilon}}{\bar{\varepsilon}}\right)^{1/3}+0.03\left(\frac{d_{\mathrm{bed}}}{d_{\mathrm{bed}}-d_{\mathrm{p}}}\right)^2\right]\frac{1}{M} \quad 6.13$$

as functions of the local porosity. Here, M is termed the modification factor and is a function of the average bed porosity and the pellet-to-bed diameter ratio defined as

$$M=1+\frac{2}{3}\frac{1}{1-\bar{\varepsilon}}\frac{d_{\mathrm{p}}}{d_{\mathrm{bed}}}. \quad 6.14$$

6.2.3 Conservation of energy

Separate energy balance equations for the gas, adsorbent, and canister wall are included in the model to account for local thermal nonequilibrium. The gas-phase energy balance accounts for transient energy storage, conduction, convection, and heat transfer with the neighboring sorbent as

$$\varepsilon_r \rho_{\mathrm{g}} c_{p,\mathrm{g}} \frac{\partial T_{\mathrm{g}}}{\partial t} = \nabla \cdot \left(\mathbf{k}_{\mathrm{eff}} \nabla T_{\mathrm{g}} \right) - \rho_{\mathrm{g}} c_{p,\mathrm{g}} \mathbf{u} \cdot \nabla T + \frac{A_{\mathrm{s}}}{V_{\mathrm{bed}}} h_{\mathrm{g-s}} \left(T_{\mathrm{s}} - T_{\mathrm{g}} \right) \tag{6.15}$$

where A_s/V_{bed} is the specific surface area of the adsorbent pellets. The interfacial gas-sorbent heat transfer coefficient, $h_{g–s}$, is predicted from the empirical correlation of Wakao *et al.*[88]. The effective axial thermal conductivity accounts for both the sorbent- and gas-phase conductivities as well as axial thermal dispersion due to mixing. As the fluid flow is anisotropic, the effective thermal conductivity is expressed as a tensor

$$\mathbf{k}_{\mathrm{eff}} = \begin{bmatrix} k_{\mathrm{eff,r}} & 0 \\ 0 & k_{\mathrm{eff,ax}} \end{bmatrix} . \tag{6.16}$$

The effective axial and radial thermal conductivity coefficients are calculated from the correlation of Cheng *et al.* [168] as

$$k_{\mathrm{eff,r}} = k_{\mathrm{g}} \left(\frac{k_{\mathrm{eff}}^{0}}{k_{\mathrm{g}}} + 0.12 PrRe_{\mathrm{p}} \frac{|\mathbf{u}|}{\bar{u}_{\mathrm{s,in}}} \left[1 - e^{-y/d_{\mathrm{p}}} \right] \right) \tag{6.17}$$

and Yagi *et al.* [90] as

$$k_{\mathrm{eff,ax}} = k_{\mathrm{g}} \left(\frac{k_{\mathrm{eff}}^{0}}{k_{\mathrm{g}}} + 0.75 PrRe_{\mathrm{p}} \right) \tag{6.18}$$

where k_g is the gas thermal conductivity, $\bar{u}_{s,in}$ is the mean superficial velocity at the bed inlet, y is the distance from the wall, and k_{eff}^{0} is the effective axial thermal conductivity of a quiescent bed of spherical particles predicted using the Krupiczka [91] equation. All these input parameters are calculated using the dimensionless Reynolds and Prandtl numbers defined in the *Nomenclature* section.

The sorbent-phase energy balance accounts for transient storage, convective heat loss to the gas, and the heat of adsorption as

$$(1-\varepsilon)\rho_{\text{env}}c_{p,\text{s}}\frac{\partial T_{\text{s}}}{\partial t}=\frac{A_{\text{s}}}{V_{\text{bed}}}h_{\text{g–s}}\left(T_{\text{g}}-T_{\text{s}}\right)-(1-\varepsilon)\lambda\frac{\partial n}{\partial t}\ . \qquad 6.19$$

The isosteric heat of adsorption, λ, is derived as a function of adsorbate partial pressure and sorbent temperature using the Clausius−Clapeyron relationship [129]. The canister wall energy balance is simply

$$A_{\text{can}}\rho_{\text{can}}c_{p,\text{can}}\frac{\partial T_{\text{can}}}{\partial t}-A_{\text{can}}k_{\text{can}}\frac{\partial^2 T_{\text{can}}}{\partial z^2}=0\ . \qquad 6.20$$

6.2.4 Initial and boundary conditions

The model uses a constant inlet mole fraction and a zero-concentration-gradient outlet,

$$x|_{z=0}=x_0,\quad \left.\frac{\partial c}{\partial z}\right|_{z=L}=0 \qquad 6.21,6.22$$

The bed is assumed to contain no adsorbate at the start of breakthrough and the fluid to be stagnant. The superficial velocity at the inlet is linearly ramped from 0 to 0.23 m/s over a one-second period to improve model convergence. The velocity is maintained at 0.23 m/s for the remainder of the simulation. To match experimental conditions [160], the temperature at the inlet of the bed is fixed at 25 °C and the pressure at the exit of the bed is fixed at 111 kPa, throughout the simulation. A convection boundary condition is used to model heat transfer between the gas-phase and wall,

$$k_{\text{can}}\left.\frac{\partial T_{\text{can}}}{\partial r}\right|_{r=r_{\text{bed}}}=-k_{\text{eff,r}}\left.\frac{\partial T_{\text{g}}}{\partial r}\right|_{r=r_{\text{bed}}}=h_{\text{g–can}}\left(T_{\text{g}}-T_{\text{can}}\right) \qquad 6.23$$

using the empirical correlation from Li and Finlayson [89] to predict the gas–canister convection coefficient, $h_{\text{g–can}}$. Heat transfer between the wall ambient and ambient is modeled as

$$k_{\text{can}}\left.\frac{\partial T_{\text{can}}}{\partial r}\right|_{r=r_{\text{can,out}}/2}=\frac{1}{R'_{\text{can–amb}}}\left(T_{\text{amb}}-T_{\text{can}}\right) \qquad 6.24$$

where the thermal resistance between the canister and ambient was found by calibration [160] to be $R'_{\text{can–amb}}$ = 3.82 K/(m W). The walls of the sorbent bed, the bottom boundary of the gas-phase, and the top and bottom boundaries of the canister wall are all assumed to be adiabatic. In addition, radial symmetry is enforced at the centerline and there is no mass flux across the wall of the canister.

6.2.5 Solution procedure

The governing equations (Eqs. 6.1–6.20) are coupled and solved in COMSOL Multiphysics [126]. The properties of the gas mixture are computed using the ideal gas assumption and accounting for local temperature, pressure, and composition [87]. An axisymmetric, two-dimensional mesh of triangular elements is generated with a maximum element size of 3 mm in the center of the bed and reducing to 1 mm at the boundary between the canister wall and bed. The cansiter wall is also meshed with triangular elements reducing from 3 mm at the outside edge of the canister wall to 1 mm at the gas-canister interface. The elements in both domains are nearly equiangular with an average element quality = 0.88, and minimum quality = 0.34 based on a skewness metric. Additionally, a 12-element thick boundary layer region is added in the gas/sorbent bed domain at the wall, which extends 2 mm into the bed (*i.e.*, one pellet diameter from the wall) to better capture the sharp velocity and concentration gradients in the near-wall region. These element sizes, resulting in a mesh containing a total of 46,000 elements, were selected based on a mesh refinement study. The Newton automatic highly nonlinear method was used to solve coupled-nonlinear equations. The solver uses the backward differentiation formula to dynamically modify the time step and reduce computation time; we impose an initial time step of 1×10^{-8} s to improve stability. Convergence is reached when the relative residuals drop below 10^{-4} for all dependent variables, namely, the adsorbate concentration in the gas and adsorbed phases, pressure, and temperatures.

6.3 Results

Experimental results for the breakthrough of carbon dioxide (CO_2) and water (H_2O) on zeolite 13X are presented. Comparison of these two adsorbates is used to illustrate that the adsorbate/adsorbent pairing affects the radial variation in concentration. The effect of radial variations in porosity on the velocity profile is then described. The 2-D simulation results are validated against the experimental data for H_2O breakthrough and compared to 1-D results to illustrate the need to account for these radial variations. The validated 2-D model is then used to investigate which kinetic and equilibrium parameters cause H_2O to exhibit more significant radial variations in concentration compared to CO_2.

6.3.1 Experimental breakthrough tests for CO_2 and H_2O on zeolite 13X

Experimental breakthrough data are for CO_2 and H_2O adsorption in a fixed-bed of zeolite 13X with d_{bed}/d_p = 48, at an inlet temperature of 25 °C and a superficial velocity of 0.23 m/s, were originally published by Son *et al.* [160] and are reproduced here, to illustrate the different behavior of these two adsorbates. To enable direct comparison between the two adsorbates, Figure 6.1 plots the normalized concentration against the nondimensional time,

$$\bar{t} = \frac{t}{t_{stoich}} \tag{6.25}$$

where the stoichiometric time [167] is defined using the mixed-exit concentration as

$$t_{stoich} = \int_0^\infty \left(1 - \frac{x_{ME}}{x_0}\right) dt \ . \tag{6.26}$$

The normalized concentration is plotted for the centerline measurement (6-mm from the end of the sorbent bed) and the mixed-exit location downstream of the bed. Initially the adsorbate mole fraction is zero at both locations. As the the experiment progresses and the pellets become saturated, the adsorbate penetrates further into the bed, until it eventually reaches the end of the bed. At this time (*i.e.*, $t = t_b$) the concentration of adsorbent in the effluent starts to rise until the bed becomes completely saturated and the effluent concentration exactly matches the influent concentration (*i.e.*, x/x_0=1).

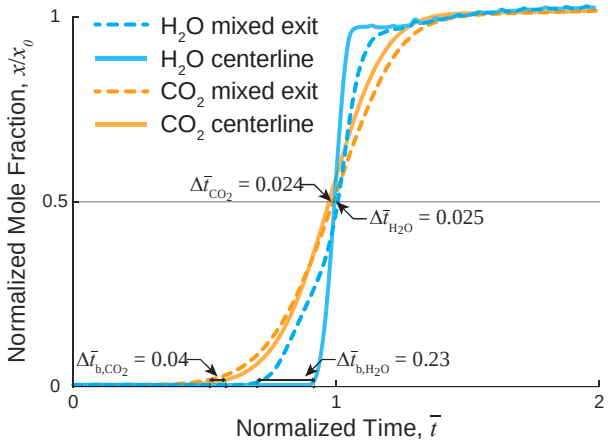

Figure 6.1. Comparison of normalized experimental breakthrough curves for CO_2 and H_2O on zeolite 13X adapted from Son *et al.*[160] Breakthrough curves measured at the mixed-exit and centerline locations are shown as dashed and solid lines, respectively.

Comparison of the centerline and mixed-exit breakthrough curves provides insight into the nonplug-flow behavior in the beds. The offset between the centerline and mixed-exit curves at the midpoint ($x/x_0 = 0.5$) is independent of adsorbate, which indicates that the mechanical dispersion mechanisms are the same for H_2O and CO_2 breakthrough as described in Son *et al.*[160] Further insight can be gleaned by examining the breakthrough time. The mixed-exit curve breaks through before the centerline for both adsorbates, indicating the presence of wall channeling. Notably, the discrepancy between the centerline and mixed-exit initial breakthrough times is significantly more pronounced for H_2O than for CO_2 breakthrough ($\Delta \bar{t}_b = 0.04$for CO_2 versus $\Delta \bar{t}_b = 0.23$ H_2O), even though breakthrough tests were conducted under identical flow conditions (see Table 5.2). This observation motivates the use of a 2-D model to investigate what causes this discrepancy between the mixed-exit and centerline breakthrough behavior.

6.3.2 2-D model validation and comparison

The 2-D, axisymmetric model developed in Section 6.2 can directly predict the effects of radial variations in porosity, without depending upon apparent dispersion parameters. We use this model to simulate the water breakthrough experiments from Son *et al.*[160] The predicted normalized mixed-exit concentration from the 2-D axisymmetric model is plotted as a function of time in Figure 6.2 along with experimental measurements and predictions from a 1-D model [160]. The 2-D model better predicts the experimental data than the 1-D model, as is further described below.

The 2-D model predicts breakthrough ($t_b = 2.5$ h) within minutes of the experimentally measured initial breakthrough time ($t_b = 2.6$ h), while the 1-D model predictions were off by one-hour ($t_b = 3.6$ h). The initial breakthrough time determines when a bed will be switched from adsorption to desorption operation in gas-separation systems; it is therefore critical to accurately predict t_b when designing a separations system. The excellent breakthrough prediction provided by the 2-D model is noteworthy considering the assumed spatial distribution of porosity and other model input parameters. The 2-D model continues to match the experimental breakthrough curve well during the initial rise (*i.e.*, $t < 4$ h) but begins to rise more steeply than the experimental curve as the bed approaches saturation at $t > 4$ h; this period of operation is of lesser concern to system designers.

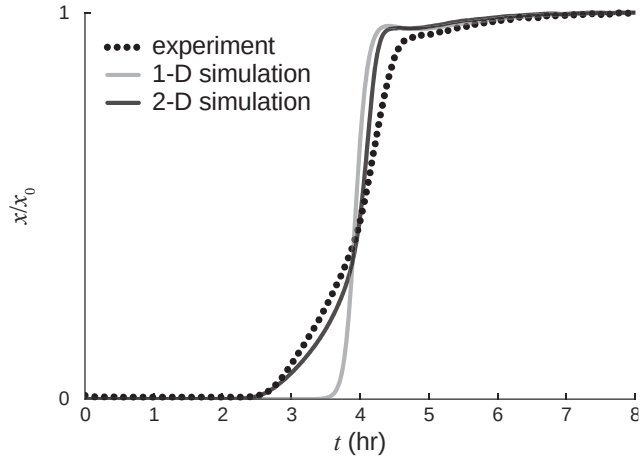

Figure 6.2. Comparison of 1-D[160] and 2-D simulation predictions to experimental measurements of the mixed-exit concentration during water breakthrough on zeolite 13X.

When a bed is confined in a rigid container, the pellets pack less efficiently near the wall, leading to a higher local porosity. The effects of these packing heterogeneities on hydrodynamics can be captured by a 2-D model where the bed permeability is described as a function of local porosity as described in Section 6.2.2. The local porosity (as described by Eq. 6.2) and interstitial axial velocity averaged over the entire duration of the H_2O breakthrough simulation are plotted in Figure 6.3. The left panels of Figure 6.3 plot these variations over the entire width of the bed as a function of normalized, radial distance from the centerline, while the right panels zoom in on the boundary-layer region (within two pellet-diameters of the wall). Note that though the velocity profile is time averaged, minimal temporal variations were observed and the results in Figure 6.3 are indicative of the velocity at any given time step. Notice that the porosity reaches a constant value within approximately one pellet diameter from the wall (upper right panel). The velocity at the wall is constrained to zero by the no-slip boundary condition but peaks at a radial distance from the wall of $0.06 \times d_p$ due to the increased permeability in the near-wall region.

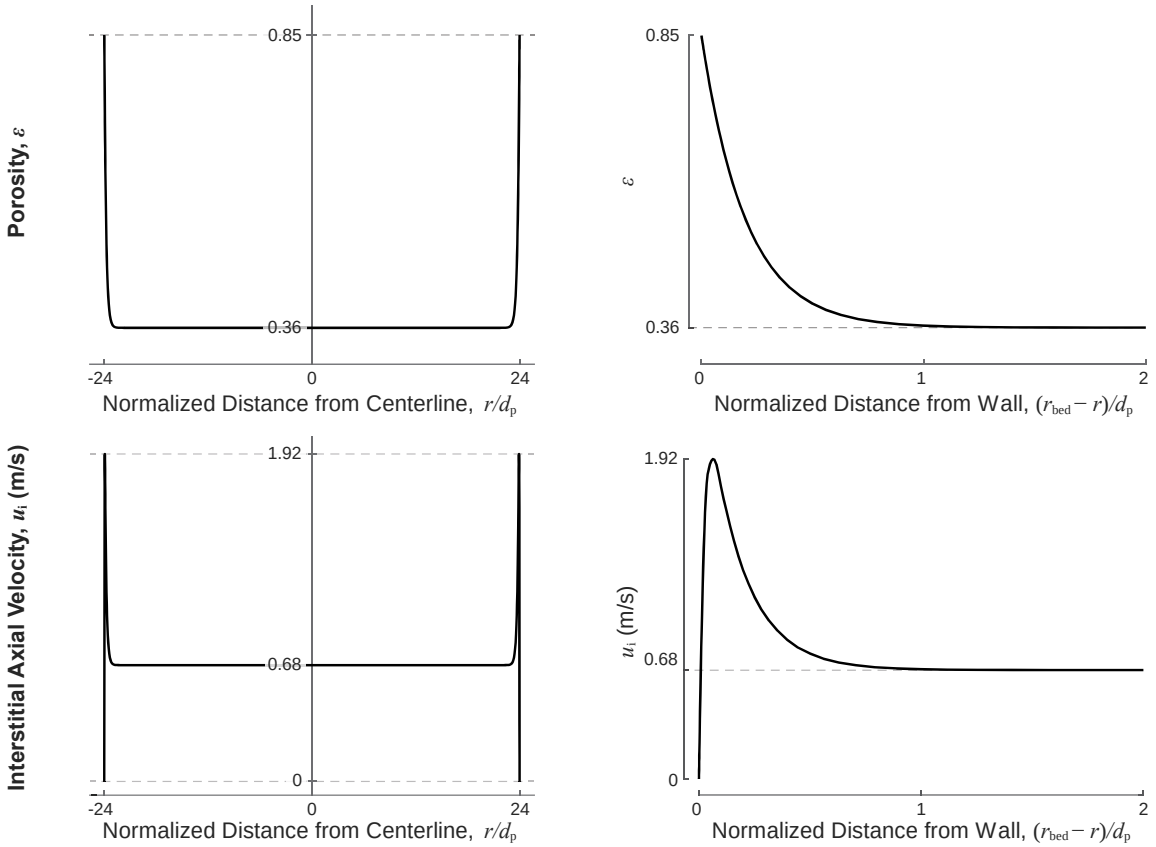

Figure 6.3. Radial variation of porosity (top) and velocity (bottom) in the fixed-bed adsorber during water breakthrough. The left panels show variation across the entire bed while the right panels show a close up of the variation within two pellet diameters from the wall.

The error in the 1-D, plug-flow model predictions is revealed to be a direct consequence of wall-channeling effects. We examine gas-phase concentration profiles from both the 1-D and 2-D models at several time steps during breakthrough as shown in the upper and lower panels of Figure 6.4, respectively. In discussing these plots, we define the mass transfer zone (MTZ) as the region where $0.1 < x/x_0 < 0.9$, *i.e.*, where there is a steep concentration gradient indicating the occurrence of adsorption. The leading and trailing edges of the MTZ are indicated on the contour plots of Figure 6.4 with black and white dashed lines, respectively.

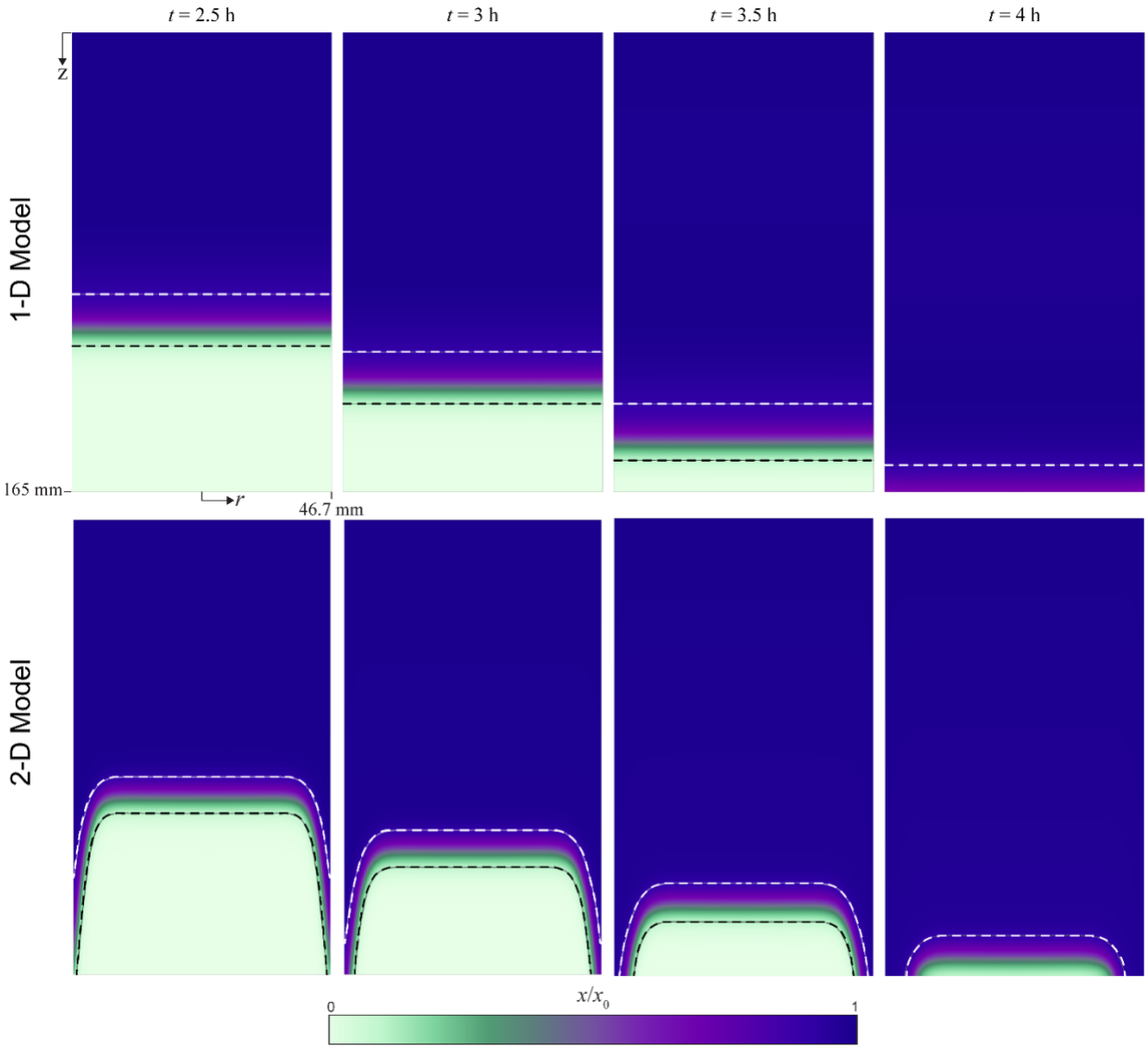

Figure 6.4. Spatial distribution of the normalized mole fraction of H_2O (x/x_0) during breakthrough in a bed of zeolite 13X as predicted the 1-D model [160] (top panels) and 2-D model (bottom panels).

The 2-D model results clearly show H_2O penetrates deeper into the bed near the walls where the interstitial flow is fastest and there is less capacity, effects of inefficient pellet packing adjacent to the rigid container walls as described above. This radial variation in concentration results in earlier breakthrough near the periphery of the bed and delayed the breakthrough at the bed centerline. Because breakthrough in the 2-D model initially occurs at the far edges of the bed and then progresses steadily inward, this results in a gradual rise in the mixed-exit concentration as is seen for both the 2-D simulation and experimental curves in Figure 6.2. Eventually, the core of MTZ

reaches the bed exit, causing a sharp rise in effluent concentration which is seen as an inflection point in the 2-D simulation breakthrough curve shortly before 4 h. Because the 1-D model assumes radially uniform velocity and porosity (*i.e.*, capacity), the water concentration is only a function of time and axial position. Thus, the front advances uniformly across the bed with time, and there is no early breakthrough at the periphery. The mixed-exit concentration predicted by the 1-D model is incapable of capturing this early breakthrough near the edge of the bed.

Further insight can be gleaned by comparing the behavior of the 1-D and 2-D models as the bed approaches saturation. Notice that the 1-D and 2-D predictions of the mixed-exit concentration in Figure 6.2 run parallel for t >4 h. This can be explained by the concentration profiles in Figure 6.4. The flat concentration profiles for the 2-D model at the centerline indicate that flow in the middle of the bed is unaffected by the faster flow near the walls. Consequently, the concentration profiles in the center are only a function of the axial dispersion and mass transfer rate (*i.e.*, the same mechanisms that control dispersion in the 1-D model). This result indicates that the flow at the centerline can be approximated as independent of wall effects and thus nearly one-dimensional.

Even though the high porosity/velocity region is very small—only extending roughly $1\times d_p$ from the wall, as shown in Figure 6.3—it can have a large effect on the breakthrough dynamics, as demonstrated in Section 5.3.1. Wall-channeling effects are frequently ignored, and the flow is assumed to be one-dimensional to reduce computational costs. While 1-D simulations cannot directly model wall-channeling, some authors attempt to account for wall-channeling in a 1-D model by using an apparent axial dispersion coefficient that is calibrated to the specific system of interest.[15] We showed in the previous chapter [160] that this method fails to capture the breakthrough behavior when nonplug-flow conditions prevail in the bed and that nonplug-flow effects can be significant even in very large beds ($d_{bed}/d_p = 48$) for which the prevailing consensus in the literature states that wall effects should be negligible. It is therefore critical to further investigate what causes the plug-flow assumption to fail and revise the guidelines for when wall effects can be neglected.

6.3.3 Effect of capacity & adsorption kinetics

The validated 2-D model is used to explain why wall channeling effects are more pronounced for H_2O breakthrough than CO_2 breakthrough on zeolite 13X. In the previous chapter [160], we hypothesized that the difference is caused by the interplay between wall channeling and the capacity and kinetics of the adsorbate/adsorbate pairing. Zeolite 13X has a greater affinity for H_2O than CO_2; the equilibrium capacity of 13X for H_2O is approximately ten times greater than that of CO_2 at the same temperature and adsorbate partial pressure.[129], [139] H_2O also adsorbs more rapidly than CO_2 reflected by its greater mass transfer coefficient [160] (see Table 6.2).

To determine how these parameters affect breakthrough in the presence of wall-channeling, we changed n^* and k_0 for H_2O in the adsorption model to match n^* and k_0 values for CO_2. After running the baseline 2-D simulation for H_2O breakthrough as described in Section 6.3.2, we run the model with the capacity decreased by 90% (*i.e.*, n^*_{in} = 1.5 mol/kg) while all other parameters remain unchanged from their definitions in Section 6.2. Then we run the model with the mass transfer coefficient reduced by 70% and 90% (*i.e.*, k_0 = 51 s^{-1} and 17 s^{-1}) again with all other parameters, including capacity, unchanged. Results from these four simulations are presented in Figure 6.5. The top panels of Figure 6.5 show the gas-phase mole fraction of H_2O at the point of breakthrough (x_{ME}/x_0 = 0.01);e the lower panels plot the nondimensional breakthrough curve predicted by each 2-D simulation alongside predictions from a 1-D model [160] for the same conditions.

Looking at the left-most two panels, we see that the low-capacity simulation is very similar to the baseline. Thus, we conclude that the adsorbent capacity has little effect on the nondimensional initial breakthrough time. Furthermore, because both the baseline and low-capacity 2-D simulations therefore have the same deviation from their 1-D counterparts, this indicates that the magnitude of wall-channeling effects is insensitive to the adsorbate capacity.

The mass transfer coefficient has a more significant impact on the nondimensional breakthrough curves than the capacity. The flow becomes increasingly dispersed in the axial direction as the mass transfer coefficient decreases. This can be observed by considering the mass-transfer zone (MTZ) in the top panels of Figure 6.5 . We see that the MTZ at the bed centerline expands from 8% of the total bed length for the baseline simulation (k_0 = 170 s^{-1}) to 55% when k_0 is reduced to

17 s^{-1}. This behavior is in accordance with prior studies which found that the MTZ length is a function of the adsorption rate, axial dispersion, and the flow rate.[175] Notably, the 1-D model predictions begin to approach the 2-D model as k_0 decreases, as can be seen in the bottom panels of Figure 6.5. This is due to the increasing axial dispersion—from increased mass transfer resistance—which begins to overpower the effects of wall channeling. Conversely, the effects of wall-channeling are exacerbated for adsorbate/adsorbent pairings with high mass transfer coefficients. These results explain why a 1-D model can accurately predict the initial breakthrough time of CO_2—which has high mass transfer resistance—but drastically fails to predict the initial breakthrough time of H_2O at the same flow rate and in the same bed.

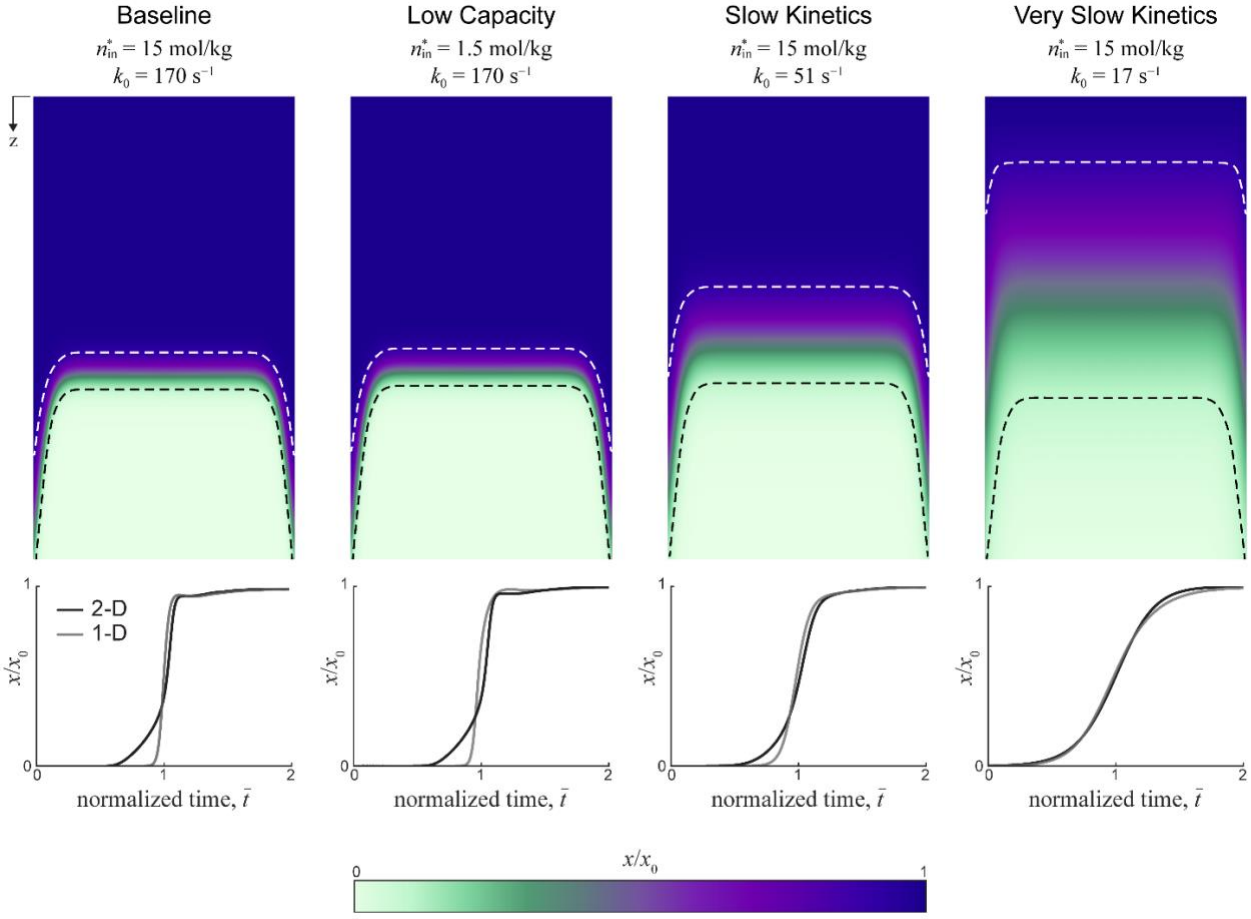

Figure 6.5. Effect of capacity and kinetics on the gas-phase mole fraction of H_2O at breakthrough in a bed of zeolite 13X. The baseline, 2-D simulation is compared against simulations where either the capacity (n^*) or the mass transfer coefficient (k_0) is modified while fixing all other parameters.

6.4 Conclusions

This chapter investigated the effect of adsorption kinetics and capacity on breakthrough behavior in confined geometries where wall-channeling effects cause spatial variations in the velocity. We summarized our previous experimental measurements [160] which showed an unexpected discrepancy between the breakthrough behavior of H_2O and CO_2 on zeolite 13X. While CO_2 breakthrough could be approximated using a 1-D plug flow adsorption model, H_2O breakthrough showed significant deviations from plug-flow predictions. To explain, we developed a 2-D model which accounts for inefficient packing of the sorbent pellets near the walls. The effect of the resulting porosity variations on velocity and concentration profiles were then described for H_2O breakthrough in a cylindrical bed with $d_{bed}/d_p = 48$, and the 2-D model was validated by comparing the predicted mixed-exit breakthrough curve to experimental data. The 2-D model showed excellent agreement with experimental data, especially at the point breakthrough, which is of paramount importance when designing an adsorbent system. The 2-D results were then compared against a 1-D model that was shown to be inadequate for describing water adsorption on zeolite 13X due to neglecting the wall-channeling effects. Notably, the 1-D model yielded almost a 40% error in the initial breakthrough time compared to experimental measurements (~1 h difference).

The validated 2-D model was then used to investigate the effect of adsorption equilibrium capacity and kinetics on the breakthrough behavior. Varying the capacity had little effect on the predicted nondimensional breakthrough curve and severity of wall-channeling effects. In contrast, as the mass transfer coefficient decreased, the increased resistance to adsorption caused a significant increase in the thickness of the mass-transfer zone. Ultimately, the 1-D and 2-D model converge when the mass-transfer resistance is sufficiently large (*i.e.*, low k_0), resulting in high axial dispersion that masks the effects of wall channeling. Our results indicate that wall-channeling effects cannot be assumed negligible based simply on a bed-to-pellet diameter criterion, but rather one must also consider the adsorption kinetics. Thus, while wall-channeling effects may be deemed negligible for a system when the k_0 value is sufficiently low, they may not be negligible for this same system if the adsorbate and/or adsorbent is changed. In conclusion, this study shows how the plug-flow assumption can break down—even for large beds ($d_{bed}/d_p = 48$)—and highlights the need to consider adsorption kinetics in addition to the traditional d_{bed}/d_p criteria when assessing the validity of the plug-flow assumption.

7. CONCLUSIONS AND FUTURE WORK

The principle objective of this dissertation was to improve the predictive capabilities of fixed-bed adsorption models and clarify the limitations of the commonly used plug-flow assumption. The work included rigorous examination of the sensitivities and uncertainties of these models, extensive experimental validation (Chapter 2), improved measurement sensitive model inputs (Chapters 3–4), and finally a tandem numerical/experimental study of the effects of plug-flow in confined geometries (Chapters 4–5). In addition to enhancing our fundamental understanding of dispersive mechanisms in fixed-beds, this work has shown many practical outcomes for improving the fidelity of models used to design the next-generation atmospheric revitalization system for humans' journey to Mars.

The primary conclusions from each preceding chapter are summarized below, followed by an outline of potential investigations for future work.

7.1 Conclusions

In Chapter 2, an axially dispersed plug-flow model is developed and calibrated to experimental data. The uncertainty of the calibrated model is then quantified based on a systematic investigation of uncertainties in an *ad hoc* prediction of effective transport properties using available correlations compared to experimental data from the literature. The most sensitive model inputs are identified, as are the uncertainties that they are expected to induce in model predictions. Note that capacity—which is well known to be a sensitive parameter—was not considered in this analysis. This work is the first such formal assessment of the uncertainty of a fixed-bed adsorption model due to the practical uncertainties associated with these model inputs.

- A thorough review of the literature was performed to quantify the uncertainty of model inputs. Uncertainty bounds for these inputs with a 95% confidence interval were presented.
- The model is most sensitive to the mass transfer coefficient, porosity, and sorbent density.
- *Ad hoc* prediction of axial dispersion can lead to large errors in the predicted breakthrough time when wall-channeling dominates the apparent axial dispersion.
- It is vital to precisely know density and porosity to which the model is highly sensitive.

The work in subsequent chapters are informed by the results of the uncertainty analysis in Chapter 2, and efforts are focused on improving measurement/knowledge of highly sensitive parameters.

Chapters 3 and 4 present and analyze experimental isotherm and heat-of-adsorption data for CO_2 and H_2O on zeolite 13X, respectively. These two adsorption material sets are of broad technological interest and the experimental isotherm data presented in this dissertation reconciles errors in previously published isotherms. Chapter 3 also presents never-before measured heat-of-adsorption values for CO_2 adsorption on 13X. In addition to providing novel data, these chapters include in-depth discussion of experimental techniques and a comprehensive comparison to extant data to identify common errors in the experimental methods used to acquire isotherms. Both chapters also include details on the development of empirical fits of known isotherm models to these new data.

- Inadequate activation temperature was shown to be the source of discrepancies amongst previously published isotherm data. Zeolite 13X must be activated at or above 350 °C to completely remove residual water loading prior to measuring isotherm data.
- Isotherms for CO_2 adsorption were measured at ten temperatures from 0 °C to 200 °C and at equilibrium pressures ranging from 0.001 kPa to 100 kPa.
- Isotherms for H_2O adsorption were measured at 25 °C, 35 °C, 50 °C, 70 °C, and 100 °C and at equilibrium pressures ranging from 0.006 kPa to 25 kPa.
- Heats of adsorption for CO_2 on zeolite 13X were also measured at nine temperatures from 10 °C to 200 °C using a thermogravimetric, differential scanning calorimeter (TG-DSC).
- The 2-site Langmuir model with constant saturation capacity (commonly known as the dual-site Langmuir) provided the best agreement with both isotherm and heat of adsorption measurements for CO_2 on zeolite 13X.
- The Sips isotherm model modified by the Aranovich–Donohue equation provided the best agreement with isotherm measurements for H_2O on zeolite 13X.

Chapter 5 investigates the effect of geometric confinement on apparent axial dispersion in fixed-bed adsorption systems using experimental measurements and an axially dispersed plug-flow model similar to the one developed in Chapter 2. The 1-D model is used to independently extract mass transfer and axial-dispersion coefficients from breakthrough experiments via centerline and

mixed-exit concentration measurements, respectively. Four experimental cases are considered: breakthrough of carbon dioxide (CO_2) and water (H_2O), in two cylindrical beds of zeolite: one with a small bed-to-pellet diameter ($d_{bed}/d_p = 17$) and a second, significantly larger bed ($d_{bed}/d_p = 48$).

- Neglecting the effects of confinement can lead to large errors (500%) in mass transfer coefficient extracted using traditional methods (*i.e.*, fitting to downstream mixed-exit data).
- Conversely, that mass transfer coefficient can be extracted from centerline breakthrough curves with good accuracy even when nonplug-flow conditions prevail.
- Wall channeling effects were observed to be significant even at $d_{bed}/d_p = 48$. This is in stark contrast to the prevailing consensus in the literature, which states that wall effects as negligible for beds with $d_{bed}/d_p \geq 20$.
- *A priori* predictions of axial dispersion from existing correlations—which do not account for the effects of confinement—grossly underpredict the apparent axial dispersion in confined geometries. As a result, the breakthrough time predicted using a 1-D model was found to be incorrect by as much as 1-hour (compared with experimental measurements).
- Furthermore, the degree to which the 1-D model predictions deviated from experimentally observed breakthrough was a strong function of the adsorbent/adsorbate pair with H_2O showing significant greater wall-effects compared to CO_2 even though experiments for both adsorbates were run with identical flow conditions.
- Ultimately, the axially disperse plug-flow model fails to capture the physics of these fixed-bed adsorption when nonplug-flow conditions prevail.

Chapter 6 describes a 2-D model that was developed to explore the effect adsorption kinetics and equilibrium have on breakthrough behavior and explain the discrepancy between the breakthrough behavior of H_2O and CO_2 observed in the previous chapter. The 2-D model was described in detail then validated against experimental data. The validated 2-D model was then used to investigate the effect of adsorption equilibrium and kinetics on the breakthrough behavior.

- The 2-D model showed excellent agreement with experimental data, especially at the start of breakthrough which is of paramount importance when designing an adsorbent system.
- Wall effects are a direct function of porosity variation in the near-wall region.

- The adsorbent's capacity had little effect on the predicted, nondimensional breakthrough curve. In contrast, the model results were very sensitive to mass transfer coefficient.
- As the mass transfer coefficient decreased, the increased resistance to adsorption caused a proportionate increase in the mass-transfer zone thickness. 1-D and 2-D model results converge when the mass transfer resistance is large enough to obviate effects of wall channeling.
- Wall-channeling effects cannot be assumed negligible based purely on a bed-to-pellet diameter criterion; adsorption kinetics must also be considered when assessing the validity of the plug-flow assumption.

7.2 Suggestions for future work

Plans for potential future studies are proposed in this section. The overall goal of the proposed investigations is to further improve the predictive capabilities of fixed-bed absorption models and to further enhance our understanding of the plug-flow assumption's range of viability.

7.2.1 Improvements for fixed-bed adsorption models

The work presented in this dissertation is limited to the first half of an adsorption/desorption cycle. Similar work should be completed to evaluate model accuracy during desorption. First, a sensitivity and uncertainty analysis should be performed for desorption under the heating and pressure conditions expected in future life-support systems. It is expected that the model will be more sensitive to heat transfer parameters as the bed temperature increases. Furthermore, uncertainty in heat transfer parameters will become significant under near-vacuum conditions. Thus, additional efforts may be required to improve prediction of parameters such as effective thermal conductivity, heat transfer coefficients, or heat of adsorption. The sensitivity and uncertainty analysis should be used to guide such efforts to improve model accuracy so that efforts can be focused on improving knowledge of input parameters that control the overall model uncertainty.

7.2.2 Determining the plug-flow assumption's range of viability

This dissertation highlighted the paramount role wall-channeling effects can play in fixed-bed adsorption and showed that plug-flow cannot be assumed based purely on the size of a bed. Perhaps most concerning is the experimental evidence that the widely used plug-flow assumption can fail even at very large bed diameters. While the present work demonstrated that this failure could be predicted with a 2-D model, it is infeasible to presume that the modeling community will, or even, can perform high-order simulations of every system they consider. Thus, significant future work is needed to derive updated guidelines for determining when the plug-flow assumption is valid *a priori*. This work could include scaling analyses of the dispersive mechanisms in a fixed-bed adsorber, parametric studies with 2-D studies, or further experimental investigations. Ideally, a mechanistic model of axial dispersion due to wall channeling could be developed which would allow modelers to evaluate a system's conformity with the plug-flow assumption. There are currently no such models in the literature, and this is a necessary step to improving our understanding of wall-channeling on axial dispersion. This model will enable *a priori* determination of when the effects of wall-channeling on axial dispersion must be considered without requiring costly and time-consuming experiments and/or high-order simulations.

APPENDIX A. CO_2 HEAT OF ADSORPTION DATA

Table A1. Calorimetrically measured heat of adsorption of CO_2 on zeolite 13X (10 °C, 25 °C, and 50 °C)

	10 °C		25 °C		50 °C	
	n mol/kg	H_a kJ/mol	n mol/kg	H_a kJ/mol	n mol/kg	H_a kJ/mol
50 mL/min	1.73 ± 0.047	38.9 ± 2.2	1.33 ± 0.047	40.8 ± 2.5	0.76 ± 0.046	42.6 ± 3.3
	2.11 ± 0.047	37.4 ± 2	1.64 ± 0.047	40.1 ± 2.3	1.04 ± 0.047	42.0 ± 2.8
	2.49 ± 0.048	37.3 ± 2	2.01 ± 0.048	39.2 ± 2.1	1.36 ± 0.047	41.3 ± 2.5
	2.98 ± 0.048	36.4 ± 1.9	2.46 ± 0.048	38.2 ± 2	1.74 ± 0.047	40.5 ± 2.3
	3.50 ± 0.049	35.6 ± 1.8	2.99 ± 0.049	37.3 ± 1.9	2.20 ± 0.048	39.6 ± 2.1
	3.81 ± 0.049	35.3 ± 1.8	3.31 ± 0.049	36.8 ± 1.9	2.50 ± 0.048	39.0 ± 2.1
	4.01 ± 0.049	35.0 ± 1.8	3.54 ± 0.049	36.5 ± 1.9	2.73 ± 0.049	38.6 ± 2
	4.16 ± 0.05	34.9 ± 1.8	3.71 ± 0.049	36.3 ± 1.9	2.91 ± 0.049	38.3 ± 2
150 mL/min	1.27 ± 0.069	39.2 ± 2.9	0.91 ± 0.069	40.5 ± 3.6	0.39 ± 0.069	40.3 ± 7.2
	1.55 ± 0.07	38.1 ± 2.5	1.18 ± 0.07	39.7 ± 3	0.60 ± 0.069	40.0 ± 4.9
	1.87 ± 0.07	37.3 ± 2.3	1.48 ± 0.07	39.1 ± 2.7	0.86 ± 0.069	40.3 ± 3.8
	2.26 ± 0.071	36.6 ± 2.1	1.83 ± 0.071	38.4 ± 2.4	1.15 ± 0.07	40.3 ± 3.1
	2.73 ± 0.072	35.8 ± 2	2.25 ± 0.071	37.6 ± 2.2	1.50 ± 0.07	40.1 ± 2.7
	3.03 ± 0.072	35.4 ± 1.9	2.54 ± 0.072	37.2 ± 2.1	1.72 ± 0.071	39.8 ± 2.5
	3.25 ± 0.073	35.1 ± 1.9	2.75 ± 0.072	36.9 ± 2.1	1.90 ± 0.071	39.6 ± 2.4
	3.42 ± 0.073	35.0 ± 1.9	2.92 ± 0.072	36.6 ± 2	2.04 ± 0.071	39.4 ± 2.4

Table A2. Calorimetrically measured heat of adsorption of CO2 on zeolite 13X (75 ℃, 100 ℃, and 125 °C)

	75 °C		100 °C		125 °C	
	n	H_a	n	H_a	n	H_a
	mol/kg	kJ/mol	mol/kg	kJ/mol	mol/kg	kJ/mol
50 mL/min	0.34 ± 0.046	42.4 ± 6.2	0.14 ± 0.046	39.6 ± 12.7	34.7 ± 19.4	34.7 ± 19.4
	0.53 ± 0.046	41.8 ± 4.2	0.25 ± 0.046	39.1 ± 7.5	32.5 ± 10.6	32.5 ± 10.6
	0.80 ± 0.047	41.7 ± 3.2	0.41 ± 0.046	39.8 ± 4.9	33.7 ± 6.8	33.7 ± 6.8
	1.12 ± 0.047	41.7 ± 2.7	0.64 ± 0.046	40.3 ± 3.5	36.3 ± 4.8	36.3 ± 4.8
	1.51 ± 0.047	41.2 ± 2.4	0.96 ± 0.047	41.0 ± 2.8	38.5 ± 3.6	38.5 ± 3.6
	1.77 ± 0.048	40.7 ± 2.3	1.18 ± 0.047	40.9 ± 2.6	39.0 ± 3.1	39.0 ± 3.1
	1.97 ± 0.048	40.4 ± 2.2	1.35 ± 0.047	40.8 ± 2.5	39.2 ± 2.8	39.2 ± 2.8
	2.13 ± 0.048	40.0 ± 2.2	1.49 ± 0.047	40.6 ± 2.4	39.3 ± 2.7	39.3 ± 2.7
150 mL/min	0.16 ± 0.068	34.9 ± 14.9	0.09 ± 0.068	25.9 ± 19.5	34.9 ± 29.2	34.9 ± 29.2
	0.27 ± 0.068	35.1 ± 9.1	0.15 ± 0.068	27.9 ± 12.5	33.0 ± 17.8	33.0 ± 17.8
	0.34 ± 0.046	42.4 ± 6.2	0.14 ± 0.046	39.6 ± 12.7	34.7 ± 19.4	34.7 ± 19.4
	0.53 ± 0.046	41.8 ± 4.2	0.25 ± 0.046	39.1 ± 7.5	32.5 ± 10.6	32.5 ± 10.6
	0.80 ± 0.047	41.7 ± 3.2	0.41 ± 0.046	39.8 ± 4.9	33.7 ± 6.8	33.7 ± 6.8
	0.34 ± 0.046	42.4 ± 6.2	0.14 ± 0.046	39.6 ± 12.7	34.7 ± 19.4	34.7 ± 19.4
	0.53 ± 0.046	41.8 ± 4.2	0.25 ± 0.046	39.1 ± 7.5	32.5 ± 10.6	32.5 ± 10.6
	0.80 ± 0.047	41.7 ± 3.2	0.41 ± 0.046	39.8 ± 4.9	33.7 ± 6.8	33.7 ± 6.8

Table A3. Calorimetrically measured heat of adsorption of CO_2 on zeolite 13X (150 ℃, 175 ℃, and 200 °C)

	150 °C		175 °C		200 °C	
	n	H_a	n	H_a	n	H_a
	mol/kg	kJ/mol	mol/kg	kJ/mol	mol/kg	kJ/mol
50 mL/min	0.05 ± 0.046	33.1 ± 28.8	0.04 ± 0.046	22.6 ± 26	0.07 ± 0.046	64.5 ± 40.9
	0.09 ± 0.046	30.9 ± 15.6	0.07 ± 0.046	19.9 ± 13.3	0.11 ± 0.046	61.0 ± 26.7
	0.15 ± 0.046	30.7 ± 9.7	0.11 ± 0.046	23 ± 9.9	0.14 ± 0.046	60.7 ± 20.3
	0.23 ± 0.046	32.5 ± 6.7	0.16 ± 0.046	27.1 ± 7.8	0.18 ± 0.046	58.5 ± 15.2
	0.36 ± 0.046	35.4 ± 4.9	0.24 ± 0.046	31.5 ± 6.2	0.23 ± 0.046	57.3 ± 11.6
	0.47 ± 0.047	36.7 ± 4	0.31 ± 0.046	33.3 ± 5.2	0.28 ± 0.046	55.4 ± 9.5
	0.56 ± 0.047	37.4 ± 3.6	0.38 ± 0.046	34.3 ± 4.5	0.32 ± 0.046	53.7 ± 8.1
	0.65 ± 0.047	37.7 ± 3.3	0.44 ± 0.047	34.9 ± 4.1	0.36 ± 0.046	52.4 ± 7.2
150 mL/min	0.05 ± 0.068	35.4 ± 49.6	0.04 ± 0.068	38.2 ± 67.5	0.03 ± 0.068	90.2 ± 203
	0.08 ± 0.068	32.9 ± 27.6	0.06 ± 0.068	43.8 ± 48.1	0.05 ± 0.068	81.4 ± 121
	0.12 ± 0.068	34.2 ± 19.6	0.09 ± 0.068	44.0 ± 33.7	0.06 ± 0.068	76.4 ± 86.5
	0.17 ± 0.068	34.2 ± 14	0.12 ± 0.068	43.7 ± 24.8	0.08 ± 0.068	74.9 ± 67.2
	0.23 ± 0.068	36.7 ± 11.2	0.15 ± 0.068	45.3 ± 20.1	0.09 ± 0.068	74.0 ± 53.5
	0.28 ± 0.068	38.0 ± 9.6	0.18 ± 0.068	46.0 ± 17.2	0.11 ± 0.068	73.9 ± 46.8
	0.32 ± 0.069	38.5 ± 8.4	0.21 ± 0.068	45.8 ± 15.1	0.12 ± 0.068	73.2 ± 41.7
	0.36 ± 0.069	38.9 ± 7.6	0.23 ± 0.068	45.3 ± 13.4	0.13 ± 0.068	72.4 ± 37.7

APPENDIX B. FITTED PARAMETERS FOR ALL CO_2 ISOTHERMS

Table B4. Parameters for the Langmuir model with constant saturation capacity for CO_2 adsorption on zeolite 13X (Grace Davidson, MS 544).

a_0, mol/kg	b_0, kPa^{-1}	E/R, K
4.960	1.1847×10^{-7}	4553

Table B5. Parameters for the Langmuir model with temperature-dependent saturation capacity for CO_2 adsorption on zeolite 13X (Grace Davidson, MS 544).

a_0, mol/kg	c_0, (mol K)/ kg	b_0, kPa^{-1}	E/R, K
0	1441	8.713×10^{-7}	4003

Table B6. Parameters for the Toth model with constant saturation capacity for CO_2 adsorption on zeolite 13X (Grace Davidson, MS 544).

$a_{0,j}$, mol/kg	$b_{0,j}$, kPa^{-1}	E/R, K	f_0	α
7.656	2.394×10^{-8}	5827	0.4962	-54.86

Table B7. Parameters for the Toth model with temperature-dependent saturation capacity for CO_2 adsorption on zeolite 13X (Grace Davidson, MS 544).

$a_{0,j}$, mol/kg	c_0, (mol K)/ kg	$b_{0,j}$, kPa^{-1}	E/R, K	f_0	α, K
6.780	239.8	2.451×10^{-8}	5815	0.52	-61.12

Table B8. Parameters for the 2-site Langmuir model with constant saturation capacity for CO_2 adsorption on zeolite 13X (Grace Davidson, MS 544).

j (site)	$a_{0,j}$, mol/kg	c_0, (mol K)/ kg	$b_{0,j}$, kPa^{-1}	E_j/R, K
1	0.7198	393.6	8.502×10^{-8}	5325
2	0.5577	873.9	1.450×10^{-6}	3250

Table B9. Parameters for the 3-site Langmuir model with constant saturation capacity for CO_2 adsorption on zeolite 13X (Grace Davidson, MS 544).

***j* (site)**	**$a_{0,j}$, mol/kg**	**$b_{0,j}$, kPa^{-1}**	**E_j/R, K**
1	2.587	8.779×10^{-8}	4375
2	1.652	4.866×10^{-8}	5593
3	1.964	3.721×10^{-9}	4473

Table B10**.** Parameters for the 3-site Langmuir model with temperature-dependent saturation capacity for CO_2 adsorption on zeolite 13X (Grace Davidson, MS 544).

***j* (site)**	**$a_{0,j}$, mol/kg**	**c_0, (mol K)/ kg**	**$b_{0,j}$, kPa^{-1}**	**E_j/R, K**
1	1.4186	78.69	5.039×10^{-8}	5573
2	0	763.5	1.827×10^{-7}	4138
3	0	517.2	1.208×10^{-6}	2133

APPENDIX C. H_2O ISOTHERM DATA

Table C11. Adsorption equilibria of H_2O on zeolite 13X (25 °C, 35 °C, 50 °C, 70 °C, and 100 °C).

25 °C		35 °C		50 °C		70 °C		100 °C	
p	*n*	*p*	*n*	*p*	*n*	*p*	*n*	*p*	*n*
kPa	mol/kg	kPa	mol/kg	kPa	mol/kg	kPa	mol/kg	kPa	mol/kg
0.0064	8.6 ± 0.9	0.0128	8.4 ± 0.9	0.0062	7.1 ± 0.7	0.0061	4.9 ± 0.5	0.0061	3.3 ± 0.4
0.0128	10.5 ± 1.1	0.0192	9.0 ± 0.9	0.0124	7.7 ± 0.8	0.0091	5 ± 0.5	0.0091	3.3 ± 0.4
0.0192	11.0 ± 1.1	0.0281	9.6 ± 1.0	0.0247	8.6 ± 0.9	0.0263	5.7 ± 0.6	0.0263	3.7 ± 0.4
0.0256	11.3 ± 1.2	0.0422	10.3 ± 1.1	0.0495	9.6 ± 1	0.100	7.5 ± 0.8	0.100	4.7 ± 0.5
0.0319	11.5 ± 1.2	0.0563	10.7 ± 1.1	0.0742	10.1 ± 1	0.200	8.7 ± 0.9	0.200	5.6 ± 0.6
0.0639	12.1 ± 1.2	0.1125	11.4 ± 1.2	0.0990	10.5 ± 1.1	0.667	10.3 ± 1.1	0.667	7.7 ± 0.8
0.128	12.8 ± 1.3	0.225	12.1 ± 1.2	0.124	10.7 ± 1.1	1.67	11.8 ± 1.2	1.667	9.7 ± 1
0.192	13.3 ± 1.3	0.338	12.6 ± 1.3	0.742	12.5 ± 1.3	3.17	12.3 ± 1.3	3.173	10.3 ± 1.1
0.255	13.6 ± 1.4	0.450	12.9 ± 1.3	1.237	13.1 ± 1.3	5.63	12.8 ± 1.3	5.627	10.9 ± 1.1
0.319	13.9 ± 1.4	0.563	13.2 ± 1.3	2.466	14 ± 1.4	7.60	13.1 ± 1.3	7.599	11.2 ± 1.1
0.479	14.3 ± 1.4	0.844	13.6 ± 1.4	3.700	14.4 ± 1.5	10.1	13.4 ± 1.4	10.132	11.5 ± 1.2
0.639	14.7 ± 1.5	1.125	13.9 ± 1.4	4.949	14.7 ± 1.5	12.3	13.6 ± 1.4	12.332	11.7 ± 1.2
0.798	14.9 ± 1.5	1.407	14.2 ± 1.4	6.166	15.1 ± 1.5	15.2	13.8 ± 1.4	15.199	11.9 ± 1.2
0.958	15.1 ± 1.5	1.688	14.4 ± 1.5	7.423	15.2 ± 1.5	20.3	14.2 ± 1.4	20.265	12.2 ± 1.2
1.12	15.3 ± 1.5	1.97	14.5 ± 1.5	9.90	16.1 ± 1.6	25.33	14.9 ± 1.5	25.33	12.4 ± 1.3
1.28	15.5 ± 1.6	2.25	14.7 ± 1.5	11.14	17.1 ± 1.7				
1.60	15.8 ± 1.6	2.81	15.0 ± 1.5	12.37	17.6 ± 1.8				
1.92	16.2 ± 1.6	3.38	15.2 ± 1.5						
2.24	16.5 ± 1.7	3.94	15.5 ± 1.6						
2.55	17.1 ± 1.7	4.50	15.9 ± 1.6						
2.87	18.2 ± 1.8	5.06	16.6 ± 1.7						

APPENDIX D. FITTED PARAMETERS FOR H_2O ISOTHERMS

Table D12. Fit parameters for the A–D Toth isotherm model for H_2O adsorption on zeolite 13X (Grace Davidson, MS 544).

$a_{0,j}$, mol/kg	$b_{0,j}$, kPa^{-1}	E/R, K	f_0	d
22.39	5.95×10^{-6}	8078	0.174	0.02525

Table D13. Fit parameters for the A–D 2-site Langmuir isotherm model for H_2O adsorption on zeolite 13X (Grace Davidson, MS 544), d = 0.03957.

k (site)	$a_{0,j}$, mol/kg	$b_{0,j}$, kPa^{-1}	E_j/R, K
1	8.975	2.19×10^{-5}	5294
2	6.022	3.68×10^{-12}	8716

Table D14. Fit parameters for the A–D 3-site Langmuir isotherm model for H_2O adsorption on zeolite 13X (Grace Davidson, MS 544), d = 0.02812.

k (site)	$a_{0,j}$, mol/kg	$b_{0,j}$, kPa^{-1}	E_j/R, K
1	4.897	2.11×10^{-13}	9025
2	4.633	2.66×10^{-20}	18896
3	7.514	1.92×10^{-9}	7535

APPENDIX E. MEASURING PELLET DENSITY

The sorbent's pellet density, ρ_{env} is also needed to calculate the bed's porosity. The pellet density, also known as the envelope density, is a measure of the bulk density of a single particle. This density is measured using a Micrometrics envelope density analyzer, GeoPyc Model 1360, conformal to ASTM D-6683. First, a small sample of the sorbent is activated per the method described in Appendix B. After activation, ~25 mL of sorbent is measured and placed in a hermetically sealed vial in the dry-N_2 glove box to prevent contamination. The mass of sorbent is measured on a scale (Mettler Toledo, XS105 Dual Range Balance, ±0.02 mg). A 50.8 mm inner diameter, precision bore glass cylinder was then filled with 50 mL of DryFlow powder, a proprietary substance that acts as a quasi-fluid composed of small, rigid spheres having a high degree of flowability. The glass cylinder was placed in the GeoPyc where the exact volume of powder was measured with a consolidation force of 145 N. The sorbent was then added to the cylinder along with the powder, and the volume of the sorbent plus DryFlow powder was measured (see Figure E1). The difference between these two measurements is the envelope volume of the sorbent.

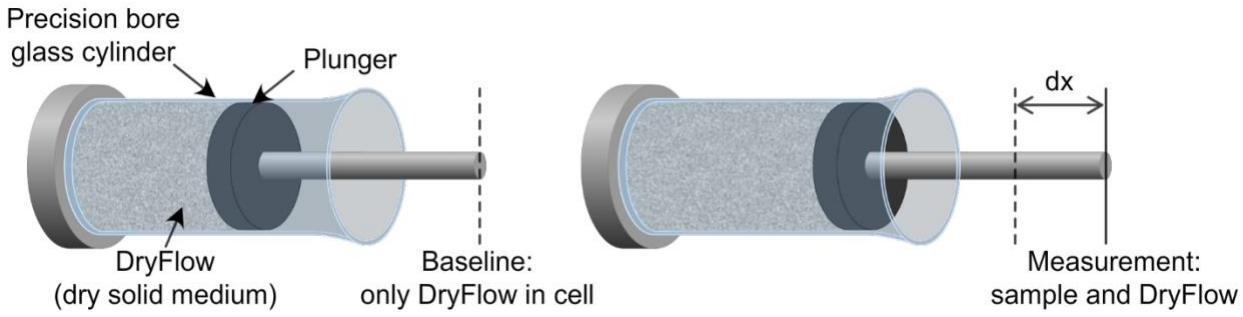

Figure E1. Volume determination by displacement of a dry medium in Micrometric, GeoPyc Model 1360, schematic of the measurement technique.

This measurement was repeated several times for each type of sorbent to estimate the variability within a single batch of sorbent. The results are summarized in Table E15..

Table E15. Envelope density measured for several commercial sorbents.

Sorbent	**ρ_{pellet} (kg/m^3) mean**	**measurement std. deviation (kg/m^3)**	**population std. deviation (kg/m^3)**	**std. deviation of mean (kg/m^3)**
VSA-10	973.8	0.7	6.9	7.0
APG-III	1112.1	4.4	32.6	32.9
ASRT-95	1118.6	0.5	3.0	3.1
RK-38	1179.0	N/A	N/A	N/A
SG-B125	1183.2	1.2	31.3	31.4
544-13X	1053.9	0.6	5.4	5.5
544C-13X	1045.2	0.5	4.3	4.3

APPENDIX F. CALIBRATION OF CANISTER–AMBIENT THERMAL RESISTANCE

The canister–ambient thermal resistance represents the combined resistance of the canister-insulation interface as

$$R'_{\text{can–amb}} = R'_{\text{can–ins}} + R'_{\text{ins}} + R'_{\text{ins–amb}}. \quad \text{F1}$$

where $R'_{\text{can–ins}}$ is the contact resistance between the canister and insulation R'_{ins} is the conduction resistance across the insulation, and $R'_{\text{ins–amb}}$ s the resistance due to convection from the outside of the insulation to ambient air. The latter two resistances can be expressed as

$$R'_{\text{ins}} = \frac{\ln\left(d_{\text{ins,out}}/d_{\text{ins,in}}\right)}{2\pi k_{\text{ins}}} \quad \text{F2}$$

and

$$R'_{\text{ins–amb}} = \frac{1}{\pi d_{\text{ins,out}} h_{\text{ins–anb}}} \quad \text{F3}$$

respectively. This approach lumps several unknown/uncertain parameters (*e.g.*, k_{ins} and $h_{\text{ins-amb}}$) into a single thermal resistance which can be directly calibrated for each test stand.

We perform a separate thermal heat loss characterization experiment to calibrate the heat transfer resistance from the canister to ambient for each test stand. The test is performed by flowing hot N_2 through the cylindrical chamber/sorbent bed. Pure N_2 with no adsorbate is used so that the heat of adsorption does not need to be considered in the analysis. Once the desired flow rate is set, the centerline gas temperature and canister surface temperature are monitored for approximately three hours until steady state is observed, and then recorded at 1 Hz for an additional 60 min. Temperature measurements and volumetric flow rate data are averaged over the steady-state period. A line is fit to the time-averaged gas temperatures versus axial position (see Figures S1 and S2). The heat loss per unit length is then calculated from the derivative of the linear fit as

$$q' = \dot{m} c_{p,\text{g}} \frac{dT_{\text{g}}}{dz} \quad \text{F4}$$

The thermal resistance between the outside of the canister wall and ambient air is then calculated as

$$R'_{\text{can–amb}} = \frac{T_{\text{can}} - T_{\text{amb}}}{q'} \qquad \text{F5}$$

From the average of the thermal resistances measured, $R'_{\text{can–amb}}$ was found to be 2.04 K/(m W) and 3.82 K/(m W) for the small- and large-diameter test stands, respectively.

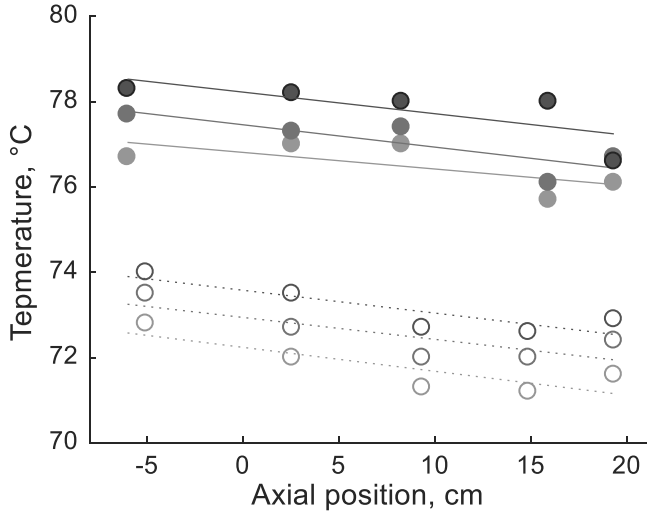

Figure F2. Plot of temperatures as a function of axial position in the large-diameter bed. Results for three independent tests are plotted in three shades of gray. Filled circles represent gas-phase temperatures measured at the centerline of the bed and empty circles represent the canister wall temperature. Least-square fits are plotted as lines for each independent experiment.

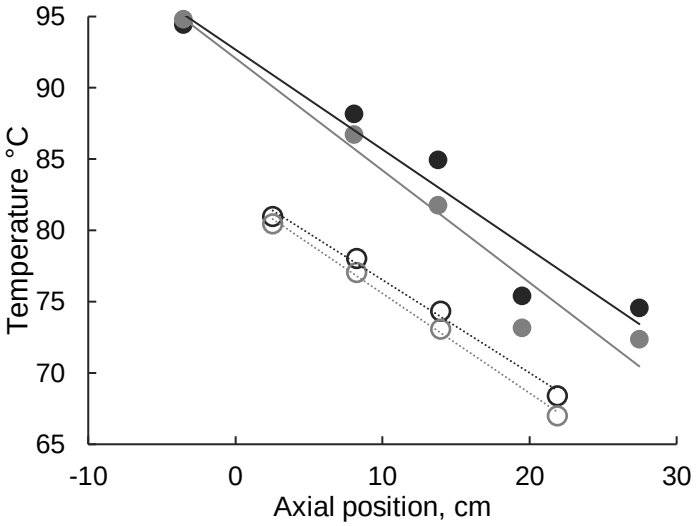

Figure F3. Plot of temperatures as a function of axial position in the small-diameter bed. Results for two independent tests are plotted in two shades of gray. Filled circles represent gas-phase temperatures measured at the centerline of the bed and empty circles represent the canister wall temperature. Least-square fits are plotted as lines for each independent experiment.

Table F16. Summary of test conditions and resulting thermal resistance between the outside of the canister wall and ambient air for the large-diameter test stand.

test description	V (SLPM)	T_g (°C)	T_{can} (°C)	T_{amb} (°C)	dT_g/dz (°C/m)	dT_s/dz (°C/m)	q' (W/m)	R' (K/Wm)
Empty Canister	119.0	76.5	71.8	22.7	-3.97	-5.62	10.6	4.6
	116.5	77.0	72.5	23.4	-5.09	-4.98	13.3	3.7
	100.0	70.9	67.1	23.5	-7.49	-5.18	16.8	2.6
Packed Bed	119.0	77.8	73.2	22.9	-4.90	-5.39	13.0	4.0

Table F17. Summary of test conditions and resulting thermal resistance between the outside of the canister wall and ambient air for the small-diameter test stand.

test description	V (SLPM)	T_g (°C)	T_{can} (°C)	T_{amb} (°C)	dT_g/dz (°C/m)	dT_s/dz (°C/m)	q' (W/m)	R' (K/Wm)
Thermal Test	16	81.8	75.9	22.0	-78.7	-69.9	28.2	1.9
	16	83.5	76.7	22.0	-70.1	-65.2	25.1	2.2

REFERENCES

[1] R. T. Yang, *Gas Separation by Adsorption Processes*. Imperial College Press, 1997.

[2] S. S. Dewan, "CHEMICAL SEPARATION AND PURIFICATION: TECHNOLOGIES AND GLOBAL MARKETS," p. 146.

[3] A. McWilliams, "The Global Industrial Gas Business," bccResearch, CHM041F, Sep. 2018.

[4] A. Kumar, "ABSORBENT AND ADSORBENT MATERIALS: GLOBAL MARKETS," p. 227.

[5] G. E. Keller, "Gas-Adsorption Processes: State of the Art," in *Industrial Gas Separations*, vol. 223, T. E. Whyte, C. M. Yon, and E. H. Wagener, Eds. WASHINGTON, D. C.: AMERICAN CHEMICAL SOCIETY, 1983, pp. 145–169.

[6] "WMO Greenhouse Gas Bulletin," World Meteorological Organization, Nov. 2017.

[7] "2014 Strategic Plan," NASA, 2014.

[8] J. Knox, G. Cmarik, D. Watson, L. Miller, and T. Giesy, "Investigation of Desiccants and CO2 Sorbents for Exploration Systems 2016-2017," Jul. 2017.

[9] J. C. Knox, "Development of Carbon Dioxide Removal Systems for NASA's Deep Space Human Exploration Missions 2016-2017," in *Proceedings of the 47th International Conference on Environmental Systems*, Charleston, South Carolina, 2017.

[10] R. Coker and J. Knox, "Predictive modeling of the CDRA 4BMS," in *Proceedings of the 46th International Conference on Environmental Systems*, Vienna, Austria, 2016.

[11] J. C. Knox, "Predictive simulation of gas adsorption in fixed beds and limitations due to the ill-posed Danckwerts boundary condition," dissertation, The University of Alabama in Huntsville, Huntsville, AL, 2016.

[12] M. S. Shafeeyan, W. M. A. Wan Daud, and A. Shamiri, "A review of mathematical modeling of fixed-bed columns for carbon dioxide adsorption," *Chemical Engineering Research and Design*, vol. 92, no. 5, pp. 961–988, May 2014.

[13] E. Glueckauf and J. I. Coates, "Theory of chromatography; the influence of incomplete equilibrium on the front boundary of chromatograms and on the effectiveness of separation," *J. Chem. Soc.*, pp. 1315–1321, 1947.

[14] S. Sircar and J. R. Hufton, "Why Does the Linear Driving Force Model for Adsorption Kinetics Work?," *Adsorption*, vol. 6, no. 2, pp. 137–147, Jun. 2000.

[15] J. C. Knox, A. D. Ebner, M. D. LeVan, R. F. Coker, and J. A. Ritter, "Limitations of breakthrough curve analysis in fixed-bed adsorption," *Ind. Eng. Chem. Res.*, vol. 55, no. 16, pp. 4734–4748, Apr. 2016.

[16] D. D. Do, *Adsorption analysis: equilibria and kinetics*. London, England: Imperial College Press, 1998.

[17] I. M. C. Lo and P. A. Alok, "Computer simulation of activated carbon adsorption for multi-component systems," *Environ. Int.*, vol. 22, no. 2, pp. 239–252, Jan. 1996.

[18] F. A. Farhadpour and A. Bono, "Sorptive separation of ethanol-water mixtures with a bi-dispersed hydrophobic molecular sieve, silicalite: measurement and theoretical analysis of column dynamics," *Chem. Eng. Processing*, vol. 35, no. 2, pp. 157–168, Mar. 1996.

[19] N. Abdel-Jabbar, S. Al-Asheh, and B. Hader, "Modeling, Parametric Estimation, and Sensitivity Analysis for Copper Adsorption with Moss Packed-Bed," *Sep. Sci. Technol.*, vol. 36, no. 13, pp. 2811–2833, Oct. 2001.

[20] D. C. K. Ko, J. F. Porter, and G. McKay, "Film-pore diffusion model for the fixed-bed sorption of copper and cadmium ions onto bone char," *Water Res*, vol. 35, no. 16, pp. 3876–3886, Nov. 2001.

[21] S. Gomez-Salazar, J. S. Lee, J. C. Heydweiller, and L. L. Tavlarides, "Analysis of cadmium adsorption on novel organo-ceramic adsorbents with a thiol functionality," *Ind. Eng. Chem. Res.*, vol. 42, no. 14, pp. 3403–3412, Jul. 2003.

[22] E. Worch, "Modelling the solute transport under nonequilibrium conditions on the basis of mass transfer equations," *J. Contam. Hydrol.*, vol. 68, no. 1–2, pp. 97–120, Jan. 2004.

[23] S. Chakraborty, S. De, S. DasGupta, and J. K. Basu, "Adsorption study for the removal of a basic dye: experimental and modeling," *Chemosphere*, vol. 58, no. 8, pp. 1079–1086, Feb. 2005.

[24] L. Lv, Y. Zhang, K. Wang, A. K. Ray, and X. S. Zhao, "Modeling of the adsorption breakthrough behaviors of Pb2+ in a fixed bed of ETS-10 adsorbent," *J. Colloid Interf. Sci.*, vol. 325, no. 1, pp. 57–63, Sep. 2008.

[25] D. Richard, N. Delgado, and D. Schweich, "Adsorption of complex phenolic compounds on active charcoal: Breakthrough curves," *Chem. Eng. J.*, vol. 158, no. 2, pp. 213–219, 2010.

[26] L. Abu-Lail, J. A. Bergendahl, and R. W. Thompson, "Mathematical modeling of chloroform adsorption onto fixed-bed columns of highly siliceous granular zeolites," *Environ. Prog. Sustain. Energy*, vol. 31, no. 4, pp. 591–596, Dec. 2012.

[27] B. Likozar, D. Senica, and A. Pavko, "Interpretation of experimental results for vancomycin adsorption on polymeric resins in a fixed bed column by mathematical modeling with independently estimated parameters," *Ind. Eng. Chem. Res.*, vol. 52, no. 26, pp. 9247–9258, Jul. 2013.

[28] T. Nur, W. G. Shim, M. A. H. Johir, S. Vigneswaran, and J. Kandasamy, "Modelling of phosphorus removal by ion-exchange resin (Purolite FerrIX A33E) in fixed-bed column experiments," *Desalin. Water Treat.*, vol. 52, no. 4–6, pp. 784–790, Jan. 2014.

[29] K. N. Gupta, N. J. Rao, and G. K. Agarwal, "Gaseous phase adsorption of volatile organic compounds on granular activated carbon," *Chem. Eng. Commun.*, vol. 202, no. 3, pp. 384–401, Mar. 2015.

[30] N. E. Davila-Guzman, F. J. Cerino-Córdova, M. Loredo-Cancino, J. R. Rangel-Mendez, R. Gómez-González, and E. Soto-Regalado, "Studies of adsorption of heavy metals onto spent coffee ground: Equilibrium, regeneration, and dynamic performance in a fixed-bed column," *Int. J. Chem. Eng.*, vol. 2016, 2016.

[31] Y. Shao and H. Chen, "Adsorption kinetics of p-nitrophenol (PNP) on coal-based activated carbon: experimental and simulation," *Desalin. Water Treat.*, vol. 57, no. 31, pp. 14496–14505, Jul. 2016.

[32] M. H. Chahbani and D. Tondeur, "Mass transfer kinetics in pressure swing adsorption," *Sep. Purif. Technol.*, vol. 20, no. 2–3, pp. 185–196, Sep. 2000.

[33] D. G. Hartzog and S. Sircar, "Sensitivity of PSA process performance to input variables," *Adsorption*, vol. 1, no. 2, pp. 133–151, 1995.

[34] M. Ratto, G. Lodi, and P. Costa, "Sensitivity analysis of a fixed-bed gas-solid TSA: the problem of design with uncertain models," *Sep. Technol.*, vol. 6, no. 4, pp. 235–245, Oct. 1996.

[35] Z. Yu, S. Peldszus, and P. M. Huck, "Adsorption of selected pharmaceuticals and an endocrine disrupting compound by granular activated carbon. 2. Model prediction," *Environ. Sci. Technol.*, vol. 43, no. 5, pp. 1474–1479, Mar. 2009.

[36] H. T. J. Reijers, J. Boon, G. D. Elzinga, P. D. Cobden, W. G. Haije, and R. W. van den Brink, "Modeling study of the sorption-enhanced reaction process for CO2 capture. I. Model development and validation," *Ind. Eng. Chem. Res.*, vol. 48, no. 15, pp. 6966–6974, Aug. 2009.

[37] Y. Lu, J. He, L. Wu, and G. Luo, "Relationship between breakthrough curve and adsorption isotherm of Ca(II) imprinted chitosan microspheres for metal adsorption," *Chin. J. Chem. Eng.*, vol. 24, no. 2, pp. 323–329, Feb. 2016.

[38] P. G. Aguilera and F. J. Gutiérrez Ortiz, "Prediction of fixed-bed breakthrough curves for H2S adsorption from biogas: Importance of axial dispersion for design," *Chem. Eng. J.*, vol. 289, pp. 93–98, Apr. 2016.

[39] M. Zheng, C. Xu, H. Hu, Z. Ye, and X. Chen, "A modified homogeneous surface diffusion model for the fixed-bed adsorption of 4,6-DMDBT on Ag–CeOx/TiO2–SiO2," *RSC Adv.*, vol. 6, no. 114, pp. 112899–112907, Nov. 2016.

[40] S. Sircar and J. R. Hufton, “Why does the linear driving force model for adsorption kinetics work?,” *Adsorption*, vol. 6, no. 2, pp. 137–147, 2000.

[41] H. T. J. Reijers, J. Boon, G. D. Elzinga, P. D. Cobden, W. G. Haije, and R. W. van den Brink, “Modeling study of the sorption-enhanced reaction process for CO2 capture. II. Application to steam-methane reforming,” *Ind. Eng. Chem. Res.*, vol. 48, no. 15, pp. 6975–6982, Aug. 2009.

[42] G. Naja and B. Volesky, “Optimization of a biosorption column performance,” *Environ. Sci. Technol.*, vol. 42, no. 15, pp. 5622–5629, Aug. 2008.

[43] B. J. Maring and P. A. Webley, “A new simplified pressure/vacuum swing adsorption model for rapid adsorbent screening for CO2 capture applications,” *Int. J. Greenh. Gas Con.*, vol. 15, pp. 16–31, Jul. 2013.

[44] J. Kalyanaraman, Y. Kawajiri, and M. J. Realff, “Bayesian estimation, uncertainty propagation and design of experiments for CO2 adsorption on amine sorbents,” in *Proceedings of the 8th International Conference on Foundations of Computer-Aided Process Design*, Cle Elum, WA, 2014, pp. 345–350.

[45] B. Borina and A. Pavko, “Adsorption of vancomycin on Amberlite XAD-16 in a packed bed column,” *Chem. Biochem. Eng. Q.*, vol. 23, no. 4, pp. 479–483, 2009.

[46] J. M. P. Q. Delgado, “A critical review of dispersion in packed beds,” *Heat Mass Transfer*, vol. 42, no. 4, pp. 279–310, Feb. 2006.

[47] J. M. P. Q. Delgado, “Longitudinal and transverse dispersion in porous media,” *Chem. Eng. Res. Des.*, vol. 85, no. 9, pp. 1245–1252, 2007.

[48] S. Sircar, R. Kumar, and K. J. Anselmo, “Effects of column nonisothermality or nonadiabaticity on the adsorption breakthrough curves,” *Ind. Eng. Chem. Proc. Des. Dev.*, vol. 22, no. 1, pp. 10–15, Jan. 1983.

[49] F. Delage, P. Pré, and P. Le Cloirec, “Mass transfer and warming during adsorption of high concentrations of VOCs on an activated carbon bed: Experimental and theoretical analysis,” *Environ. Sci. Technol.*, vol. 34, no. 22, pp. 4816–4821, Nov. 2000.

[50] S. Sircar, “Influence of gas-solid heat transfer on rapid PSA,” *Adsorption*, vol. 11, no. 1, pp. 509–513, Jul. 2005.

[51] K. S. Walton and M. D. LeVan, “Effect of energy balance approximations on simulation of fixed-bed adsorption,” *Ind. Eng. Chem. Res.*, vol. 44, no. 19, pp. 7474–7480, Sep. 2005.

[52] B. Shirani, T. Kaghazchi, and M. Beheshti, “Water and mercaptan adsorption on 13X zeolite in natural gas purification process,” *Korean J. Chem. Eng.*, vol. 27, no. 1, pp. 253–260, Jan. 2010.

[53] K.-M. Kim, H.-T. Oh, S.-J. Lim, K. Ho, Y. Park, and C.-H. Lee, "Adsorption Equilibria of Water Vapor on Zeolite 3A, Zeolite 13X, and Dealuminated Y Zeolite," *J. Chem. Eng. Data*, vol. 61, no. 4, pp. 1547–1554, Apr. 2016.

[54] R. Kay, "International Space Station (ISS) Carbon Dioxide Removal Assembly (CDRA) Protoflight Performance Testing," presented at the International Conference On Environmental Systems, Danvers, Massachusetts, 1998.

[55] G. D. L. Hopson, "Skylab environmental control and life support systems," presented at the Life Support and Environmental Control Conference, San Francisco, CA, 1971, pp. 71-AV-14.

[56] Q. H. Dirar and K. F. Loughlin, "Intrinsic adsorption properties of CO2 on 5A and 13X zeolite," *Adsorption*, vol. 19, no. 6, pp. 1149–1163, Dec. 2013.

[57] Y. Wang and M. D. LeVan, "Adsorption equilibrium of carbon dioxide and water vapor on zeolites 5A and 13X and silica gel: Pure components," *J. Chem. Eng. Data*, vol. 54, no. 10, pp. 2839–2844, Oct. 2009.

[58] L. Erden *et al.*, "On the variability and reproducibility of equilibrium adsorption isotherm measurements from different laboratories," presented at the lewis, San Francisco, CA, 03-Nov-2013.

[59] F. Brandani and D. M. Ruthven, "The Effect of Water on the Adsorption of CO2 and C3H8 on Type X Zeolites," *Ind. Eng. Chem. Res.*, vol. 43, no. 26, pp. 8339–8344, Dec. 2004.

[60] S. Sircar, "Heat of adsorption on heterogeneous adsorbents," *Appl. Surf. Sci.*, vol. 252, no. 3, pp. 647–653, Oct. 2005.

[61] M. A. Alkhabbaz, P. Bollini, G. S. Foo, C. Sievers, and C. W. Jones, "Important roles of enthalpic and entropic contributions to CO2 capture from simulated flue gas and ambient air using mesoporous silica grafted amines," *J. Am. Chem. Soc.*, vol. 136, no. 38, pp. 13170–13173, 2014.

[62] A. L. Myers, "Thermodynamics of adsorption in porous materials," *AIChE J.*, vol. 48, no. 1, pp. 145–160, Jan. 2002.

[63] S. Sircar, R. Mohr, C. Ristic, and M. B. Rao, "Isosteric heat of adsorption: theory and experiment," *J. Phys. Chem. B*, vol. 103, no. 31, pp. 6539–6546, Aug. 1999.

[64] S. J. Bhadra, A. D. Ebner, and J. A. Ritter, "On the use of the dual process Langmuir model for predicting unary and binary isosteric heats of adsorption," *Langmuir*, vol. 28, no. 17, pp. 6935–6941, May 2012.

[65] G. N. Lewis, M. Randall, K. S. Pitzer, and L. Brewer, *Thermodynamics*, 2nd ed. McGraw-Hill Book Company, 1961.

[66] J. A. Dunne, M. Rao, S. Sircar, R. J. Gorte, and A. L. Myers, "Calorimetric heats of adsorption and adsorption isotherms. 2. O2, N2, Ar, CO2, CH4, C2H6, and SF6 on NaX, H-ZSM-5, and Na-ZSM-5 zeolites," *Langmuir*, vol. 12, no. 24, pp. 5896–5904, Jan. 1996.

[67] D. Shen, M. Bülow, F. Siperstein, M. Engelhard, and A. L. Myers, "Comparison of experimental techniques for measuring isosteric heat of adsorption," *Adsorption*, vol. 6, no. 4, pp. 275–286, Dec. 2000.

[68] N. N. Avgul', B. G. Aristov, A. V. Kiselev, L. Y. Kurdyuko, and N. V. Frolova, "Adsorption and heat of adsorption of carbon dioxide on LiX zeolite," *Russ. J. Phys. Chem.*, vol. 42, no. 10, pp. 1426-, 1968.

[69] C. Bläker, M. Luckas, C. Pasel, F. Dreisbach, and D. Bathen, "Entwicklung eines Messgeräts zur Kopplung von kalorimetrischen und volumetrischen Sorptionsmessungen," *Chemie Ingenieur Technik*, vol. 88, no. 3, pp. 282–290, Mar. 2016.

[70] F. W. M. da Silva *et al.*, "Adsorption microcalorimetry applied to the characterisation of adsorbents for CO2 capture," *Can. J. Chem. Eng.*, vol. 90, no. 6, pp. 1372–1380, Dec. 2012.

[71] S. S. Khvoshchev and A. V. Zverev, "Calorimetric study of NH3 and CO2 adsorption on synthetic faujasites with Ca2+, Mg2+, and La3+ cations," *J. Colloid Interf. Sci.*, vol. 144, no. 2, pp. 571–578, 1991.

[72] D. F. Plant, G. Maurin, I. Deroche, and P. L. Llewellyn, "Investigation of CO2 adsorption in faujasite systems: grand canonical Monte Carlo and molecule dynamics simulations based on a new derived Na+-CO2," *Microporous Mesoporous Mat.*, vol. 99, no. 1–2, pp. 70–78, Feb. 2007.

[73] W. Zimmermann and J. U. Keller, "A new calorimeter for simultaneous measurement of isotherms and heats of adsorption," *Thermochimica Acta*, vol. 405, no. 1, pp. 31–41, Oct. 2003.

[74] P. L. Llewellyn and G. Maurin, "Gas adsorption microcalorimetry and modelling to characterise zeolites and related materials," *Comptes Rendus Chimie*, vol. 8, no. 3, pp. 283–302, Mar. 2005.

[75] Y. Cohen and A. B. Metzner, "Wall effects in laminar flow of fluids through packed beds," *AIChE Journal*, vol. 27, no. 5, pp. 705–715, Sep. 1981.

[76] J. F. Richardson, J. H. Harker, and J. R. Backhurst, *Coulson & Richardson's chemical engineering: Particle Technology and Separation Processes*, 5 edition., vol. 2. Oxford: Butterworth-Heinemann, 2002.

[77] K. N. Son, J. A. Weibel, S. V. Garimella, and J. C. Knox, "Calibration and Sensitivity of a Fixed-Bed Adsorption Model for Atmosphere Revitalization in Space," in *Proceedings of the 47th International Conference on Environmental Systems*, Charleston, South Carolina, 2017, p. 173.

[78] K. N. Son, J. A. Weibel, J. C. Knox, and S. V. Garimella, "Calibration and uncertainty analysis of a fixed-bed adsorption model for CO2 separation," *Adsorption*, vol. 24, no. 8, pp. 781–802, Nov. 2018.

[79] F. Augier, C. Laroche, and E. Brehon, "Application of computational fluid dynamics to fixed bed adsorption calculations: Effect of hydrodynamics at laboratory and industrial scale," *Separation and Purification Technology*, vol. 63, no. 2, pp. 466–474, Oct. 2008.

[80] K. N. Son, C. Gomez, M. Paragon, and J. C. Knox, "Experimental validation of vacuum desorption in 1-D model of CO2 removal," in *Proceedings of the 46th International Conference on Environmental Systems*, Vienna, Austria, 2016.

[81] "Adsorbents for Process Applications," Grace Davison, W. R. Grace & Co., Columbia, MD, 2010.

[82] R. Kay and D. Pancho, "Evaluation of alternative desiccants and adsorbents for the desiccant/adsorbent bed," Honeywell, 12–77742, CAGE 70210, 2013.

[83] "Q-Fiber® Felt Data Sheet," Johns Manville, Denver, CO, HPI-25 4-08, 2008.

[84] "Datasheet Flexible Min-K®," Morgan Advanced Materials, 6-14–120, 2013.

[85] "Physical Properties of Pyropel® Insulation," Albany International, Rochester, NH.

[86] M. F. Edwards and J. F. Richardson, "Gas dispersion in packed beds," *Chem. Eng. Sci.*, vol. 23, no. 2, pp. 109–123, May 1968.

[87] "Material library user's guide," COMSOL AB, Stockholm, SE, COMSOL Multiphysics®, ver. 5.2a.

[88] N. Wakao, S. Kaguei, and T. Funazkri, "Effect of fluid dispersion coefficients on particle-to-fluid heat transfer coefficients in packed beds," *Chem. Eng. Sci.*, vol. 34, no. 3, pp. 325–336, Jan. 1979.

[89] C.-H. Li and B. A. Finlayson, "Heat transfer in packed beds—a reevaluation," *Chem. Eng. Sci.*, vol. 32, no. 9, pp. 1055–1066, 1976.

[90] S. Yagi, D. Kunii, and N. Wakao, "Studies on axial effective thermal conductivities in packed beds," *AIChE J.*, vol. 6, no. 4, pp. 543–546, Dec. 1960.

[91] R. Krupiczka, "Analysis of thermal conductivity in granular materials," *Int. Chem. Eng.*, vol. 7, no. 1, pp. 122–144, 1967.

[92] G. Langer, A. Roethe, K.-P. Roethe, and D. Gelbin, "Heat and mass transfer in packed beds—III. Axial mass dispersion," *Int. J. Heat Mass Transf.*, vol. 21, no. 6, pp. 751–759, Jun. 1978.

[93] D. F. Fairbanks and C. R. Wilke, "Diffusion coefficients in multicomponent gas mixtures," *Ind. Eng. Chem.*, vol. 42, no. 3, pp. 471–475, Mar. 1950.

[94] J. O. Hirschfelder, C. F. Curtiss, and R. B. Bird, *The Molecular Theory of Gases and Liquids*. London, England: Wiley-Interscience, 1964.

[95] J. Toth, "State equations of the solid gas interface layer," *Acta Chim. Acad. Sci. Hung.*, vol. 69, no. 3, pp. 311–317, 1971.

[96] N. Wakao and S. Kagei, *Heat and Mass Transfer in Packed Beds*. New York, NY: Taylor & Francis, 1982.

[97] A. Bradshaw, A. Johnson, N. Mclachlan, and Y. Chiu, "Heat transfer between air and nitrogen and packed beds of non-reacting solids," *Trans. Inst. Chem. Eng.*, vol. 48, no. 3, pp. T77–T84, 1970.

[98] J. De Acetis and G. Thodos, "Mass and heat transfer in flow of gases through spherical packings," *Ind. Eng. Chem.*, vol. 52, no. 12, pp. 1003–1006, Dec. 1960.

[99] L. R. Galloway, W. Komarnicky, and N. Epstein, "Effect of configuration on mass and heat transfer in beds of stacked spheres," *Can. J. Chem. Eng.*, vol. 35, no. 4, pp. 139–150, 1957.

[100] M. J. Goss and G. A. Turner, "Simultaneous computation of heat transfer and dispersion coefficients and thermal conductivity value in a packed bed of spheres: II. Technique of computing numerical values," *AIChE J.*, vol. 17, no. 3, pp. 590–592, May 1971.

[101] Handley, D. and Heggs, P.J., "Momentum and heat transfer mechanisms in regular shaped packings," *Trans. Inst. Chem. Eng.*, vol. 46, pp. T251–T264, 1968.

[102] G. F. Malling and G. Thodos, "Analogy between mass and heat transfer in beds of spheres: Contributions due to end effects," *Int. J. Heat Mass Transf.*, vol. 10, no. 4, pp. 489–492, Apr. 1967.

[103] J. T. L. McConnachie and G. Thodos, "Transfer processes in the flow of gases through packed and distended beds of spheres," *AIChE J.*, vol. 9, no. 1, pp. 60–64, Jan. 1963.

[104] C. N. Satterfield and H. Resnick, "Simultaneous heat and mass transfer in a diffusion-controlled chemical reaction .2. Studies in a packed bed," *Chem. Eng. Prog.*, vol. 50, no. 10, pp. 504–510, 1954.

[105] A. Sen Gupta and G. Thodos, "Direct analogy between mass and heat transfer to beds of spheres," *AIChE J.*, vol. 9, no. 6, pp. 751–754, Nov. 1963.

[106] G. A. Turner and L. Otten, "Values of thermal (and other) parameters in packed beds," *Ind. Eng. Chem. Proc. Des. Dev.*, vol. 12, no. 4, pp. 417–424, Oct. 1973.

[107] C. R. Wilke and O. Hougen, "Mass transfer in the flow of gases through granular solids extended to low modified Reynolds numbers," *Trans. Am. Inst. Chem. Eng.*, vol. 41, no. 4, pp. 445–451, 1945.

[108] S. Yagi and N. Wakao, “Heat and mass transfer from wall to fluid in packed beds,” *AIChE J.*, vol. 5, no. 1, pp. 79–85, Mar. 1959.

[109] D. Kunii, M. Suzuki, and N. Ono, “Heat transfer from wall surface to packed beds at high Reynolds number,” *J. Chem. Eng. Jpn.*, vol. 1, no. 1, pp. 21–26, 1968.

[110] K. W. McHenry and R. H. Wilhelm, “Axial mixing of binary gas mixtures flowing in a random bed of spheres,” *AIChE J.*, vol. 3, no. 1, pp. 83–91, Mar. 1957.

[111] J. J. Carberry and R. H. Bretton, “Axial dispersion of mass in flow through fixed beds,” *AIChE J.*, vol. 4, no. 3, pp. 367–375, Sep. 1958.

[112] R. J. Blackwell, R. J. Rayne, and W. M. Terry, “Factors influencing the efficiency of miscible displacement.,” *J. Petrol. Technol.*, vol. 217, p. 9, 1959.

[113] T. K. Perkins and O. C. Johnston, “A review of diffusion and dispersion in porous media,” *Soc. Petrol. Eng. J.*, vol. 3, no. 1, pp. 70–84, Mar. 1963.

[114] R. J. Sinclair and O. E. Potter, “The dispersion of gas in flow through a bed of packed solids,” *Trans. Inst. Chem. Eng.*, vol. 43, pp. 3–9, 1965.

[115] D. J. Gunn and C. Pryce, “Dispersion in Packed Beds,” *Trans. Inst. Chem. Eng.*, vol. 47, no. 10, pp. t341–t350, 1969.

[116] G. W. Johnson and R. S. Kapner, “The dependence of axial dispersion on non-uniform flows in beds of uniform packing,” *Chem. Eng. Sci.*, vol. 45, no. 11, pp. 3329–3339, 1990.

[117] D. S. Scott, W. Lee, and J. Papa, “The measurement of transport coefficients in gas-solid heterogeneous reactions,” *Chem. Eng. Sci.*, vol. 29, no. 11, pp. 2155–2167, Nov. 1974.

[118] E. Wicke, “Significance of molecular diffusion for chromatographic procedures,” *Ber. Bunsen-Ges. Phys. Chem. Chem. Phys.*, vol. 77, no. 3, pp. 160–171, 1973.

[119] T. Özgümüş, M. Mobedi, Ü. Özkol, and A. Nakayama, “Thermal Dispersion in Porous Media—A Review on the Experimental Studies for Packed Beds,” *Appl. Mech. Rev*, vol. 65, no. 3, p. 031001, Jul. 2013.

[120] D. Kunii and J. M. Smith, “Heat transfer characteristics of porous rocks: II. Thermal conductivities of unconsolidated particles with flowing fluids,” *AIChE J.*, vol. 7, no. 1, pp. 29–34, Mar. 1961.

[121] J. Votruba, V. Hlaváček, and M. Marek, “Packed bed axial thermal conductivity,” *Chem. Eng. Sci.*, vol. 27, no. 10, pp. 1845–1851, Oct. 1972.

[122] D. J. Gunn and J. F. C. De Souza, “Heat transfer and axial dispersion in packed beds,” *Chem. Eng. Sci.*, vol. 29, no. 6, pp. 1363–1371, Jun. 1974.

[123] D. J. Gunn and M. Khalid, "Thermal dispersion and wall heat transfer in packed beds," *Chem. Eng. Sci.*, vol. 30, no. 2, pp. 261–267, Feb. 1975.

[124] D. Vortmeyer and W. Adam, "Steady-state measurements and analytical correlations of axial effective thermal conductivities in packed beds at low gas flow rates," *Int J Heat Mass Transf*, vol. 27, no. 9, pp. 1465–1472, Sep. 1984.

[125] F. P. Incropera, D. P. DeWitt, T. L. Bergman, and A. S. Lavine, *Fundamentals of Heat and Mass Transfer*, 6th edition. Hoboken, NJ: John Wiley & Sons, 2006.

[126] *COMSOL Multiphysics*®. Stockholm, SE: COMSOL AB, 2016.

[127] R. Huang, G. Belancik, D. Jan, J. C. Knox, and T.-M. J. Richardson, "CO2 capacity sorbent analysis using volumetric measurement approach," in *Proceedings of the 47th International Conference on Environmental Systems*, Charleston, South Carolina, 2017.

[128] G. E. Cmarik, K. N. Son, and J. C. Knox, "Standard isotherm fit information for dry CO2 on sorbents for 4BMS," NASA, Technical Memo NASA/TM—2017-219847, 2017.

[129] K. N. Son, G. E. Cmarik, J. C. Knox, J. A. Weibel, and S. V. Garimella, "Measurement and Prediction of the Heat of Adsorption and Equilibrium Concentration of CO2 on Zeolite 13X," *J. Chem. Eng. Data*, vol. 63, no. 5, pp. 1663–1674, May 2018.

[130] J. Rouquerol *et al.*, "Recommendations for the characterization of porous solids (Technical Report)," *Pure Appl. Chem., PAC*, vol. 66, no. 8, pp. 1739–1758, 1994.

[131] I. Langmuir, "The constitution and fundamental properties of solids and liquids. Part I. solids.," *J. Am. Chem. Soc.*, vol. 38, no. 11, pp. 2221–2295, Nov. 1916.

[132] T. Nitta, T. Shigetomi, M. Kuro-Oka, and T. Katayama, "An adsorption isotherm of multi-site occupancy model for homogeneous surface," *J. Chem. Eng. Jpn.*, vol. 17, no. 1, pp. 39–45, 1984.

[133] S. U. Rege, R. T. Yang, and M. A. Buzanowski, "Sorbents for air prepurification in air separation," *Chem. Eng. Sci.*, vol. 55, no. 21, pp. 4827–4838, Nov. 2000.

[134] F. Brandani, "Development and Application of the Zero Length Column (ZLC) Technique for Measuring Adsorption Equilibria," dissertation, The University of Maine, 2002.

[135] F. Brandani, D. Ruthven, and C. G. Coe, "Measurement of Adsorption Equilibrium by the Zero Length Column (ZLC) Technique Part 1: Single-Component Systems," *Ind. Eng. Chem. Res.*, vol. 42, no. 7, pp. 1451–1461, Apr. 2003.

[136] Y. Belmabkhout and A. Sayari, "Isothermal versus non-isothermal adsorption−desorption cycling of triamine-grafted pore-expanded MCM-41 mesoporous silica for CO2 capture from flue gas," *Energy Fuels*, vol. 24, no. 9, pp. 5273–5280, Sep. 2010.

[137] A. Khelifa, L. Benchehida, and Z. Derriche, “Adsorption of carbon dioxide by X zeolites exchanged with Ni2+ and Cr3+: isotherms and isosteric heat,” *J. Colloid Interf. Sci.*, vol. 278, no. 1, pp. 9–17, Oct. 2004.

[138] V. R. Choudhary, S. Mayadevi, and A. P. Singh, “Sorption isotherms of methane, ethane, ethene and carbon dioxide on NaX, NaY and Na-mordenite zeolites,” *J. Chem. Soc., Faraday Trans.*, vol. 91, no. 17, pp. 2935–2944, Jan. 1995.

[139] K. N. Son, T.-M. J. Richardson, and G. E. Cmarik, “Equilibrium Adsorption Isotherms for pure H2O on Zeolite 13X,” *Journal of Chemical & Engineering Data*, In Review.

[140] “Dynamic Dual Vapor/Gas Gravimetric Sorption Analyzer Product Brochure,” Surface Measurement Systems, Oct. 2015.

[141] D. M. Ruthven, *Principles of Adsorption and Adsorption Processes*. John Wiley & Sons, 1984.

[142] H. Ahn and C.-H. Lee, “Effects of capillary condensation on adsorption and thermal desorption dynamics of water in zeolite 13X and layered beds,” *Chemical Engineering Science*, vol. 59, no. 13, pp. 2727–2743, Jul. 2004.

[143] K. Schumann, B. Unger, A. Brandt, and F. Scheffler, “Investigation on the pore structure of binderless zeolite 13× shapes,” *Microporous and Mesoporous Materials*, vol. 154, pp. 119–123, May 2012.

[144] G. L. Aranovich and M. D. Donohue, “A New Approach to Analysis of Multilayer Adsorption,” *Journal of Colloid and Interface Science*, vol. 173, no. 2, pp. 515–520, Aug. 1995.

[145] D. R. Stull, “Vapor Pressure of Pure Substances. Organic and Inorganic Compounds,” *Ind. Eng. Chem.*, vol. 39, no. 4, pp. 517–540, Apr. 1947.

[146] R. Sips, “On the Structure of a Catalyst Surface,” *The Journal of Chemical Physics*, vol. 16, no. 5, pp. 490–495, May 1948.

[147] Y. K. Ryu, S. J. Lee, J. W. Kim, and C.-H. Leef, “Adsorption equilibrium and kinetics of H2O on zeolite 13x,” *Korean J. Chem. Eng.*, vol. 18, no. 4, pp. 525–530, Jul. 2001.

[148] J.-H. Kim *et al.*, “Adsorption Equilibria of Water Vapor on Alumina, Zeolite 13X, and a Zeolite X/Activated Carbon Composite,” *J. Chem. Eng. Data*, vol. 48, no. 1, pp. 137–141, Jan. 2003.

[149] V. K. Chuikina, A. V. Kiselev, L. V. Mineyeva, and G. G. Muttik, “Heats of adsorption of water vapour on NaX and KNaX zeolites at different temperatures,” *J. Chem. Soc., Faraday Trans. 1*, vol. 72, no. 0, pp. 1345–1354, Jan. 1976.

[150] R. Gopal, B. R. Hollebone, C. H. Langford, and R. A. Shigeishi, "The rates of solar energy storage and retrieval in a zeolite-water system," *Solar Energy*, vol. 28, no. 5, pp. 421–424, Jan. 1982.

[151] R. Zhu, B. Han, M. Lin, and Y. Yu, "Experimental investigation on an adsorption system for producing chilled water," *International Journal of Refrigeration*, vol. 15, no. 1, pp. 31–34, Jan. 1992.

[152] G. Li, P. Xiao, P. A. Webley, J. Zhang, and R. Singh, "Competition of CO2/H2O in adsorption based CO2 capture," *Energy Procedia*, vol. 1, no. 1, pp. 1123–1130, Feb. 2009.

[153] D. Ferreira, R. Magalhães, P. Taveira, and A. Mendes, "Effective Adsorption Equilibrium Isotherms and Breakthroughs of Water Vapor and Carbon Dioxide on Different Adsorbents," *Ind. Eng. Chem. Res.*, vol. 50, no. 17, pp. 10201–10210, Sep. 2011.

[154] D. Chen, X. Hu, L. Shi, Q. Cui, H. Wang, and H. Yao, "Synthesis and characterization of zeolite X from lithium slag," *Applied Clay Science*, vol. 59–60, pp. 148–151, May 2012.

[155] M. Hefti, D. Marx, L. Joss, and M. Mazzotti, "Adsorption equilibrium of binary mixtures of carbon dioxide and nitrogen on zeolites ZSM-5 and 13X," *Microporous Mesoporous Mater.*, vol. 215, pp. 215–228, Oct. 2015.

[156] B. Mette, H. Kerskes, H. Drück, and H. Müller-Steinhagen, "Experimental and numerical investigations on the water vapor adsorption isotherms and kinetics of binderless zeolite 13X," *International Journal of Heat and Mass Transfer*, vol. 71, pp. 555–561, Apr. 2014.

[157] C. Lehmann, S. Beckert, T. Nonnen, R. Gläser, O. Kolditz, and T. Nagel, "Water loading lift and heat storage density prediction of adsorption heat storage systems using Dubinin-Polanyi theory—Comparison with experimental results," *Applied Energy*, vol. 207, pp. 274–282, Dec. 2017.

[158] S. Semprini *et al.*, "Numerical modelling of water sorption isotherms of zeolite 13XBF based on sparse experimental data sets for heat storage applications," *Energy Conversion and Management*, vol. 150, pp. 392–402, Oct. 2017.

[159] K. F. Loughlin, D. Abouelnasr, and A. al Mousa, "Saturation loadings on 13X (Faujasite) zeolite above and below the critical conditions. Part IV: inorganic multi-atomic species, halocarbons and oxygenated hydrocarbons data evaluation and modeling," *Adsorption*, vol. 24, no. 1, pp. 81–94, Jan. 2018.

[160] K. N. Son, J. A. Weibel, J. C. Knox, and S. V. Garimella, "Limitations of the Axially Disperse Plug-Flow Model in Predicting Breakthrough in Confined Geometries," *Industrial & Engineering Chemistry Research*, In Preparation.

[161] S. Afandizadeh and E. A. Foumeny, "Design of packed bed reactors: guides to catalyst shape, size, and loading selection," *Appl. Therm. Eng.*, vol. 21, no. 6, pp. 669–682, Apr. 2001.

[162] "Improvements in or relating to the filling of granular materials into containers," GB606867 (A), 20-Aug-1948.

[163] J. Álvarez-Ramírez, G. Fernández-Anaya, F. J. Valdés-Parada, and J. A. Ochoa-Tapia, "Physical Consistency of Generalized Linear Driving Force Models for Adsorption in a Particle," *Ind. Eng. Chem. Res.*, vol. 44, no. 17, pp. 6776–6783, Aug. 2005.

[164] X. Hu, E. Mangano, D. Friedrich, H. Ahn, and S. Brandani, "Diffusion mechanism of CO2 in 13X zeolite beads," *Adsorption*, vol. 20, no. 1, pp. 121–135, Jan. 2014.

[165] T. J. Giesy, Y. Wang, and M. D. LeVan, "Measurement of Mass Transfer Rates in Adsorbents: New Combined-Technique Frequency Response Apparatus and Application to CO2 in 13X Zeolite," *Ind. Eng. Chem. Res.*, vol. 51, no. 35, pp. 11509–11517, Sep. 2012.

[166] D. Vortmeyer and K. Michael, "The effect of non-uniform flow distribution on concentration profiles and breakthrough curves of fixed bed adsorbers," *Chemical Engineering Science*, vol. 40, no. 11, pp. 2135–2138, Jan. 1985.

[167] M. Matthews, J. Ritter, J. M. Intyre, J. Becnel, and C. Holland, "Fundamentals Of Fixed Bed Adsorption Processes: Analysis Of Adsorption Breakthrough And Desorption Elution Curves," presented at the 2002 Annual Conference, 2002, pp. 7.583.1-7.583.9.

[168] P. Cheng, A. Chowdhury, and C. T. Hsu, "Forced Convection in Packed Tubes and Channels with Variable Porosity and Thermal Dispersion Effects," in *Convective Heat and Mass Transfer in Porous Media*, Springer, Dordrecht, 1991, pp. 625–653.

[169] F. Brandani and D. Ruthven, "Measurement of Adsorption Equilibria by the Zero Length Column (ZLC) Technique Part 2: Binary Systems," *Ind. Eng. Chem. Res.*, vol. 42, no. 7, pp. 1462–1469, Apr. 2003.

[170] J. J. Mahle and D. K. Friday, "Axial Dispersion Effects on the Breakthrough Behavior of Favorably Adsorbed Vapors," *Recents Progres en Genie Des Procedes*, vol. 5, no. 17, 1991.

[171] H. Mohamadinejad, J. C. Knox, and J. E. Smith, "Experimental and Numerical Investigation of Adsorption/Desorption in Packed Sorption Beds under Ideal and Nonideal Flows," *Separation Science and Technology*, vol. 35, no. 1, pp. 1–22, Jan. 2000.

[172] M. Giese, *Strömung in porösen Medien unter Berücksichtigung effektiver Viskositäten*. na, 1998.

[173] M. Gaeini, R. Wind, P. A. J. Donkers, H. A. Zondag, and C. C. M. Rindt, "Development of a validated 2D model for flow, moisture and heat transport in a packed bed reactor using MRI experiment and a lab-scale reactor setup," *International Journal of Heat and Mass Transfer*, vol. 113, pp. 1116–1129, Oct. 2017.

[174] O. Bey and G. Eigenberger, "Fluid flow through catalyst filled tubes," *Chemical Engineering Science*, vol. 52, no. 8, pp. 1365–1376, Apr. 1997.

[175] M. D. LeVan, “Asymptotic Fixed-Bed Behavior: Proportionate and Constant Patterns,” in *Adsorption: Science and Technology*, A. E. Rodrigues, M. D. LeVan, and D. Tondeur, Eds. Dordrecht: Springer Netherlands, 1989, pp. 149–168.

VITA

Karen N. Son received her B.S. in Mechanical Engineering from Utah State University in 2013. Later that year, she joined Cooling Technologies Research Center, an I/UCRC at Purdue University as a Graduate Research Assistant and a recipient of the NASA Space Technology Research Fellowship (NSTRF). She earned her Ph.D. in Mechanical Engineering under the advisement of Dr. Suresh V. Garimella. Her dissertation work focused on characterizing transport phenomena in sorbent beds as part of a collaboration with NASA to develop carbon dioxide removal systems for advanced space exploration. Karen spent three summers as a visiting scholar at MSFC developing predictive models of adsorption in collaboration with researchers in the Environmental Control and Life Support Systems (ECLSS) group. She has also collaborated with scientists at Sandia National Laboratories and NREL using massively parallel simulations to model pore-level physics in porous media.

PUBLICATIONS

[1] K. N. Son, C. Gomez, M. Paragon, and J. C. Knox, "Experimental validation of vacuum desorption in 1-D model of CO_2 removal," in Proceedings of the 46th International Conference on Environmental Systems, Vienna, Austria, 2016.

[2] K. N. Son, J. A. Weibel, V. Kumaresan, and S. V. Garimella, "Design of multifunctional lattice-frame materials for compact heat exchangers," International Journal of Heat and Mass Transfer, vol. 115, pp. 619–629, Dec. 2017.

[3] K. N. Son, J. A. Weibel, S. V. Garimella, and J. C. Knox, "Calibration and Sensitivity of a Fixed-Bed Adsorption Model for Atmosphere Revitalization in Space," in Proceedings of the 47th International Conference on Environmental Systems, Charleston, South Carolina, 2017, p. 173.

[4] K. N. Son, J. A. Weibel, J. C. Knox, and S. V. Garimella, "Calibration and uncertainty analysis of a fixed-bed adsorption model for CO_2 separation," Adsorption, vol. 24, no. 8, pp. 781–802, Nov. 2018.

[5] G. E. Cmarik, K. N. Son, and J. C. Knox, "Standard isotherm fit information for dry CO_2 on sorbents for 4BMS," NASA, Technical Memo NASA/TM—2017-219847, 2017.

[6] K. N. Son, G. E. Cmarik, J. C. Knox, J. A. Weibel, and S. V. Garimella, "Measurement and Prediction of the Heat of Adsorption and Equilibrium Concentration of CO_2 on Zeolite 13X," J. Chem. Eng. Data, vol. 63, no. 5, pp. 1663–1674, May 2018.

[7] K. N. Son, T.-M. J. Richardson, and G. E. Cmarik, "Equilibrium Adsorption Isotherms for pure H_2O on Zeolite 13X," Journal of Chemical & Engineering Data, In Review.

[8] K. N. Son, J. A. Weibel, J. C. Knox, and S. V. Garimella, "Limitations of the Axially Disperse Plug-Flow Model in Predicting Breakthrough in Confined Geometries," Industrial & Engineering Chemistry Research, In Preparation.

[9] K. N. Son, J. A. Weibel, J. C. Knox, and S. V. Garimella, "Effect of Radial Flow Variations on Breakthrough in Confined Geometries," Industrial & Engineering Chemistry Research, In Preparation.